



ulm university universität  
**uulm**



ZSW - Zentrum für Sonnenenergie und Wasserstoff-Forschung

Baden-Württemberg

Geschäftsbereich Elektrochemische Energietechnologien

# **Studies of high voltage $\text{LiNi}_{0.5}\text{Mn}_{1.5}\text{O}_4$ as positive electrode material in lithium ion cells**

Dissertation zur Erlangung des Doktorgrades Dr. rer. nat.  
der Fakultät für Naturwissenschaften der Universität Ulm

vorgelegt von

**Giulio Gabrielli**

aus Sassocorvaro – Italien

- 2016 -

Amtierender Dekan: Prof. Dr. Peter Dürre

Erster Gutachter: Prof. Dr. Werner Tillmetz

Zweiter Gutachter: Prof. Dr. Mika Lindén

Dritter Gutachter: Prof. Dr. Andrea Balducci

Tag der Promotion: 22.12.2016

# Abstract

Since their first commercialization in 1991, Li-ion batteries (LIBs) present many advantages with respect to other commercial battery technologies. In particular, their higher specific energy and specific power make LIBs the best candidate for electric mobile transport application. Nowadays, electric vehicles are a concrete possibility for the future of mobile transport and new high-energy LIBs are the key to realise it.

Developing the next generation of LIBs requires innovative and cheaper cathode materials with higher operating potentials. Among these “high-voltage materials”,  $\text{LiNi}_{0.5}\text{Mn}_{1.5}\text{O}_4$  (LMNO) is one of the most promising candidates because of its high operating potential (4.7 V vs.  $\text{Li/Li}^+$ ), good specific capacity and low production costs. Unfortunately, standard organic electrolytes are not stable above 4.5 V vs.  $\text{Li/Li}^+$  and thus, higher operating potentials translate into electrolyte degradation and fast aging of the electrochemical system.

The cathode material investigated in this work is an innovative LMNO with tailored particle architecture (LMNO-0). This tailored architecture combines the low surface area of micrometric particles with the fast kinetics of nanometric primary crystallites in order to guarantee a good compromise between stability and electrochemical performance at high potential. Furthermore, LMNO-0 powders present tap-density, surface area and processability, in line with commercial cathode materials. Additional modifications of crystallite size, oxygen stoichiometry and particle dimension significantly influence the electrochemical behaviour of LMNO-0 and allow identifying the optimal material for LIBs application.

The optimisation of the particles morphology plays a fundamental role also in reducing the electrolyte degradation rates of LMNO-0 electrodes operating at high potential. In particular, the low surface area accessible for secondary reactions and the dense network of crystallites are key parameters in reducing the surface reactivity and improving the Li-ion diffusion. This remarkable

electrochemical behaviour of LMNO-0 electrodes is even more evident when using suitable charging protocols, developed in function of the desired cycling rate.

The particle architecture is a crucial feature for reducing the electrolyte degradation rate at high potential; however, it does not influence the nature of the secondary reactions occurring at the particles surface. A valid strategy for improving the active material/electrolyte interface of the morphologically tailored LMNO consists in coating the particles with a thin layer of lithium niobate ( $\text{LiNbO}_3$ ). This stable and homogeneous coating does not compromise the electrochemical performance of the pristine material but acts as a stable and ion-conductive passivation layer.

Both the coated and the uncoated LMNO present stable high voltage behaviour, remarkable coulombic efficiency and good charge/discharge capacity also when used in full Li-ion cells versus graphite anodes. However, cells using the coated LMNO present twofold cycling stability and significantly reduced cell aging (80% capacity retention after 660 cycles) with respect to those assembled with the uncoated one (80% capacity retention after 335 cycles). These results confirm the beneficial effects of the particle morphology also in full cells and additionally, point out the impressive cycling stability achievable with the  $\text{LiNbO}_3$  surface coating. Unfortunately, the same results are not reproducible increasing the testing temperature at 45 °C. In this case, accelerated aging kinetics lead to lower cycling stability and rapid capacity fade of all the tested full cells.

Realising high-voltage Li-ion cells suitable for practical application is still an open challenge both for the scientific community and for the manufacturers. This study presents very encouraging results, which touch different fundamental aspects of these complicated systems and delineate possible paths for further investigation works.



# List of publications

**Part of this dissertation have been published in the following journal articles:**

*Tailoring high-voltage and high-performance  $\text{LiNi}_{0.5}\text{Mn}_{1.5}\text{O}_4$  cathode material for high energy Lithium-ion batteries*

P. Axmann, G. Gabrielli, M. Wohlfahrt-Mehrens

Journal of Power Sources, 301, (2016) 151-159.

DOI: 10.1016/j.jpowsour.2015.10.010

*Study of  $\text{LiNi}_{0.5}\text{Mn}_{1.5}\text{O}_4$  morphological features for reduced electrolyte decomposition at high potential*

G. Gabrielli, P. Axmann, M. Wohlfahrt-Mehrens

Journal of the Electrochemical Society, 163, (2016), A470-A476.

DOI: 10.1149/2.0541603jes

*Combining optimized  $\text{LiNi}_{0.5}\text{Mn}_{1.5}\text{O}_4$  particle morphology and  $\text{LiNbO}_3$  coating for long cycling-life graphite/ $\text{LiNi}_{0.5}\text{Mn}_{1.5}\text{O}_4$  full cells*

G. Gabrielli, P. Axmann, T. Diemant, R. J. Behm, M. Wohlfahrt-Mehrens

ChemSusChem, 10.1002/cssc.201600278, (2016)

DOI: 10.1002/cssc.201600278

## **Presentation at conferences:**

### ***Oral Presentations:***

*Developing High Cycling Stability Graphite/LiNi<sub>0.5</sub>Mn<sub>1.5</sub>O<sub>4</sub> Li-Ion Cells*

Giulio Gabrielli, Peter Axmann, Margret Wohlfahrt-Mehrens

229th ECS Meeting 2016, May 29 - June 2, San Diego, California (United States)

*High performance high voltage spinel materials as cathode for Li-ion batteries and its application in full cells.*

G. Gabrielli, P. Axmann, M. Wilka, M. Wohlfahrt-Mehrens

GDCh Wissenschaftsforum Chemie 2013, 1-4 September 2013, Darmstadt (Germany)

### ***Posters:***

*Strategies to improve long term stability of graphite/LMNO full cells*

G. Gabrielli, P. Axmann, Thomas Diemant, Rolf Jürgen Behm, M. Wohlfahrt-Mehrens

Battery Conference, 25-27 April 2016, Münster (Germany)

*Effect of the surface area and morphology of high voltage spinel materials on the stability of organic electrolyte working at high potential.*

G. Gabrielli, P. Axmann, M. Wilka, M. Wohlfahrt-Mehrens

ILED, May 28-30 May 2014, Rome (Italy)

# Table of Contents

<b>LIST OF FIGURES .....</b>	<b>VII</b>
<b>LIST OF TABLES .....</b>	<b>XIV</b>
<b>1. INTRODUCTION.....</b>	<b>1</b>
1.1 Li-ion batteries and sustainable energy .....	1
1.2 Batteries .....	4
1.3 Li-ion Batteries: Origins, present and next future. ....	8
1.4 High-energy cathode materials .....	12
1.5 $\text{LiNi}_{0.5}\text{Mn}_{1.5}\text{O}_4$ as high voltage cathode for Li-ion batteries .....	14
<b>2. AIMS OF THE THESIS.....</b>	<b>19</b>
<b>3. EXPERIMENTAL .....</b>	<b>20</b>
3.1 Materials .....	20
3.1.1 $\text{LiNi}_{0.5}\text{Mn}_{1.5}\text{O}_4$ .....	20
3.1.2 $\text{LiNi}_{0.5}\text{Mn}_{1.5}\text{O}_{4-\delta}$ .....	21
3.1.3 $\text{LiNbO}_3$ -treated $\text{LiNi}_{0.5}\text{Mn}_{1.5}\text{O}_4$ .....	22
3.1.4 Graphite .....	23
3.2 Analytical Methods.....	25
3.2.1 Inductively Coupled Plasma - Optical Emission Spectroscopy (ICP-OES) .....	25
3.2.2 Laser diffraction analysis.....	25
3.2.3 Nitrogen adsorption porosimetry .....	26
3.2.4 Scanning Electron Microscopy (SEM) and Energy Dispersive X-ray Spectroscopy (EDX) .....	27
3.2.5 Tap-density .....	28
3.2.6 X-ray diffraction on powders (XRD).....	29
3.3 Electrodes Preparation .....	31
3.4 Electrochemical Characterisation .....	32
3.4.1 Cells configurations .....	32
3.4.2 Electrochemical Techniques .....	34
<b>4. RESULTS AND DISCUSSION – PART I.....</b>	<b>41</b>
4.1 Characterisation of the Pristine $\text{LiNi}_{0.5}\text{Mn}_{1.5}\text{O}_4$ .....	41
4.1.1 Morphology and composition of LMNO-0 .....	41
4.1.2 Electrochemical Performance of LMNO-0.....	46

4.2 Modification of the Pristine Material .....	49
4.2.1 Crystallite Size Effects .....	49
4.2.2 Changes in the Oxygen Stoichiometry of LMNO.....	53
4.2.3 Role of the particle dimension in LMNO-0 electrodes .....	60
<b>5. RESULTS AND DISCUSSION – PART II.....</b>	<b>63</b>
5.1 STUDY OF THE ELECTROLYTE STABILITY ON LMNO-0 ELECTRODES.....	63
5.2 CHARGE OPTIMIZATION OF LMNO-0 ELECTRODES. ....	75
<b>6. RESULTS AND DISCUSSION – PART III.....</b>	<b>80</b>
6.1 LiNbO <sub>3</sub> SURFACE TREATMENT OF LMNO .....	80
6.2 REALIZATION OF GRAPHITE/LMNO FULL CELLS .....	87
<b>7. SUMMARY .....</b>	<b>98</b>
<b>BIBLIOGRAPHY .....</b>	<b>105</b>

# List of Figures

<b>Figure 1:</b> Average IEA crude oil import price by scenario. © OECD/IEA 2014 World Energy Outlook, IEA Publishing. <sup>1</sup> Licence: <a href="http://www.iea.org/t&amp;c">www.iea.org/t&amp;c</a> . ....	1
<b>Figure 2:</b> Total primary energy demand and gross domestic product (GDP) in selected countries, 1971-2012. © OECD/IEA 2014 World Energy Outlook, IEA Publishing. <sup>1</sup> Licence: <a href="http://www.iea.org/t&amp;c">www.iea.org/t&amp;c</a> . ....	2
<b>Figure 3:</b> Scheme of a redox reaction: (a) initial state, (b), (c) proceeding of the redox reaction (d) final state. ....	5
<b>Figure 4:</b> Representation of a Li-ion battery based on graphite as anode material and LiCoO <sub>2</sub> as cathode material. ....	9
<b>Figure 5:</b> Voltage versus capacity for different anode and cathode materials for Li-ion batteries. ....	10
<b>Figure 6:</b> Ragone plot comparing different battery technologies. Reproduced (“Adapted” or “in part”) from Chem. Soc. Rev., 2015, 44, 5926 with permission of The Royal Society of Chemistry. <sup>25</sup> License Number: 3871920800244. <a href="http://dx.doi.org/10.1039/c4cs00442f">http://dx.doi.org/10.1039/c4cs00442f</a> .....	11
<b>Figure 7:</b> Voltage profiles of the Li <sub>1.2</sub> Ni <sub>0.2</sub> Mn <sub>0.6</sub> O <sub>2</sub> electrodes during cycling. Reproduced (“Adapted” or “in part”) from J. Mater. Chem. A, 2015, 3, 9915 with permission of The Royal Society of Chemistry. <sup>39</sup> License Number: 3871970359256. <a href="http://dx.doi.org/10.1039/c5ta01214g">http://dx.doi.org/10.1039/c5ta01214g</a> .....	13
<b>Figure 8:</b> Representation of (a) fully-stoichiometric spinel structure and (b) oxygen-deficient spinel structure. Reproduced with the permission from Adv. Mater. 2012, 24, 2109-2116. Copyright 2012 WILEY-VCH Verlag GmbH & Co. KGaA. License	

Number: 3872450012137. Voltage vs. capacity curves for (c) $\text{LiNi}_{0.5}\text{Mn}_{1.5}\text{O}_4$ , (d) $\text{LiNi}_{0.5}\text{Mn}_{1.5}\text{O}_{4-\delta}$ . Adapted with permission from Chem. Mater. 2004, 16, 906-914. Copyright 2004 American Chemical Society. <sup>53</sup> .....	16
<b>Figure 9:</b> Representation of the spinel structure $\text{LiNi}_{0.5}\text{Mn}_{1.5}\text{O}_4$ . Reproduced (“Adapted” or “in part”) from J. Mater. Chem., 2007, 17, 3668–3677 with permission of The Royal Society of Chemistry. Licence Number: 3874820112217. <a href="http://dx.doi.org/10.1039/b707040n">http://dx.doi.org/10.1039/b707040n</a> .....	20
<b>Figure 10:</b> (a) Stacking of graphene layers in graphite and (b) Current vs. potential plot for a graphite anode and Li intercalation stages. Adapted with permission from J. Phys. Chem. B 1997, 101, 4630-4640. Copyright 1997 American Chemical Society. ....	23
<b>Figure 11:</b> Types of physisorption isotherms.....	26
<b>Figure 12:</b> Radiation emission principle in the Energy Dispersive Spectroscopy. ....	28
<b>Figure 13:</b> Lattice leading to a destructive interference (left) or to a constructive interference (right) of the diffracted X-rays. ....	29
<b>Figure 14:</b> Schematic representation of a T-Cell. ....	32
<b>Figure 15:</b> (left) representation of the coin cells components, (right) coin cell ready for using. ....	33
<b>Figure 16:</b> ECC-Ref cell from EL-CELL.....	34
<b>Figure 17:</b> (a) Current variation in function of the time and (b) voltage variation in terms of time during a charge/discharge cycling test. ....	35
<b>Figure 18:</b> (a) Linear potential scan from an initial value ( $E_i$ ) to a final value ( $E_f$ ) and (b) measured current during the potential scan. ....	37
<b>Figure 19:</b> Nyquist’s plot of impedance.....	39
<b>Figure 20:</b> Nyquist’s plots for (a) a resistor, (b) a capacitor, (c) a Warburg semi-infinite diffusion element and (d) a Randles circuit for electrode-electrolyte interfaces. ....	40

<b>Figure 21:</b> Representation of the desired LMNO particle architecture. ....	41
<b>Figure 22:</b> SEM images of the synthesized LMNO-0 at different magnifications. Reprinted from J. Power Sources, 301, (2016), 151-159. Copyright 2015, with permission from Elsevier. <sup>102</sup> Licence number 3875240261510.....	42
<b>Figure 23:</b> Particle size distribution of LMNO-0. Reproduced in part with permission from J. Electrochem. Soc., 163, A470 (2016). Copyright 2016, The Electrochemical Society. ....	43
<b>Figure 24:</b> XRD pattern and fitting for LMNO-0 powders. ....	44
<b>Figure 25:</b> (a) Charge/Discharge cycles, (b) Potential vs. Specific capacity and (c), (d) corresponding differential curves for LMNO-0 electrodes. Adapted and reprinted from J. Power Sources, 301, (2016), 151-159. Copyright 2015, with permission from Elsevier. <sup>102</sup> Licence number 3875240261510.....	46
<b>Figure 26:</b> SEM images of the sample LMNO-T1. Reprinted in part from J. Power Sources, 301, (2016), 151-159. Copyright 2015, with permission from Elsevier. <sup>102</sup> Licence number 3875240261510.....	49
<b>Figure 27:</b> XRD pattern and fit for the sample LMNO-T1. ....	50
<b>Figure 28:</b> Potential vs. Specific capacity profiles obtained for (a) LMNO-0 and (b) LMNO-T1. Reprinted in part from J. Power Sources, 301, (2016), 151-159. Copyright 2015, with permission from Elsevier. <sup>102</sup> Licence number 3875240261510.....	51
<b>Figure 29:</b> (a) Trend of the hysteresis and (b) of the discharge specific capacity in function of the applied C-rate for LMNO-0 and LMNO-T1, LMNO-T2 and LMNO-T3 electrodes. Reprinted in part from J. Power Sources, 301, (2016), 151-159. Copyright 2015, with permission from Elsevier. <sup>102</sup> Licence number 3875240261510. ....	52

<b>Figure 30:</b> SEM images of (a) LMNO-T2 and (b) LMNO-T3. Reprinted in part from J. Power Sources, 301, (2016), 151-159. Copyright 2015, with permission from Elsevier.	
<sup>102</sup> Licence number 3875240261510. ....	53
<b>Figure 31:</b> XRD patterns and fits for LMNO-0, LMNO-T1, LMNO-T2 and LMNO-T3. Reprinted from J. Power Sources, 301, (2016), 151-159. Copyright 2015, with permission from Elsevier. <sup>102</sup> Licence number 3875240261510. ....	54
<b>Figure 32:</b> Potential vs. specific capacity profiles for (a) LMNO-0, (b) LMNO-T1, (c) LMNO-T2 and (d) LMNO-T3 electrodes. Reprinted in part from J. Power Sources, 301, (2016), 151-159. Copyright 2015, with permission from Elsevier. <sup>102</sup> Licence number 3875240261510. ....	56
<b>Figure 33:</b> (a) $U_{\text{plat}}$ and $U_{\text{max}}$ at 1C and 2C for LMNO-0 electrodes. (b) Increase of $U_{\text{plat}}$ and $U_{\text{max}}$ with the C-rate and extrapolation at 3C for LMNO-0 electrodes. ....	57
<b>Figure 34:</b> Impedance spectra for LMNO-0 and LMNO-T3 electrodes in (a), (b) lithiated status and (c), (b) delithiated status. Reprinted from J. Power Sources, 301, (2016), 151-159. Copyright 2015, with permission from Elsevier. <sup>102</sup> Licence number 3875240261510. ....	58
<b>Figure 35:</b> SEM images for (a) LMNO-L, (b) LMNO-M, (c) LMNO-S and (d) LMNO-XS. Reprinted from J. Power Sources, 301, (2016), 151-159. Copyright 2015, with permission from Elsevier. <sup>102</sup> Licence number 3875240261510. ....	60
<b>Figure 36:</b> Potential vs. Specific capacity profiles for (a) LMNO-XS, (b) LMNO-S, (c) LMNO-M (d) LMNO-L and (f) reversible specific capacity for the same electrodes. Reprinted in part from J. Power Sources, 301, (2016), 151-159. Copyright 2015, with permission from Elsevier. <sup>102</sup> Licence number 3875240261510. ....	61
<b>Figure 37:</b> SEM images for (a), (b) LMNO-R and (c), (d) LMNO-0 samples. ....	64



<b>Figure 38:</b> Particle size distribution for LMNO-R powders. Reproduced in part with permission from J. Electrochem. Soc., 163, A470 (2016). Copyright 2016, The Electrochemical Society. <sup>103</sup>	65
<b>Figure 39:</b> XRD pattern and fit for the sample LMNO-R. Reproduced in part with permission from J. Electrochem. Soc., 163, A470 (2016). Copyright 2016, The Electrochemical Society. <sup>103</sup>	66
<b>Figure 40:</b> Linear potential sweep for LMNO-0 and LMNO-R electrodes. Reproduced with permission from J. Electrochem. Soc., 163, A470 (2016). Copyright 2016, The Electrochemical Society. <sup>103</sup>	67
<b>Figure 41:</b> Potential profiles and current trends for (a) LMNO-0 and (b) LMNO-R electrodes obtained by holding the potential at 4.72, 4.76, 4.90 and 5.00 V vs. Li/Li <sup>+</sup> . Reproduced in part with permission from J. Electrochem. Soc., 163, A470 (2016). Copyright 2016, The Electrochemical Society. <sup>103</sup>	69
<b>Figure 42:</b> Trend of the coulombic efficiency for LMNO-0 and LMNO-R electrodes cycled two times between 3.5 and 4.9 V vs. Li/Li <sup>+</sup> and then 10 times holding the potential at 4.72, 4.76, 4.90 and 5.00 V vs. Li/Li <sup>+</sup> during charging.	71
<b>Figure 43:</b> (a) Equivalent circuit, impedance spectra and relative fittings obtained at the (b) 6 <sup>th</sup> , (c) 10 <sup>th</sup> and (d) 14 <sup>th</sup> cycle of LMNO-0 and LMNO-R electrodes. Adapted and reproduced with permission from J. Electrochem. Soc., 163, A470 (2016). Copyright 2016, The Electrochemical Society. <sup>103</sup>	72
<b>Figure 44:</b> Trend of the R <sub>F</sub> during cycling for LMNO-0 and LMNO-R electrodes.	73
<b>Figure 45:</b> (a) Potential and specific current profiles, (b) discharge specific capacity and coulombic efficiency for LMNO-0 electrodes charged with a potentiostatic step at different cut-offs. Reproduced with permission from J. Electrochem. Soc., 163, A470 (2016). Copyright 2016, The Electrochemical Society. <sup>103</sup>	76

<b>Figure 46:</b> (a) Discharge capacity and (b) coulombic efficiency of LMNO-0 cycled according different charging procedures. Adapted and reproduced with permission from J. Electrochem. Soc., 163, A470 (2016). Copyright 2016, The Electrochemical Society. <sup>103</sup>	78
<b>Figure 47:</b> SEM images of LMNO-T at different magnifications.	81
<b>Figure 48:</b> (a); (b) TEM images, (c); (e); (g); (i); EDX analyses and (d); (f); (h); (j) EELS analyses of LMNO-T particles. The green, blue, red and light blue colours correspond to the detected Mn, Ni, O and Nb, respectively. Adapted and reproduced with the permission from ChemSusChem. 2016, DOI: 10.1002/cssc.201600278. Copyright 2016 WILEY-VCH Verlag GmbH & Co. KGaA. <sup>88</sup> License Number: 3883560968998	82
<b>Figure 49:</b> XPS spectra for LMNO-T and LMNO (a) in the Nb(3d) and (b) in the Mn(3p)/Li(1s) regions. Adapted and reproduced with the permission from ChemSusChem. 2016, DOI: 10.1002/cssc.201600278. Copyright 2016 WILEY-VCH Verlag GmbH & Co. KGaA. <sup>88</sup> License Number: 3883560968998	83
<b>Figure 50:</b> XRD patterns of LMNO-T.	84
<b>Figure 51:</b> Discharge specific capacity and coulombic efficiency of LMNO-T electrodes. Reproduced in part with the permission from ChemSusChem. 2016, DOI: 10.1002/cssc.201600278. Copyright 2016 WILEY-VCH Verlag GmbH & Co. KGaA. <sup>88</sup> License Number: 3883560968998	85
<b>Figure 52:</b> Voltage profiles and specific capacity of Graphite anodes cycled in half-cells at C/4. Reproduced with the permission from ChemSusChem. 2016, DOI: 10.1002/cssc.201600278. Copyright 2016 WILEY-VCH Verlag GmbH & Co. KGaA. <sup>88</sup> License Number: 3883560968998	88

<b>Figure 53:</b> Electrodes potential profiles and cell voltage of a Graphite/LMNO full cell.	89
<b>Figure 54:</b> (a) Potential profiles and (b) cycling stability of a Graphite/LMNO full cell.	
Reproduced in part with the permission from ChemSusChem. 2016, DOI:	
10.1002/cssc.201600278. Copyright 2016 WILEY-VCH Verlag GmbH & Co. KGaA.	<sup>88</sup>
License Number: 3883560968998	90
<b>Figure 55:</b> Impedance values and fittings for Graphite/LMNO cells in the discharged state.	
Reproduced in part with the permission from ChemSusChem. 2016, DOI:	
10.1002/cssc.201600278. Copyright 2016 WILEY-VCH Verlag GmbH & Co. KGaA.	<sup>88</sup>
License Number: 3883560968998	92
<b>Figure 56:</b> (a) Potential profiles and (b) cycling stability of a Graphite/LMNO-T full cell.	
Reproduced in part with the permission from ChemSusChem. 2016, DOI:	
10.1002/cssc.201600278. Copyright 2016 WILEY-VCH Verlag GmbH & Co. KGaA.	<sup>88</sup>
License Number: 3883560968998	94
<b>Figure 57:</b> (a) impedance measurements and fittings for Graphite/LMNO-T cells; (b) comparison between the $R_{SC}$ of Graphite/LMNO and Graphite/LMNO-T cells.	
Adapted and reproduced with the permission from ChemSusChem. 2016, DOI:	
10.1002/cssc.201600278. Copyright 2016 WILEY-VCH Verlag GmbH & Co. KGaA.	<sup>88</sup>
License Number: 3883560968998	95
<b>Figure 58:</b> Potential profiles and cycling stability for (a), (b) Graphite/LMNO and (c), (d) Graphite/LMNO-T cells tested at 45 °C.	
Adapted and reproduced with the permission from ChemSusChem. 2016, DOI: 10.1002/cssc.201600278. Copyright 2016	
WILEY-VCH Verlag GmbH & Co. KGaA.	<sup>88</sup>
License Number: 3883560968998	
(Adapted)	97

# List of Tables

**Table 1:** XRD fits results for LMNO-0, LMNO-T2 and LMNO-T3. ....55

**Table 2:** Equilibrium current values measured at the end of the potentiostatic steps. ...70

# 1. INTRODUCTION

## 1.1 Li-ion batteries and sustainable energy

The problems related to a fossil fuel based society are nowadays clear and commonly accepted. The fossil fuels are a non-renewable energy vector and following the current policies, they will become year after year more expensive and inaccessible (**Figure 1**). On the other side, the evolution of the present society requires increasing amounts of energy, especially in the developing countries (**Figure 2**).<sup>1</sup>

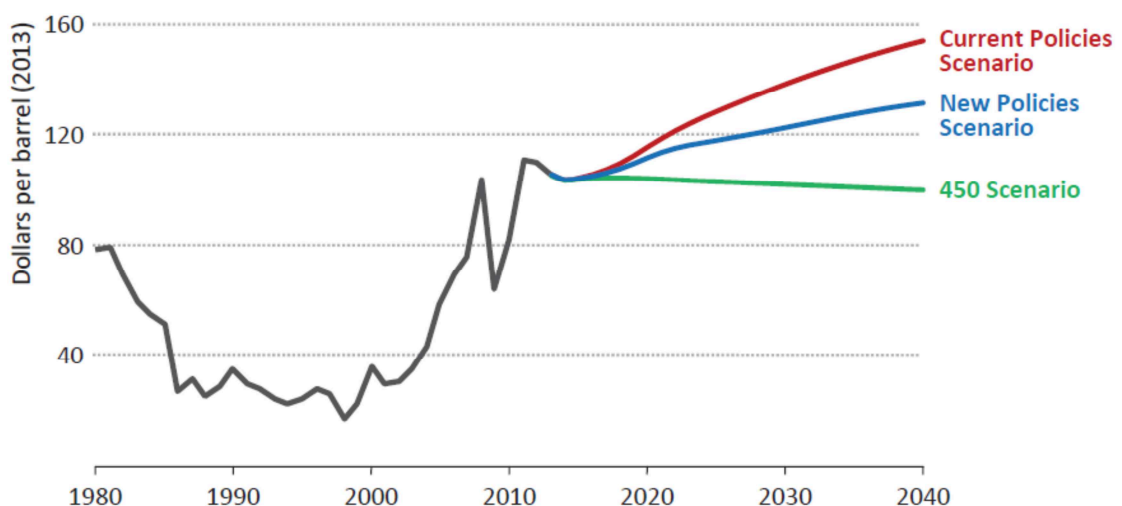


**Figure 1:** Average IEA crude oil import price by scenario. © OECD/IEA 2014 World Energy Outlook, IEA Publishing.<sup>1</sup> Licence: [www.iea.org/t&c](http://www.iea.org/t&c).

The extensive use of fossil fuel (e.g. oil, coal and natural gases) constantly increases the CO<sub>2</sub> and pollution levels in the atmosphere, with consequent global warming and changes in the world climate. These changes will become dramatic without a concrete solution to the current polluting emissions.

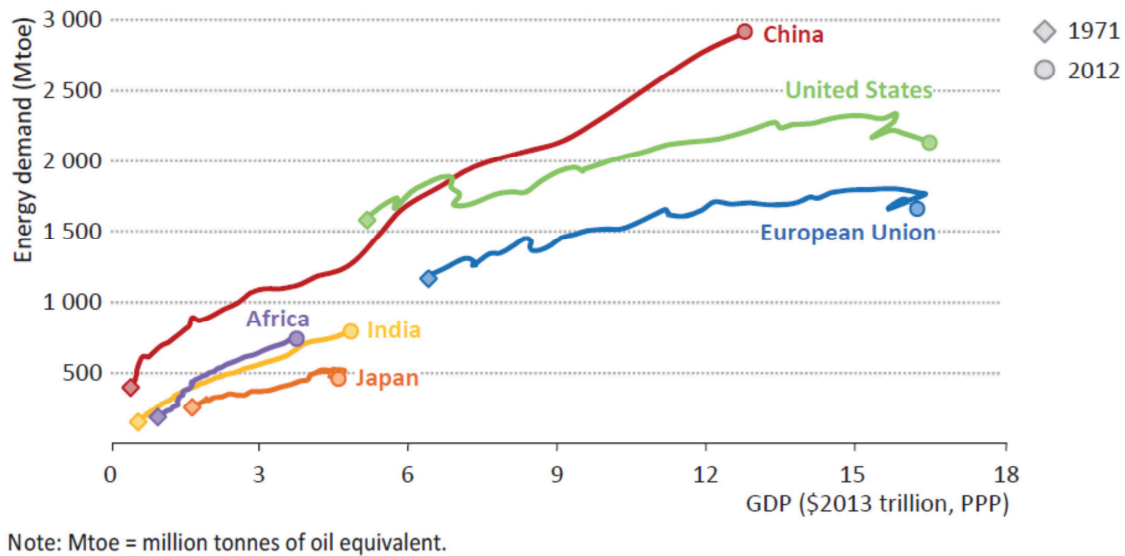


**Figure 2:** Total primary energy demand and gross domestic product (GDP) in selected countries, 1971-2012. © OECD/IEA 2014 World Energy Outlook, IEA Publishing.<sup>1</sup> Licence: [www.iea.org/t&c](http://www.iea.org/t&c).

In order to avoid this scenario, new eco-friendly, renewable and harmless energy suppliers should gradually replace the fossil fuels. Among these new energy suppliers, the sun and the wind are the most accessible and diffuse alternatives. Solar panels and wind turbines are already a common technology, principally employed in supporting the main energy distribution systems. Unfortunately, the fossil fuels still present key features, which make their replacement on a global scale a very challenging task. In particular, the ease of transport, the high energy density and the capacity to supply energy in-continuous make the fossil fuels more practical and cheap in comparison to the localized and intermittent energy provide by sun or wind. Adopting efficient and high-performance energy storage systems allows stocking the produced energy and then relocating or using it when necessary. This way, it is possible to overcome the problems related to the continuity and the distribution of the collected energy.

Batteries are scalable storage devices suitable for both fix and mobile applications. Moreover, the facile scalability makes this energy storage system very attractive also for the electric-based mobile transport. Different battery

technologies are already available on the market but among them, Li-ion batteries are the best candidates as high-energy systems. In comparison with other battery technologies (e.g. Lead-acid, Nickel-Cadmium or Nickel-Metal hydrate batteries), Li-ion batteries present many superior characteristics. Among them, high specific energy and energy density (normally over 150 Wh kg<sup>-1</sup> or 400 Wh l<sup>-1</sup>), wide operating temperature range (from -10 °C to 60 °C), reduced charging time, low self-discharge rate (typically 2 – 3 % per month), absence of memory effect and long cycling life.<sup>2,3</sup>

The road transport sector already adopted Li-ion batteries for different types of electric vehicles, such as Hybrid Electric Vehicles (HEVs), Plug-in Hybrid Electric Vehicles (PHEVs) and fully Electric Vehicles (EVs). However, the current Li-ion batteries still require improvements, especially for a large-scale EVs diffusion.<sup>4</sup> The market of the electric vehicles requires safer and cheaper batteries suitable for extended driving ranges and fast recharge. All these issues depend mainly on the materials adopted in the batteries and thus, on the complex chemistry and electrochemistry behind these apparently simple devices.

## 1.2 Batteries

A battery is a device consisting in one or more electrochemical cells connected in series or parallel and able to convert chemical energy in electrical energy. The conversion from chemical energy to electrical energy occurs in the electrochemical cell, where two species react via a redox reaction and generate an electrons flow through an external circuit.

The electrochemical cells consist in three different main elements:

- Anode: The anode is the negative electrode, which releases electrons during the redox reaction (oxidation).
- Cathode: The cathode is the positive electrode, which accepts the electrons coming from the anode during the redox reaction (reduction).
- Electrolyte: The electrolyte is an ion-conductive media (generally liquid), which allows the charge transfer between the anode and the cathode in form of ions flow. The electrolyte is also electronically insulating in order to prevent short cuts between the electrodes.

The reaction occurring in an electrochemical cell appears as a scheme in **Figure 3**.



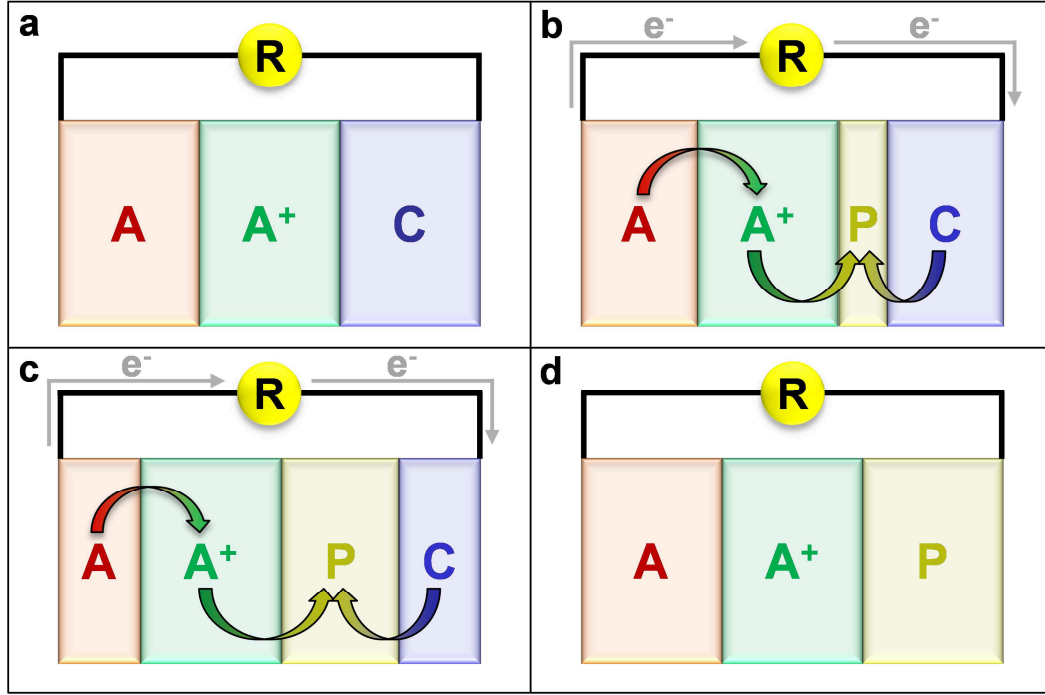


**Figure 3:** Scheme of a redox reaction: (a) initial state, (b), (c) proceeding of the redox reaction (d) final state.

In the reported scheme,  $A$  represents the anode material and  $C$  the cathode material. The electrolyte is assumed to contain  $A^+$  ions free to move between the electrodes. During the reaction,  $A$  gradually oxidises releasing  $A^+$  in the electrolyte. At the same time, an equivalent amount of  $e^-$  flows from the anode to the cathode through the external circuit. The  $A^+$  ions in the electrolyte migrate to the surface of the cathode, where together with  $C$  and the electrons coming from the anode, react and form the new species  $P$ . This process continues until at least one of the two materials  $A$  or  $C$  reacts completely. The process described consists in two half-reactions: one occurring at the anode and defined as oxidation half-reaction (1.1). The other one occurring at the cathode and defined as reduction half-reaction (1.2):



The overall reaction between  $A$  and  $C$  is the combination of the two half-reactions:



If the reaction between the two materials is not efficiently reversible, the electrochemical cell allows only one single conversion of chemical energy in electrical energy (discharge). Systems based on these cells are primary batteries such as alkaline batteries or Zinc-Carbon batteries.

In the case of an efficient reversible reaction, the electrochemical cell allows both the conversion of chemical energy into electrical energy (discharge) and the storage of electrical energy in form of chemical energy (charge). Systems based on these cells are secondary or rechargeable batteries, such as Lead-acid, Nickel-Cadmium or Nickel-Metal hydrate batteries.

A fundamental parameter in an electrochemical cell is the voltage. The voltage of an electrochemical cell at the equilibrium (no current flowing) is described by the Nernst equation (1.4), which, assuming a general redox reaction  $aA + bB \rightarrow cC + dD$ , is: <sup>5, 6</sup>

$$E = E^0 - \left( \frac{RT}{zF} \right) \ln \left( \frac{\{C\}^c \{D\}^d}{\{A\}^a \{B\}^b} \right) \quad (1.4)$$

Where  $E^0$  is the cell potential at standard-state conditions,  $R$  is the gas constant,  $T$  is the absolute temperature,  $z$  is the number of mole of electrodes involved in the reaction,  $F$  is the Faraday's constant ( $F = 96485 \text{ C mol}^{-1}$ ),  $\{A\}$ ,  $\{B\}$ ,  $\{C\}$ ,  $\{D\}$  and  $a$ ,  $b$ ,  $c$ ,  $d$  are the activities and the number of moles of the involved, respectively. The voltage observed with no current flow is the open circuit voltage (OCV). When an appreciable current starts to flow, a voltage drop occurs. This voltage drop is related to different resistances: (a) the ohmic drop (IR drop), due to the internal resistances of the cell, (b) The concentration overpotential, due to the formation of concentration gradients inside the cell and (c) the surface

overpotential, due to the charge-transfer reactions on the surface of the electrodes.<sup>6</sup>

A second fundamental property of an electrochemical cell is the theoretical capacity ( $Q$  / Ah), which is defined as the total amount of charge involved in the reaction according to the equation:<sup>6</sup>

$$Q = \frac{zFm}{M} \quad (1.5)$$

Where  $z$  is the number of electrons transferred from each ion,  $F$  is the Faraday's constant,  $m$  is the mass of the reacting substance and  $M$  is the molar mass of the reacting substance. In the battery field, the theoretical capacity is often normalised to the active material mass the studied electrode, obtaining this way the theoretical gravimetric specific capacity ( $Q_{spec}$  / Ah g<sup>-1</sup>):

$$Q_{spec} = \frac{zF}{M} \quad (1.6)$$

Both the capacity and the voltage define the energy of an electrochemical cell according to the equation:<sup>6</sup>

$$Energy (Wh) = Capacity (Ah) \times Voltage (V) \quad (1.7)$$

Often, the energy of a battery is normalised according to the weight or to the volume of the system defining this way the specific energy (Wh kg<sup>-1</sup>) and the energy density (Wh L<sup>-1</sup>).

The energy of a battery clearly depends on the chemistry of the cell. Improvements of the energy density require studying new active materials with higher capacity or higher operating potentials.

### 1.3 Li-ion Batteries: Origins, present and next future.

The Li-ion technology is based on the electrochemical insertion/deinsertion of a small guest ( $\text{Li}^+$ ) into a stable host crystalline structure.<sup>5</sup> The choice of Li as guest depends on its light atomic weight ( $6.941 \text{ g mol}^{-1}$ ) and its low reduction potential ( $E^0 = -3.05 \text{ V vs. SHE}$ ), which guarantee considerable specific capacity and thus high energy at the cells level.

One of the first Li-ion batteries consisted in metallic Li coupled with  $\text{LiTiS}_2$  as intercalation cathode material.<sup>7,8,9</sup> Because of the metallic Li, these batteries had many safety issues and resulted inappropriate for commercial applications. In the following years, the Li metal anode was replaced with an intercalation anode introducing a new concept of Li-ion battery called the Rocking Chair Battery.<sup>10,11,12</sup> This new concept of Li-ion battery led to the first commercialization of a Li-ion battery in 1991 by Sony, which used graphite as anode material and  $\text{LiCoO}_2$  as cathode material. The introduction of the first Li-ion battery revolutionised the electronic device sector, promoting a large diffusion of portable devices such as laptops and mobile phones. In the following years, the Li-ion technology developed continuously both on a cell level and on a materials level, increasing the specific energy of a single battery from  $98 \text{ Wh kg}^{-1}$  in 1991 to more than  $200 \text{ Wh kg}^{-1}$  in 2015.<sup>13,14</sup>

**Figure 4** shows a schematic representation of an operating Li-ion battery based on graphite as anode intercalation material and  $\text{LiCoO}_2$  as intercalation cathode material. The electrodes of a Li-ion battery are metallic current collectors (generally Cu foil at the anode and Al foil at the cathode) coated with a composite material containing high percentage of active material. A separator (generally a porous polymeric foil) soaked with the electrolyte (a mixture of organic solvents and Li-salt) avoids short cuts between the electrodes and guarantees the Li-ions diffusion between anode and cathode. The charge of a Li-ion battery consists in the extraction of  $\text{Li}^+$  from the cathode material (delithiation) and the simultaneous insertion of  $\text{Li}^+$  into the anode (lithiation).

During delithiation, the cathode material undergoes an oxidation, releasing in the external circuit a quantity of electrons equivalent to the amount of extracted  $\text{Li}^+$ . At the same time, the anode undergoes a reduction, uptaking electrons from the external circuit and inserting an equivalent amount of  $\text{Li}^+$  in its structure. The discharge follows the same principle but the exchange of  $\text{Li}^+$  and electrons occurs in the opposite direction.

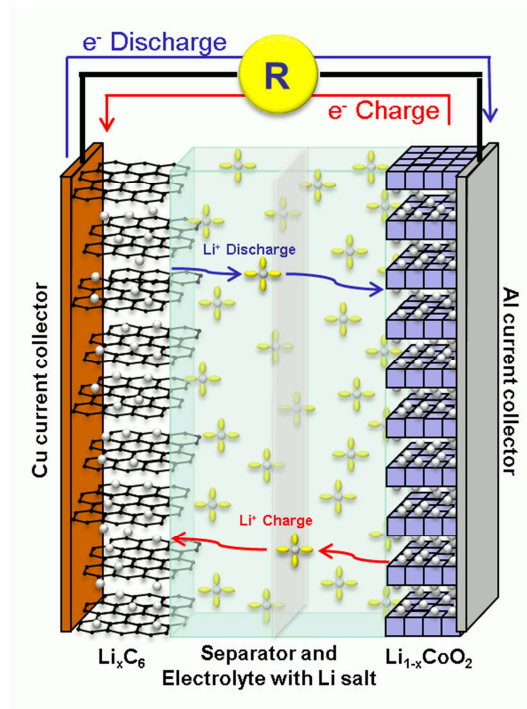


**Figure 4:** Representation of a Li-ion battery based on graphite as anode material and  $\text{LiCoO}_2$  as cathode material.

During the last years, the operating principle of Li-Ion batteries remained unchanged but the researchers developed and studied many innovative materials as alternative to graphite and  $\text{LiCoO}_2$ . **Figure 5** compares some of these materials in terms of specific capacity and operating potential.

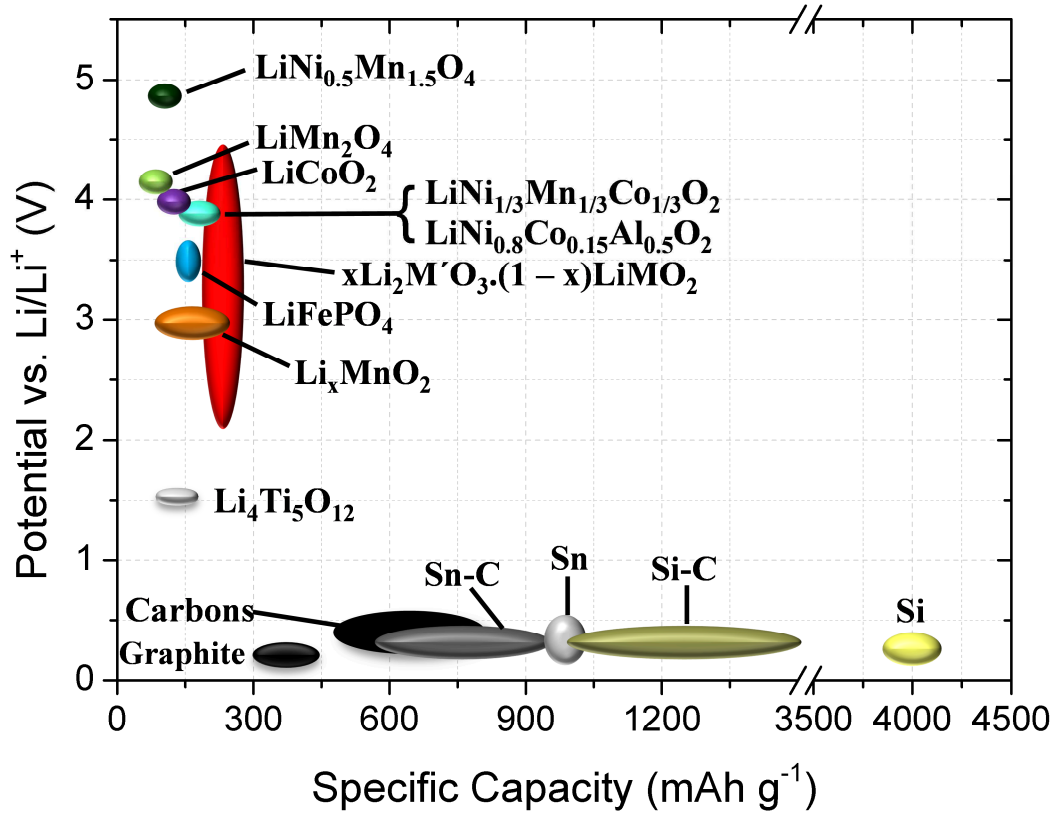


**Figure 5:** Voltage versus capacity for different anode and cathode materials for Li-ion batteries.

So far, graphite remains the main anode material for commercial Li-ion batteries because of its low operating potential, good specific capacity and availability. Some commercial Li-ion batteries replaced graphite with  $\text{Li}_4\text{Ti}_5\text{O}_{12}$  (LTO), which guarantees very high cycling stability and excellent charge and discharge kinetics because of the high  $\text{Li}^+$  mobility in its structure.<sup>15,16,17</sup> The next most promising anode materials are Si or Sn composite materials, which present very high specific capacities and thus significant advantages for the energy density at the cell level.<sup>18,19,20,21</sup>

A different scenario appears for the cathode active materials. The expensive and toxic  $\text{LiCoO}_2$  was gradually replaced by new active materials such as  $\text{LiFePO}_4$  (LFP),  $\text{LiNi}_{0.33}\text{Mn}_{0.33}\text{Co}_{0.33}\text{O}_2$  (NMC),  $\text{LiMn}_2\text{O}_4$  (LMO) and  $\text{LiAl}_{0.05}\text{Ni}_{0.80}\text{Co}_{0.15}\text{O}_2$  (NCA), which are nowadays the state of the art for Li-ion batteries.<sup>22,23,24</sup> Systems based on these materials are successfully adopted for portable electronic devices and also for electric mobile transportation. In this last

application field, the energy and the power of the current Li-ion batteries meet the goal for HEV and PHEV. However, the future of the electric transport are the fully EV, which require higher specific energy (**Figure 6**) and lower cell cost.<sup>25</sup>

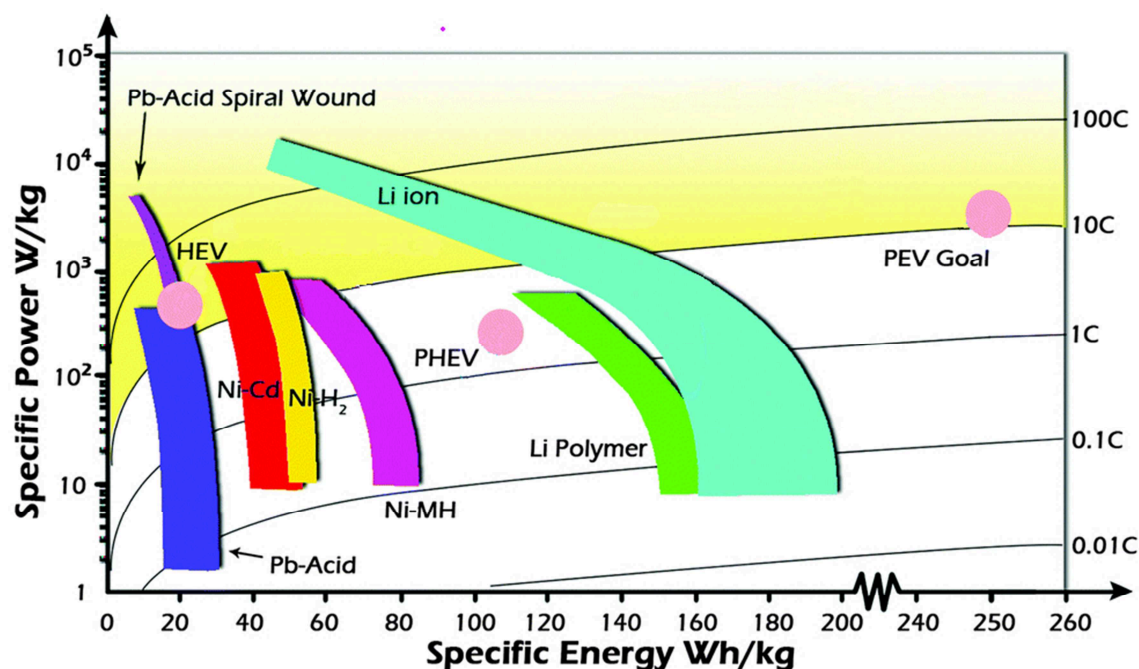


**Figure 6:** Ragone plot comparing different battery technologies. Reproduced (“Adapted” or “in part”) from Chem. Soc. Rev., 2015, 44, 5926 with permission of The Royal Society of Chemistry.<sup>25</sup> License Number: 3871920800244. <http://dx.doi.org/10.1039/c4cs00442f>

According to this prospective, key issues for the next-generation Li-ion batteries are the increase of the specific energy and the reduction of costs by adopting available and eco-friendliness raw materials. This target is achievable by developing new cathode materials, with reduced or absent Co-content, higher operating potential or higher capacity. Among these materials, the spinel structured  $\text{LiNi}_{0.5}\text{Mn}_{1.5}\text{O}_4$  (LMNO) is one of the best candidates for the next generation of Li-ion batteries.<sup>23,24</sup>

## 1.4 High-energy cathode materials

As already mentioned in the previous chapters, adopting high-capacity cathode materials increases the specific energy of Li-ion batteries. Among the cathode materials for Li-ion batteries, layered oxide materials ( $\text{Li}_{1-x}\text{MO}_2$  where  $\text{M} = \text{Co}$ ,  $\text{Ni}$  or  $\text{Mn}$ ) present remarkable specific capacities above  $270 \text{ mAh g}^{-1}$ . Unfortunately, the structure of these materials becomes unstable when deeply delithiated (generally for  $x \geq 0.5$ ) and their actual capacity is limited to a half of the theoretical value.<sup>26,27,28,29,30</sup> For  $\text{M} = \text{Co}$  or  $\text{Ni}$ , the structural instability is due to oxygen losses and to the migration of metal ions into Li-depleted layers. For  $\text{M} = \text{Mn}$ , the deeply delithiated structure converts to the more stable spinel structure. Structural stabilisations of these materials were achieved by introducing the lithium-manganese-rich layered oxides.<sup>31,32</sup> These materials were prepared by including  $\text{Li}_2\text{MnO}_3$  domains in the structure of the pristine layered oxides, obtaining this way a structurally integrated “layered-layered” compound  $(x)\text{Li}_2\text{MnO}_3 \cdot (1 - x)\text{LiMO}_2$ . Recent studies focalised their attention on  $(x)\text{Li}_2\text{MnO}_3 \cdot (1 - x)\text{LiNi}_{1/2}\text{Mn}_{1/2}\text{O}_2$  and on further partially substituted materials adopting small stoichiometric amount of  $\text{Co}$  or  $\text{Cr}$ . These materials deliver a discharge capacity between 250 and 280  $\text{mAh g}^{-1}$  with a maximum value of 310  $\text{mAh g}^{-1}$  reported by T. Ohzuku et al. for  $\text{Li}[\text{Li}_{0.2}\text{Ni}_{0.4}\text{Mn}_{0.6}]\text{O}_2$ .<sup>33</sup>

This class of materials presents different electrochemical behaviours such as a gradual activation during the first cycles. This activation consists in structural rearrangements of the atoms in the structure and leads to a progressive increase of the capacity. Unfortunately, among their electrochemical features, “layered-layered” compounds also present limited capacity retention and gradual reduction of the operating potential upon cycling (**Figure 7**). The reason for this behaviour is the oxygen loss from the guest structure and the progressive and irreversible conversion of the layered phase into spinel phase.<sup>34,35,36,37,38,39</sup>



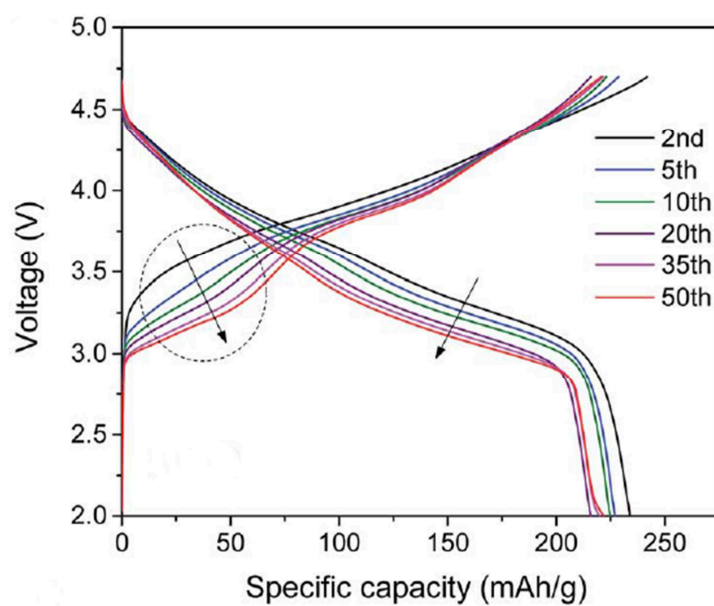


**Figure 7:** Voltage profiles of the  $\text{Li}_{1.2}\text{Ni}_{0.2}\text{Mn}_{0.6}\text{O}_2$  electrodes during cycling. Reproduced (“Adapted” or “in part”) from *J. Mater. Chem. A*, 2015, 3, 9915 with permission of The Royal Society of Chemistry.<sup>39</sup> License Number: 3871970359256. <http://dx.doi.org/10.1039/c5ta01214g>

## 1.5 $\text{LiNi}_{0.5}\text{Mn}_{1.5}\text{O}_4$ as high voltage cathode for Li-ion batteries

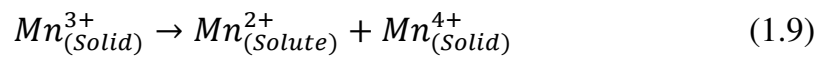
A second approach to increase the energy density of a Li-ion battery consists in increasing the cell voltage. Graphite-based anodes are already optimal electrodes for this purpose because of their operating potential very close to lower limit of 0 V vs.  $\text{Li/Li}^+$ . Increasing the cell voltage requires then new cathode materials operating at higher potential with respect to the standard cathode materials. Suitable classes of materials for high-voltage application are the phospho-olivines  $\text{LiMPO}_4$  (where  $\text{M} = \text{Mn}^{2+}$  or  $\text{Co}^{2+}$ ) and the substituted spinel-type materials  $\text{LiM}_x\text{Mn}_{2-x}\text{O}_4$  (where  $\text{M} = \text{Fe}^{3+}$ ,  $\text{Ni}^{2+}$ ,  $\text{Cr}^{3+}$ ,  $\text{Co}^{3+}\dots$ ) which work at potentials close to 5 V vs.  $\text{Li/Li}^+$ .<sup>40</sup> In particular, the family of the substituted spinel materials is the best candidate for practical application because of their good rate capability and cycling stability.<sup>41,42,43,44</sup> Among the spinel-type materials, Ni-substituted  $\text{LiNi}_x\text{Mn}_{1-x}\text{O}_4$  (LMNO) is the most promising high-voltage material for Li-ion batteries. LMNO presents good theoretical specific capacity ( $147 \text{ mAh g}^{-1}$ ), high-voltage activity at ca. 4.7 V vs.  $\text{Li/Li}^+$  and a 3D spinel structure optimal for Li-ions diffusion.<sup>45,46,47,48,49,50</sup> Furthermore, this material is cheap, Co-free and easy to synthesise.

The stoichiometry of LMNO is adjustable during the synthesis by modifying the Ni content according to the formula  $\text{Li}[\text{Ni(II)}_x\text{Mn(III)}_{1-2x}\text{Mn(IV)}_{1+x}]\text{O}_4$ . Modifications of the Ni content “x” modify the oxidation state of the Mn(III) in the structure and lead to the formation of Mn(IV). LMNOs containing both Mn(III) and Mn(IV) show low-voltage activity (ca. 4 V vs.  $\text{Li/Li}^+$ ) related to the Mn(III)/Mn(IV) red/ox couple and a high-voltage activity (ca. 4.7 V vs.  $\text{Li/Li}^+$ ) related to the Ni(II)/Ni(IV) red/ox couple. In the case of  $x = 0.5$  (fully-substituted spinel) all the manganese in the structure converts to Mn(IV) and the material presents only the high-voltage activity related to the Ni(II)/Ni(IV) red/ox couple (**Figure 8a**).

It is possible to vary the stoichiometry of LMNO, and thus the Mn(III) content, also by introducing oxygen deficiencies in the structure. The introduction of

oxygen deficiencies is possible by applying appropriate secondary thermal treatments, which consist in re-calcinations of LMNO at high temperature (e.g. 800 °C) followed by fast cooling down.<sup>51,52</sup> Considering the fully-substituted LMNO ( $\text{LiNi}_{0.5}\text{Mn}_{1.5}\text{O}_4$ ), introducing oxygen deficiencies ( $\delta$ ) modifies the stoichiometry of the material according to the formula  $\text{Li}[\text{Ni(II)}_{0.5}\text{Mn(III)}_{2\delta}\text{Mn(IV)}_{1.5-2\delta}]\text{O}_{4-\delta}$ . As reported in **Figure 8b**, oxygen-deficient LMNOs show both the 4 V plateau related to the presence of Mn(III) and the high-voltage plateaus typical for the Ni(II)/Ni(IV) redox couple. Moreover, oxygen-deficient LMNOs present partially disordered spinel structure described by the *Fd-3m* space group (**Figure 8d**), which differs from the highly-ordered structure (space group *P4<sub>3</sub>32*) typical for stoichiometric  $\text{LiNi}_{0.5}\text{Mn}_{1.5}\text{O}_4$  (**Figure 8c**).<sup>53,54,55</sup> The introduction of oxygen deficiencies in a stoichiometric material is a reversible process. It is possible to restore the initial oxygen content via long annealing at high temperature (e.g. 700 °C for 48 h) followed by slow cooling down.<sup>53</sup>

The fully-substituted and stoichiometric  $\text{LiNi}_{0.5}\text{Mn}_{1.5}\text{O}_4$  is an attractive choice for cathode material application in Li-ion batteries. The absence of Mn(III) guarantees an operating potential of 4.7 V vs.  $\text{Li/Li}^+$  which is beneficial for the final cell energy. In addition, the tetravalent manganese avoids the Jahn-Teller distortion typical for Mn(III)-containing materials and it also reduces the aging phenomena related to manganese disproportion and dissolution in the electrolyte:  
56,57,58,59,60,61



The stoichiometric phase seems anyway to present lower ionic and electronic conductivity with respect to the not-stoichiometric ones.<sup>62,63</sup>

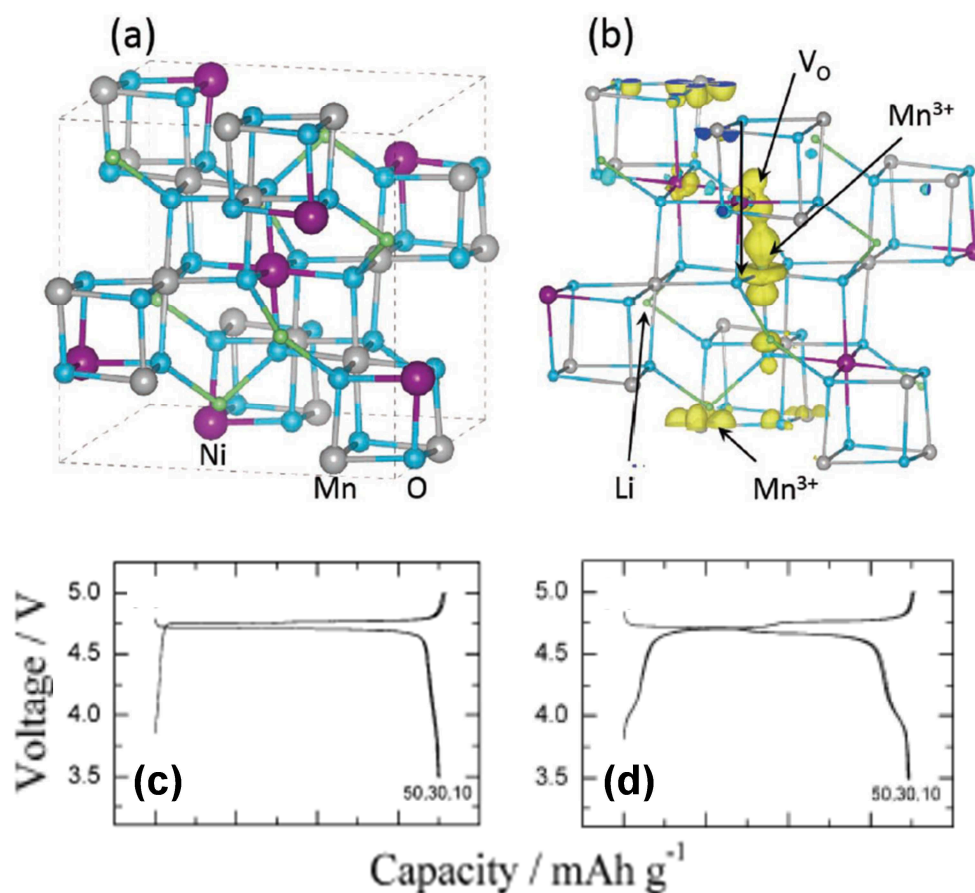


**Figure 8:** Representation of (a) fully-stoichiometric spinel structure and (b) oxygen-deficient spinel structure. Reproduced with the permission from *Adv. Mater.* 2012, 24, 2109-2116. Copyright 2012 WILEY-VCH Verlag GmbH & Co. KGaA.<sup>64</sup> License Number: 3872450012137. Voltage vs. capacity curves for (c) LiNi<sub>0.5</sub>Mn<sub>1.5</sub>O<sub>4</sub>, (d) LiNi<sub>0.5</sub>Mn<sub>1.5</sub>O<sub>4-δ</sub>. Adapted with permission from *Chem. Mater.* 2004, 16, 906-914. Copyright 2004 American Chemical Society.<sup>53</sup>

The main problem related to high-voltage materials is the instability of standard electrolytes at high potentials versus Li/Li<sup>+</sup>. The electrolytes for Li-ion batteries are generally mixtures of Li-salts (e.g. LiPF<sub>6</sub>) and organic solvents such as ethylene carbonate (EC), Dimethyl carbonate (DMC), diethyl carbonate (DEC), ethyl methyl carbonate (EMC) and propylene carbonate (PC). Both the lithium salt and the organic compounds start to decompose at potentials above 4.5 V vs. Li/Li<sup>+</sup>. The onset potential and the products of these decomposition phenomena depend both on the electrolyte mixture (e.g. EC:DMC mixtures results more stable than other mixtures) and on the material used as working

electrode.<sup>65</sup> For instance, adopting Pt as working electrode, the electrolyte degradation occurs at different potentials than using Al or active materials such as Ni-substituted spinels. The mechanism of the electrolyte decomposition on LMNO electrodes was extensively investigated in the past years and it has been possible to identify the principal by-products form.<sup>66,67,68,69</sup> The degradation process leads to a large variety of compounds such as Polycarbonates, LiF,  $\text{Li}_x\text{PO}_y\text{F}_z$ ,  $\beta$ -diketonate, Ni(II) and Mn(II)/(III) complexes, Ni(II) and Mn(II) oxalates and carbonates. The formed by-products can both depose on the cathode as a film and dissolve in the electrolyte reaching all the cell components.<sup>66,67,68,69,70</sup> For this reason, the aging of a high-voltage Li-ion cell strongly differs from what observed in a standard Li-ion cells. In standard Li-ion cells, the anode (graphite) works outside the potential stability window of the organic electrolytes. Nevertheless, during the first charge/discharge cycles, part of the electrolyte decomposes on the surface of the anode forming a passivation layer called Solid Electrolyte Interface (SEI). This SEI stabilises the anode and blocks further electrolyte decomposition. On the cathode side, the potential does not overcome the stability window of standard organic electrolytes and does not lead to significant electrolyte decomposition. In a high-voltage Li-ion cell, both the anode and the cathode work outside the stability window of standard organic electrolytes. During the first charge/discharge cycles of these cells, part of the electrolyte decomposes both at the anode forming the SEI and at the cathode forming passivation films and soluble decomposition by-products. The dissolved by-products are free to diffuse in the cell and reach the anode surface, where they further react and compromise the quality of the SEI. Keeping cycling, the electrolyte decomposition still occurs both on the anode and on the cathode, leading to continuous film thickening, by-products formation, SEI damaging and thus charge consumption. Additionally, using LMNO as cathode material leads to Mn dissolution (lower for stoichiometric materials), which contributes to all the above mentioned aging phenomena.<sup>71,72,73,74,75,76</sup>

Optimising the morphology of LMNO particles is a valid strategy to limit the electrolyte decomposition rates. This way, it is possible to reduce the surface

reactivity of the active material and guarantee at the same time the required electrochemical performance. A second valid strategy to stabilise the active material/electrolyte interface of LMNO consists in coating the particles with a thin layer of a coating material. In this case, the selected material must present suitable characteristics such as good ionic conductivity and good stability on the particles surface. Different coating materials present these properties and have been already reported in literature (e.g.  $\text{Bi}_2\text{O}_3$ ,  $\text{Al}_2\text{O}_3$ ,  $\text{AlPO}_4$ ,  $\text{ZrO}_2$ ,  $\text{SiO}_2$ ,  $\text{MgF}_2$ ,  $\text{Li}_3\text{PO}_4$ ) obtaining different effects on the electrochemical behaviour of the pristine material.<sup>77,78,79,80,81</sup>

The scientific effort and the growing interest in high-voltage systems based on  $\text{LiNi}_{0.5}\text{Mn}_{1.5}\text{O}_4$  underline the importance of studying this innovative cathode material. Every single contribution in understanding and improving LMNO cathodes is a step forward in the direction of cheaper and more performing energy storage systems.

## 2. AIMS OF THE THESIS

This thesis includes results from the project “Funktionsmaterialien und Materialanalytik zu Lithium-Hochleistungsbatterien” founded by the German Research Association (DFG) and the project “Advanced High Performance Polymer Lithium Batteries for Electrochemical Storage” (APPLES) founded by the European community. These projects aimed to investigate materials for high-energy and performing Li-Ion batteries. These kinds of batteries are the key for a sustainable mobile transport based on innovative electric vehicles and thus, their feasibility attracts the attentions of both research and industry.

The purpose of this work is to study an innovative and morphologically optimised LMNO as promising cathode material for stable and performing high-voltage Li-ion cells.

The first part of this scientific work wants to explore the relationship between material features and electrochemical behaviour of LMNO. Fundamental characteristics such as particle architecture, crystallite size and particle dimension are the first and most important instrument for tuning the electrochemical behaviour and the technological features of new active materials. Only by optimising the particle morphology of LMNO it is possible to increase its electrochemical performance, reduce the electrolyte decomposition phenomena and obtain powder density in line with commercial cathode materials. Realising stable high-voltage Li-ion batteries is a task that goes also beyond the optimisation of the single cathode material and requires a careful investigation of the entire electrochemical system. For this reason, the second part of the work aims to point out key strategies to improve the cycling life of graphite/LMNO full Li-ion cells. This task includes also the study of  $\text{LiNbO}_3$  as coating material for LMNO and its effects on the full cells aging.

The entire work also takes in account technological aspects such as materials processability and density, electrodes loading and operating conditions, in order to give a real contribution to the state of the art of these promising systems.

## 3. EXPERIMENTAL

### 3.1 Materials

#### 3.1.1 $\text{LiNi}_{0.5}\text{Mn}_{1.5}\text{O}_4$

As discussed in *Chapter 1.5*, stoichiometric  $\text{LiNi}_{0.5}\text{Mn}_{1.5}\text{O}_4$  is one of the most promising candidates as high-voltage cathode material for Li-ion batteries. This cathode material presents operating potential of ca. 4.7 V vs.  $\text{Li/Li}^+$  and  $147 \text{ mAh g}^{-1}$  theoretical specific capacity. Additionally, the 3D spinel structure (**Figure 9**) facilitates the  $\text{Li}^+$  diffusion during the intercalation/deintercalation processes.

The availability of the raw materials and the absence of Co make this material rather cheap. Furthermore, synthesis of LMNO is easy and suitable for large-scale application.

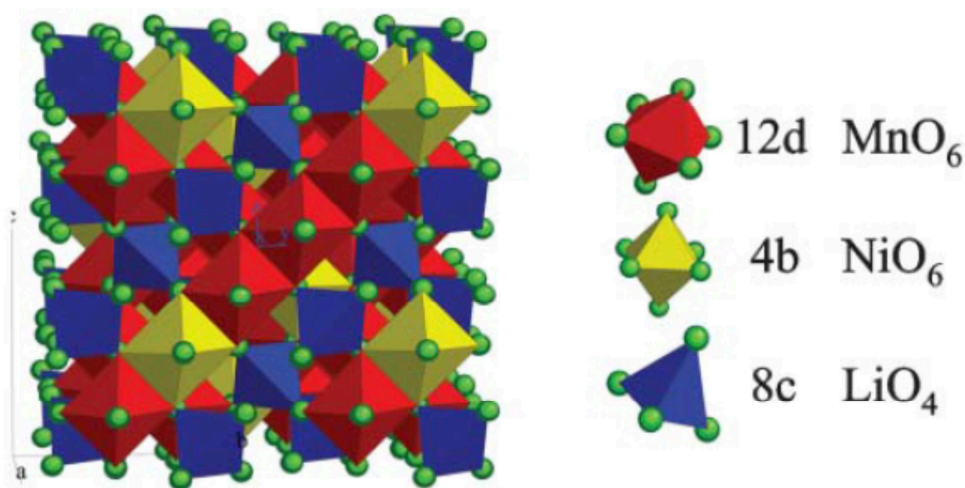


**Figure 9:** Representation of the spinel structure  $\text{LiNi}_{0.5}\text{Mn}_{1.5}\text{O}_4$ . Reproduced (“Adapted” or “in part”) from *J. Mater. Chem.*, 2007, 17, 3668–3677 with permission of The Royal Society of Chemistry.<sup>82</sup> Licence Number: 3874820112217. <http://dx.doi.org/10.1039/b707040n>



The materials studied in this work were synthesised according to a continuous two-steps method consisting in: precipitation of mixed manganese-nickel precursors and calcination in presence of Li salt. The precursors were obtained in alkaline environment from aqueous solutions of ammonia containing Ni and Mn nitrates (1:3 stoichiometric ratio). The obtained precursor underwent a calcination step at 700 °C for 10 h together with LiOH as lithium precursor. Finally, the calcined material was slowly cooled down to room temperature in order to reach the final oxygen stoichiometry. This synthesis allows controlling the transition metal stoichiometry within a short range, described by the formula  $\text{LiNi}_{0.5-y}\text{Mn}_{1.5+y}\text{O}_4$  ( $0 \leq y \leq 0.02$ ).

The crystallite size strongly affects the kinetics of the active materials. Thus, part of the stoichiometric  $\text{LiNi}_{0.5}\text{Mn}_{1.5}\text{O}_4$  underwent a secondary thermal aiming to increase the size of the primary crystallites. This secondary thermal treatment consisted in calcining the pristine LMNO at 800 °C for 5 h and then annealing it at 700 °C for 48 h in order to reinstate of the oxygen stoichiometry in the final material (LMNO-T1).

The material used in *Chapter 5* as reference material (LMNO-R) was a  $\text{LiNi}_{0.5}\text{Mn}_{1.5}\text{O}_4$  purchased from Sigma-Aldrich. The material was dried under vacuum at 100 °C before using.

### **3.1.2 $\text{LiNi}_{0.5}\text{Mn}_{1.5}\text{O}_{4-\delta}$**

*Chapter 1.5* described the effects of introducing oxygen deficiencies in the LMNO structure. These oxygen deficiencies influence the electrochemical behaviour of LMNO and are an interesting modification for a comprehensive investigation of the material.

Variations in the oxygen stoichiometry of LMNO were obtained by secondary thermal treatments at high temperature. Calcinations of the stoichiometric LMNO for 1 h at 800 °C allow introducing oxygen deficiencies in the structure

without significant increase the crystallite size. The cooldown step determines the amount of oxygen deficiencies remaining in the structure of the final material. Slow cooldown rates leave lower amount of oxygen deficiencies in the structure (LMNO-T2), while direct quenching in air leads to higher amount of oxygen deficiencies in the final material (LMNO-T3).

### ***3.1.3 LiNbO<sub>3</sub>-treated LiNi<sub>0.5</sub>Mn<sub>1.5</sub>O<sub>4</sub>***

As discussed in *Chapter 1.5*, the main problem in operating at high potential versus Li/Li<sup>+</sup> is the electrolyte degradation occurring at the cathodes surface. A possible strategy for inhibiting the electrolyte decomposition phenomena consists in coating the surface of LMNO particles with a suitable material.

In this work, lithium niobate (LiNbO<sub>3</sub>) is studied as coating material for LMNO with the purpose of stabilising the active material/electrolyte interface. The choice of LiNbO<sub>3</sub> depends on its interesting properties such as high ionic conductivity ( $10^{-6}$  S cm<sup>-1</sup> at 293 K), low coating resistances, reduction of the Mn dissolution phenomena and stability at the LMNO operating conditions.<sup>83,84,85,86,87</sup>

The surface of LMNO was coated with LiNbO<sub>3</sub> by following an easy and low temperature method consisting in: impregnation of LMNO powders with an ethanol solution of CH<sub>3</sub>CH<sub>2</sub>OLi (lithium ethoxide) and Nb<sub>2</sub>(OCH<sub>2</sub>CH<sub>3</sub>)<sub>10</sub> (niobium ethoxide), drying of the impregnated powders in air and thermal treatment at 350°C for 30 minutes.<sup>88</sup> The ethoxides used as precursors are expected to form LiNb(OCH<sub>2</sub>CH<sub>3</sub>)<sub>6</sub> on the surface of LMNO particles when handled under inert atmosphere. The following contact with air and heat treatment lead to the hydrolysis of LiNb(OCH<sub>2</sub>CH<sub>3</sub>)<sub>6</sub> and to the formation of LiNbO<sub>3</sub>, respectively.<sup>89,90,91</sup>

### 3.1.4 Graphite

Graphite is the most common anode active material for Li-ion batteries. The success of graphite as anode material depends on its high theoretical specific capacity ( $373 \text{ mAh g}^{-1}$ ), good cycling stability, high electronic conductivity, low cost and large availability of the raw material.

Graphite is made of graphene layers stacked on each other according to an AB sequence (**Figure 10a**). Ordered graphite can intercalate one lithium atom each six carbon atoms, accommodating the guest atoms between the graphene layers. The intercalation of Li atoms is governed by the energy required to open gaps between the graphene layers. For this reason, the guest atoms occupy preferential sites in the structure and graphite passes through four different phases during the intercalation process (**Figure 10b**).<sup>92</sup>

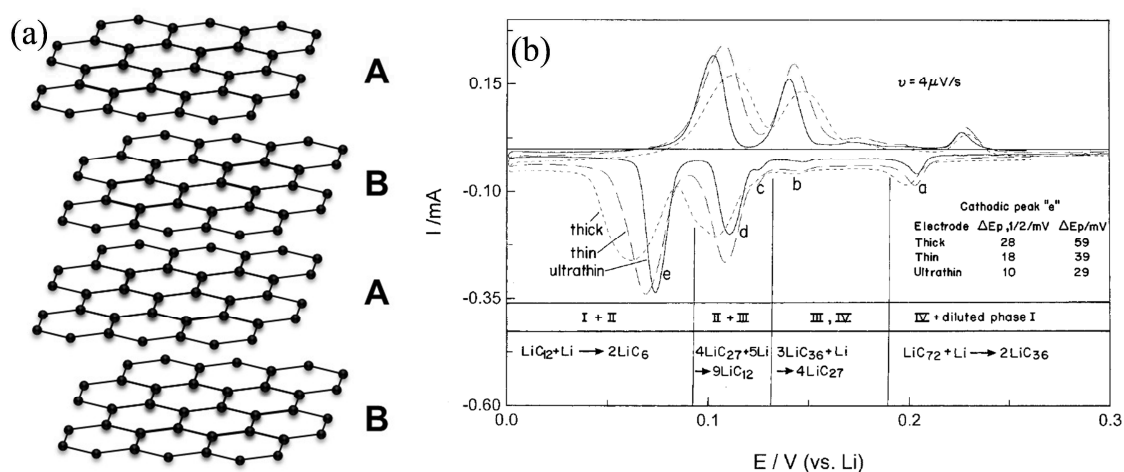


**Figure 10:** (a) Stacking of graphene layers in graphite and (b) Current vs. potential plot for a graphite anode and Li intercalation stages. Adapted with permission from *J. Phys. Chem. B* 1997, 101, 4630-4640. Copyright 1997 American Chemical Society.<sup>92</sup>

As already mentioned in *Chapter 1.5*, the operating potential of graphite is very close to the redox potential of lithium. Standard organic electrolytes are not stable at such low potential and therefore, they decompose on the surface of the graphite anode forming the SEI. The formation of the SEI stabilises the graphite anode in the next cycles, but it also consumes part of the charge available in the

cell. For this reason, commercial graphite for Li-ion batteries has very high electrochemical performance and guarantees low charge losses related to the SEI formation process.

Because of its very low operating potential, graphite is a very interesting anode material also for high-voltage application. Graphite anodes guarantee the highest cell voltage achievable together with LMNO cathodes in a full cell and thus, lead to consistent increase of the energy density.

The graphite used in this work is a commercial material type SMG from Hitachi. This graphite was dried overnight at 130 °C under vacuum before using.

## **3.2 Analytical Methods**

### ***3.2.1 Inductively Coupled Plasma - Optical Emission Spectroscopy (ICP-OES)***

ICP-OES is a spectroscopic technique performed on atoms excited or ionised by a plasma torch. These species emit typical electromagnetic signals, which allow their direct identification. The ICP-OES allows also quantitative analyses by evaluating the intensity of the emitted electromagnetic emissions.

In this work ICP-OES analysis were performed with a SPECTRO ARCOS High Resolution ICP-OES spectrometer (SPECTRO Analytical Instruments GmbH). The instrument adopts a quartz plasma torch and an array of 32 CCD detectors with an overall wavelength detection range between 130 and 770 nm. This instrument is designed for liquid state analysis, thus solid-state samples were prepared according to the following method: 250 mg of the selected material were dissolved under heating in an acid solution (3 ml HCl + 1 ml HNO<sub>3</sub>) and then diluted with Millipore H<sub>2</sub>O up to 50 ml of volume. The obtained solution was cooled-down to 20 °C and analysed.

### ***3.2.2 Laser diffraction analysis***

Laser diffraction analyses are widely adopted for determining the particle size distribution of powders suspended in solutions. This technique consists in projecting a laser beam through a suspension containing the desired sample and analysing the resulting scattered light. Larger particles scatter the laser light at lower angles, while smaller particles scatter it at larger angles. The instrument can evaluate the diffracted light signals and calculates the overall particle size distribution of the sample.

In this work, the particle size distribution was determined with a Mastersizer MICRO analyser (Malvern Instruments). The sample preparation consisted in dispersing the powders of the desired sample in Millipore H<sub>2</sub>O until obtaining a laser beam obscuration of ca. 20 %.

### 3.2.3 Nitrogen adsorption porosimetry

Nitrogen adsorption porosimetry is a technique based on the physisorption of liquid nitrogen on the surface of materials. This technique is widely used to evaluate the surface area and porosity of the analysed samples.

The analysis procedure consists in injecting known amount of N<sub>2</sub> (at a temperature of 77 °K) on the sample and measuring the value of the equilibrium pressure reached. Plotting the volume of adsorbed/desorbed N<sub>2</sub> as function of the relative pressure  $p/p^0$  (ratio between the measured pressure  $p$  and the vapour pressure of liquid nitrogen  $p^0$ ), it is possible to graphically represent adsorption/desorption isotherms (**Figure 11**).

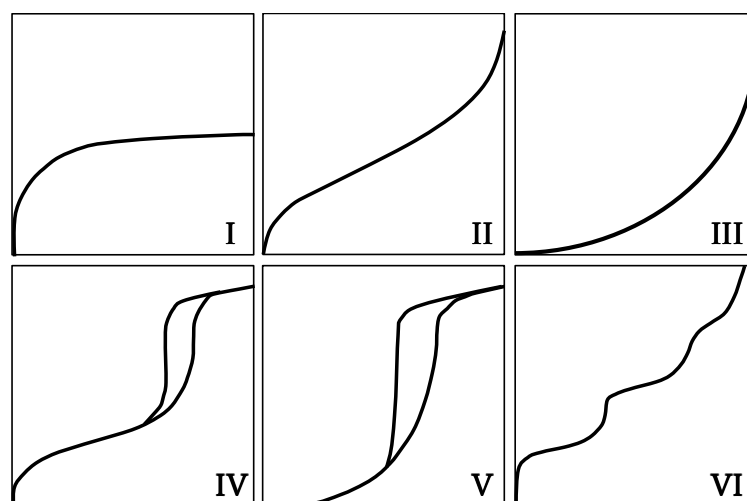


**Figure 11:** Types of physisorption isotherms.

The shape of the isotherms depends on the interactions between the samples' surface and the injected N<sub>2</sub>. For instance, Type I isotherms are typical for microporous samples with small external surface, Type II are related to non-porous or microporous samples and Type IV regard mesoporous samples, where a capillary condensation leads to the appearance of a hysteresis loop. One of the most diffused theories to interpret the surface/gas interactions is the Brunauer-Emmett-Teller (BET) theory, which expands the Langmuir theory admitting also the formation of multilayers. According to the BET, it is possible to determine the surface area of the investigated samples.

The samples here reported were investigated with a Sorptomatic 1990 porosimeter from Thermo Electron Component. Before the analysis, the materials were degassed under vacuum at 150 °C for 10 h. The surface areas were calculated evaluating the isotherms between 0.05 and 0.33 p/p<sup>0</sup> according to the BET theory.

#### ***3.2.4 Scanning Electron Microscopy (SEM) and Energy Dispersive X-ray Spectroscopy (EDX)***

The SEM is a powerful technique, which allows detailed investigation of materials surface. The scanning electron microscope irradiates a sample with an electrons beam and evaluates the signals generated from the interactions between beam and samples surface. The electrons beam can inelastically interact with the atoms of a sample, inducing this way the emission of secondary electrons. A microscope equipped with a suitable detector can collect these low energy electrons and generate an image of the samples surface.

Scanning electron microscopes can also include an X-rays detector. In this case, it is possible to determine the atomic composition of samples surface by performing the Energy Dispersive X-ray Spectroscopy (EDS or EDX). This technique employs the electrons beam for removing electrons from the internal shells of the atoms. This ionisation induces another electron from higher levels to

fill the vacancy releasing energy in form of X-rays (**Figure 12**). These X-ray emissions depend on the electronic structure of the ionised atoms and allow the identification of the species on samples surface.

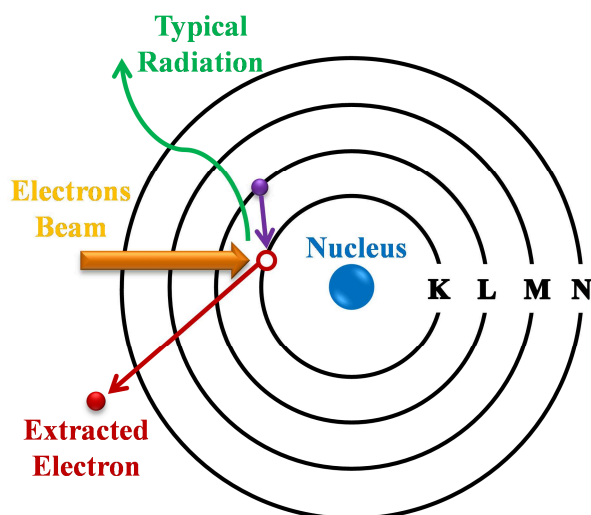


**Figure 12:** Radiation emission principle in the Energy Dispersive Spectroscopy.

The microscope used in this work is a Leo 1530 VP using a field emission electron gun (Tungsten) as electron source. This microscope was equipped with both a detector for secondary electrons and a detector for X-rays. The electrons in the beam were accelerated with a voltage between 10 – 20 kV. All the measurements were performed in a vacuum chamber with a pressure in the order of  $10^{-6}$  mbar.

### 3.2.5 Tap-density

The tap-density of powders depends on the particles density and on their capacity to pack together. Li-ion batteries require active materials with high tap-density in order to guarantee good processability and high electrode loadings. The processability of active materials influences the quality of the final electrodes and the quantity of resources needed for their realisation (e.g. energy and solvents).



The electrodes loading is beneficial for the specific energy ( $\text{Wh kg}^{-1}$ ) and energy density ( $\text{Wh L}^{-1}$ ) of the final cell.<sup>93,94,95,96,97</sup>

In this work, the tap-density of the active materials was determined by tapping the samples powders 2500 times with a JEL jolting volumeter STAV 2003. The tap-density value ( $\text{mg cm}^{-3}$ ) was then calculated dividing the volume of the sample at the end of tapping by its mass.

### 3.2.6 X-ray diffraction on powders (XRD)

XRD analyses use a monochromatic X-rays beam to irradiate the powders of the desired sample and collect structural information from the intensity and the position of the diffracted radiation. The radiations diffracted by the atoms in different lattice planes interact with each other leading to constructive and destructive interferences (**Figure 13**).

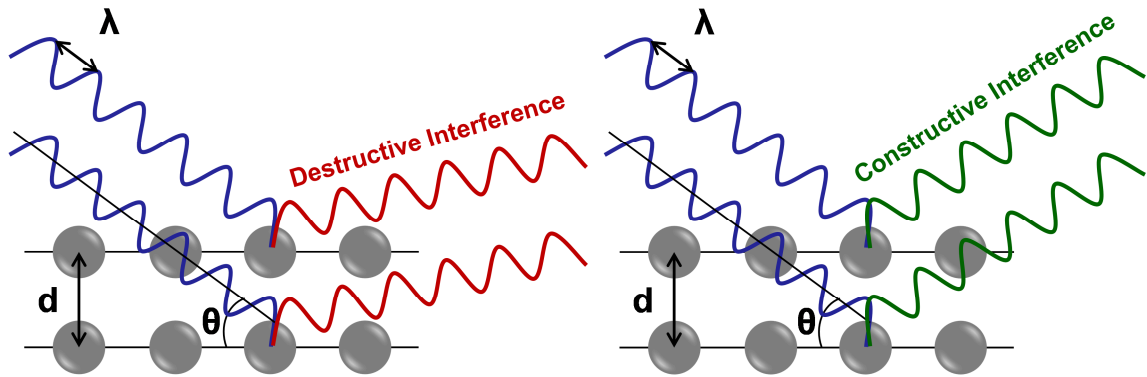


**Figure 13:** Lattice leading to a destructive interference (left) or to a constructive interference (right) of the diffracted X-rays.

The Bragg's law describes the conditions for constructive or destructive interferences according to the equation:

$$n\lambda = 2d \sin \theta \quad (3.1)$$

Where  $n$  is a positive integer number,  $\lambda$  is the wavelength of the X-radiation,  $d$  is the distance between the planes in the lattice and  $\theta$  is the angle between the X-radiation and the surface of the lattice plane. Each crystalline phase presents a unique combination of atoms in the lattice and generates a typical diffraction pattern, which allows its direct identification. Additionally, XRD analyses allow calculating the crystallites size ( $D$ ) according to the Scherrer's equation:

$$D = \frac{0.9\lambda}{\beta \cos \theta} \quad (3.2)$$

Where  $\lambda$  is the wavelength of the X-radiation,  $\beta$  is the full width at half maximum of the diffraction peak and  $\theta$  is the angle between the X-radiation and the surface of the lattice plane.

In this work, all XRD analyses were performed on a Siemens D5000 diffractometer with an X-rays source based on the Cu K $\alpha$  radiation (0.154 nm).

### 3.3 Electrodes Preparation

LMNO electrodes were prepared both on small scale and on large scale. Small scale preparations consisted in coating a dispersion of N-methylpyrrolidone (NMP), LMNO, carbon black (Timcal, Super P) and polyvinylidene fluoride (Solvay, Solef 5130) on Al foil (used as current collector). The dispersions were coated via the “doctor blade” technique controlling the electrodes loading by adjusting the blade height. The ratio between LMNO, carbon black and polyvinylidene fluoride was set according to the purpose of the preparation. The coated Al foil was dried overnight at 45 °C and then punched into circular electrodes (area of 1.13 or 2.01 cm<sup>2</sup>). The obtained electrodes were pressed at 5 tons cm<sup>-2</sup>, dried overnight at 130 °C under vacuum and finally transferred in an Ar-filled glovebox with O<sub>2</sub> and H<sub>2</sub>O concentration below 0.1 ppm.

The large-scale preparation consisted in coating the LMNO dispersions with a large-scale coater (Lacom) working with minimum 1 kg of active material per batch. In this case, the LMNO : carbon black : polyvinylidene fluoride ratio was fixed to 88 : 8 : 4 wt.%. The coated Al foil was dried and then calendared at 100 °C applying a force of 250 N. Circular electrodes (2.01 cm<sup>2</sup> area) were punched from the coating, pressed at 0.5 tons cm<sup>-2</sup> and dried overnight at 130 °C under vacuum. The dried electrodes were transferred in an Ar-filled glovebox with O<sub>2</sub> and H<sub>2</sub>O concentration below 0.1 ppm.

Graphite anodes were prepared according to the large-scale preparation described above. The graphite dispersion consisted in 90 wt.% graphite and 10 wt.% polyvinylidene fluoride. The current collector was in this case Cu foil. The electrodes punched from this coating (area 2.01 cm<sup>2</sup>) were pressed at 0.25 tons cm<sup>-2</sup>, dried and stored in glovebox as already described for LMNO electrodes.

## 3.4 Electrochemical Characterisation

### 3.4.1 Cells configurations

#### 3.4.1.1 T-Cells

T-Cells are commonly used for basic electrochemical studies. This kind of cells has T-shaped form, which allows using a working electrode (WE), a counter electrode (CE) and a reference electrode (RE) as shown in **Figure 14**. According to this cell geometry, the WE directly faces the CE, while the RE takes its place in the upper part of the cell without touching the other electrodes. In order to avoid shortcuts, one or more separators soaked with the desired electrolyte stand between the WE and the counter CE. An excess of electrolyte fills the empty spaces in the cell and keeps all the electrodes wet. The three electrodes are connected with the outside by metallic pistons, which also seal the cell and keep the electrodes in the right position.

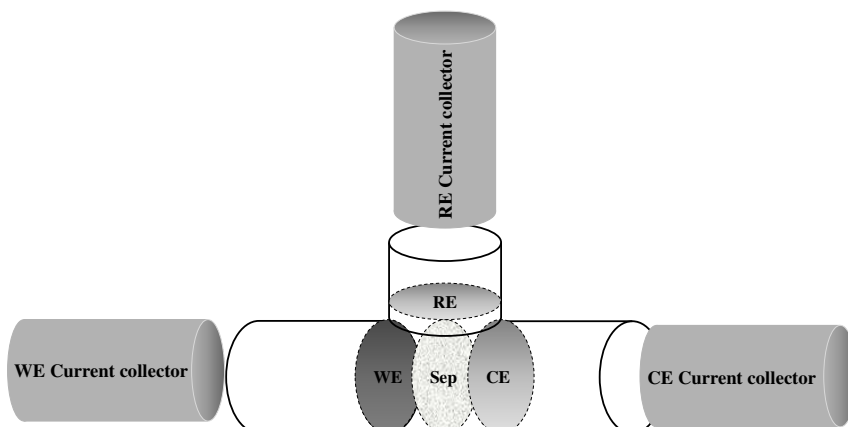


**Figure 14:** Schematic representation of a T-Cell.

The T-Cells used in this work were assembled in half-cell configuration, using circular electrodes ( $1.13\text{ cm}^2$  area) as WE and metallic Li discs (also  $1.13\text{ cm}^2$  area) as CE and WE. The electrolyte was a mixture of EC:DMC (1:1 wt.) + 1 M  $\text{LiPF}_6$  (from UBE, Japan). Three discs of glass fibre (Whatman GF/A)

soaked with the electrolyte were used as separator. The cells were assembled in an Ar-filled glovebox with O<sub>2</sub> and H<sub>2</sub>O concentration below 0.1 ppm.

### 3.4.1.2 Coin cells

The coin cells (or button cells) are single-cell batteries mainly adopted in small portable devices. These cells accommodate only WE and CE without any additional RE. **Figure 15** shows a representation of the various cell components and their position in the final cell. The assembling procedure of coin cells is easy and consists in staking the various components in the right order. The WE lays inside the can in order to expose the coated face to two (for half-cells) or three (for full cells) separators (GF/A Whatman). The CE (metallic Li discs for half-cells or graphite anodes for full cells) lays face down on the separators. Finally, a metallic spacer and a metallic spring complete the upper part of the stack. The can containing the stack is then filled with electrolyte (EC:DMC 1:1 wt. + 1 M LiPF<sub>6</sub>), closed with a metallic cap and sealed using a crimping tool.

The coin cells used for this work were MTI Al-Clad CR2032 Coin Cell assembled in an Ar-filled glovebox (O<sub>2</sub> and H<sub>2</sub>O concentration below 0.1 ppm) and used for long-term stability tests and two-electrode impedance spectroscopy on full cells.

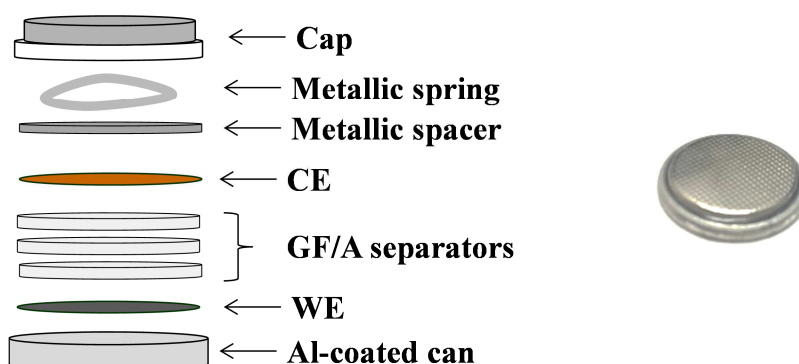


**Figure 15:** (left) representation of the coin cells components, (right) coin cell ready for using.

### 3.4.1.3 ECC-Ref electrochemical cells

ECC-Ref (EL-CELL GmbH<sup>98</sup>) are electrochemical cells suitable for research applications. These cells present the same geometry of coin cells but they also include a reference electrode (**Figure 16**).

ECC-Ref cells were assembled by stacking the WE, four glass fibre separators (GF/A from Whatman), the CE and a piston in the same order described for coin cells. When the cell is closed, a golden spring presses the stack applying a reproducible force on it. The RE consisted in a tip of metallic lithium stuck on a metal pin and facing the separators between WE and CE (**Figure 16**, left side). The electrolyte was again a mixture of EC:DMC (1:1 wt.) + 1 M LiPF<sub>6</sub> (from UBE, Japan). The cell design and the position of the RE make these cells the system of choice for three-electrode impedance measurements.

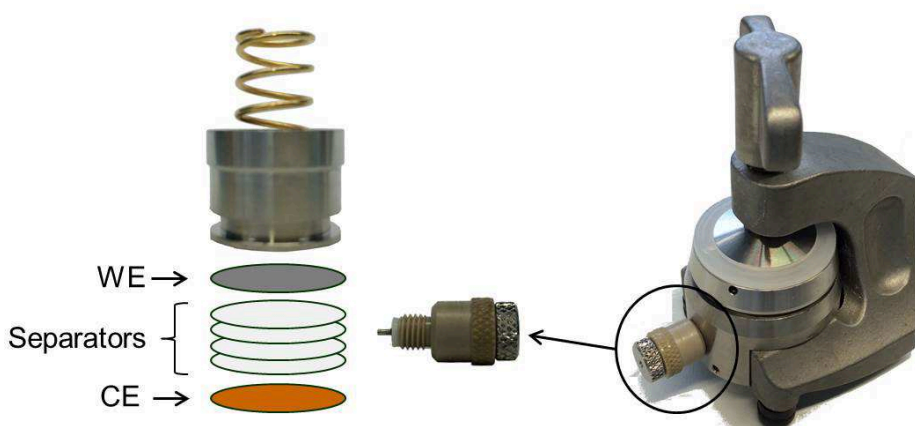


**Figure 16:** ECC-Ref cell from EL-CELL.

## 3.4.2 Electrochemical Techniques

### 3.4.2.1 Galvanostatic charge/discharge cycling

Galvanostatic charge/discharge cycling is a diffused technique for evaluating electrochemical performances and cycling stability of batteries. This technique

consists in cyclically increase and decrease the cell potential between two limit values by applying a constant current.

In full cells, the “charge” process occurs when the cathode undergoes an oxidation reaction (Li extraction) and the anode undergoes a reduction reaction (Li insertion). In this case, the current applied to the cathode is positive and the cell voltage varies from an initial value  $E_i$  to a final value  $E_f$ . The “discharge” of a full cell is the inverse process, occurring when the current flows in the opposite direction. In this case, the cell voltage varies from the  $E_f$  value to the  $E_i$  value. Charge and discharge together correspond to one galvanostatic cycle (**Figure 17**), while  $E_i$  and  $E_f$  are the lower and the upper cell cut-offs, respectively.

It is possible to extend the concept of “charge” and “discharge” also to half-cells. In this case, the “charge” corresponds to the oxidation of the investigated electrode (Li extraction) and accordingly, the “discharge” corresponds to the reduction (Li insertion).

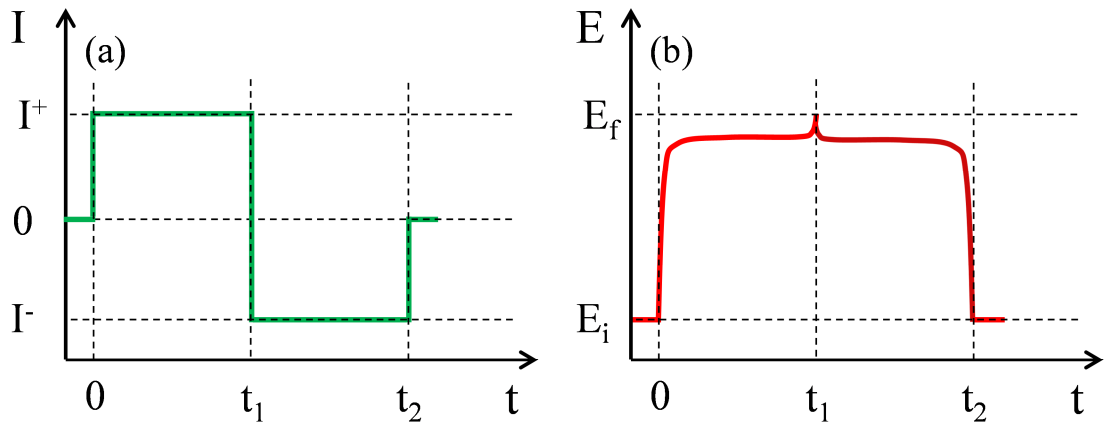


**Figure 17:** (a) Current variation in function of the time and (b) voltage variation in terms of time during a charge/discharge cycling test.

In the battery field, the current is often defined in terms of “C-rate”. Applying a current (or a C-rate) of 1C, the cell delivers (discharge) or accumulate (charge) all its capacity in one hour. Accordingly, multiples or fractions of C define higher or lower currents, respectively. For instance, a C-rate of 2C corresponds to twice the current of C (complete charge or discharge in 30 minutes), while a C-rate of

0.5C (or C/2) corresponds to half the current of C (complete charge or discharge in two hours).

Along with the electrochemical performance and the cycling stability, charge/discharge cycling tests allow determining the coulombic efficiency of a system. The coulombic efficiency is the ratio between discharge and charge capacity (often expressed in percentage) and defines the amount of reversible capacity obtained at the end of each galvanostatic cycle.

The here reported charge/discharge cycling tests were performed on three-electrodes, two-electrode, half- and full cells. Half-cells were always tested at room temperature (RT), while full cells were tested both at RT and at 45°C. The instruments used for charge/discharge cycling tests were either a VMP-3 Potentiostat/Galvanostat from BioLogic Science Instrument (France) or a cell test system from BaSyTech GmbH (Germany).

#### 3.4.2.2 Linear Sweep Voltammetry (LSV)

The Linear Sweep Voltammetry (LSV) is a potentiodynamic electrochemical technique consisting in a linear potential scan of an electrode. The potential scan runs from an initial value  $E_i$  to a final value  $E_f$  as illustrated in **Figure 18a**. During the measurement, a potentiostat guides the potential sweep according to a defined scanning rate. At the same, it measures the current variations related to eventual electrochemical processes occurring at the electrode interface (**Figure 18b**). LSV measurements allow evaluating the different redox reactions occurring at the electrode within the desired potential window.

The LSV measurements here reported were always performed at RT using a VMP-3 Potentiostat/Galvanostat from BioLogic Science Instrument (France).



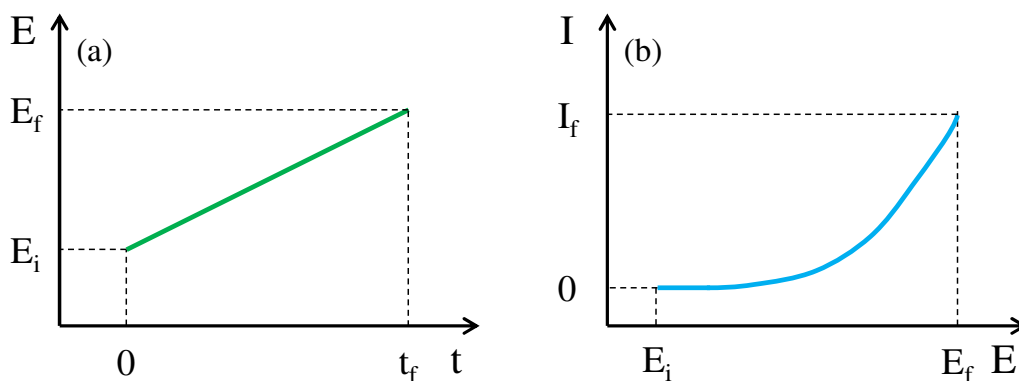


**Figure 18:** (a) Linear potential scan from an initial value ( $E_i$ ) to a final value ( $E_f$ ) and (b) measured current during the potential scan.

### 3.4.2.3 Electrochemical Impedance Spectroscopy

Electrochemical impedance spectroscopy is a very powerful electrochemical technique, which provides information about interfaces and the processes occurring at them.

Impedance spectroscopy measurements often consist in perturbing the investigated system with a single-frequency signal (voltage or current) and then measuring the phase shift and the amplitude of the response signal at that same frequency.<sup>99</sup> The system is normally investigated in a wide range of frequencies (from mHz to MHz) in order to study processes presenting different kinetics.

An impedance spectroscopy measure starts with the application a sinusoidal signal to the system. A Frequency Response Analyser controls the frequency of the applied signal (for example a voltage signal) according to the equation:

$$V(i) = V_a \sin(\omega t) \quad (3.3)$$

Where  $V_a$  is the amplitude of the perturbation,  $\omega$  is its angular frequency and  $t$  is the time. The applied signal induces a response signal from the system (in this case a current signal):

$$I(i) = I_a \sin(\omega t + \theta) \quad (3.4)$$

Where  $I_a$  is the amplitude of the response signal and  $\theta$  is its phase shift with respect to  $V(i)$ . Both  $I_a$  and  $\theta$  depend on the processes occurring in the investigated system. The Frequency Response Analyser processes the response signal, integrates it according to the Ohm's Law and originates this way the impedance signal ( $Z$ ).

It possible to represent  $Z$  as complex number in a vector diagram. According to this representation, the vector  $Z$  can be described in function of its real component ( $Z'$ ) and its imaginary component ( $Z''$ ):<sup>99</sup>

$$Z = Z' + iZ'' \quad (3.5)$$

Where  $i$  is the imaginary unit  $\sqrt{-1}$ . The real component  $Z'$ , the imaginary component  $Z''$  and the modulus  $|Z|$  of the impedance are accordingly defined as:

$$Z' = |Z| \cos \theta \quad (3.6)$$

$$Z'' = |Z| \sin \theta \quad (3.7)$$

$$|Z| = [(Z')^2 + (Z'')^2]^{1/2} \quad (3.8)$$

This representation of impedance is the so-called *Nyquist's plot* (**Figure 19**).

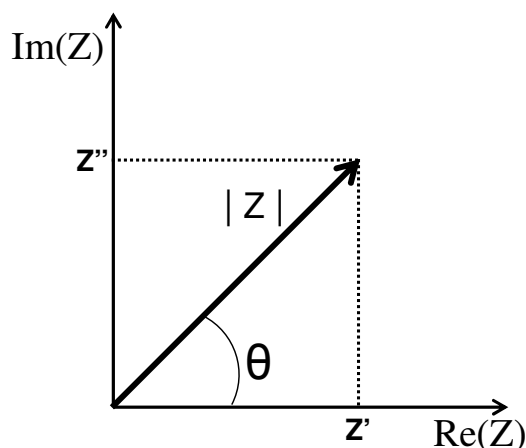


**Figure 19:** Nyquist's plot of impedance.

It is possible to fit the experimental impedance data with elements of ideal circuits. These elements give typical impedance responses (**Figure 20a, b, c**) and when conveniently combined in series or parallel, they can accurately fit complex experimental signals. In the case of electrode-electrolyte interfaces, the impedance signal can be fit according to the Randles circuit reported in **Figure 20d**.

The impedance measurements here reported were performed at RT with a VMP-3 Potentiostat/Galvanostat (BioLogic Science Instrument, France) equipped with a Frequency Response Analyser. The cells used for impedance spectroscopy measurements were two-electrodes coin cell or three-electrodes ECC-Ref (EL-Cells). The studied electrodes were always potentiostatically polarized for 1.5 h at the desired potential before performing the measurement. The impedance results were fitted with the program Equivalent Circuit according to the method of Boukamp.

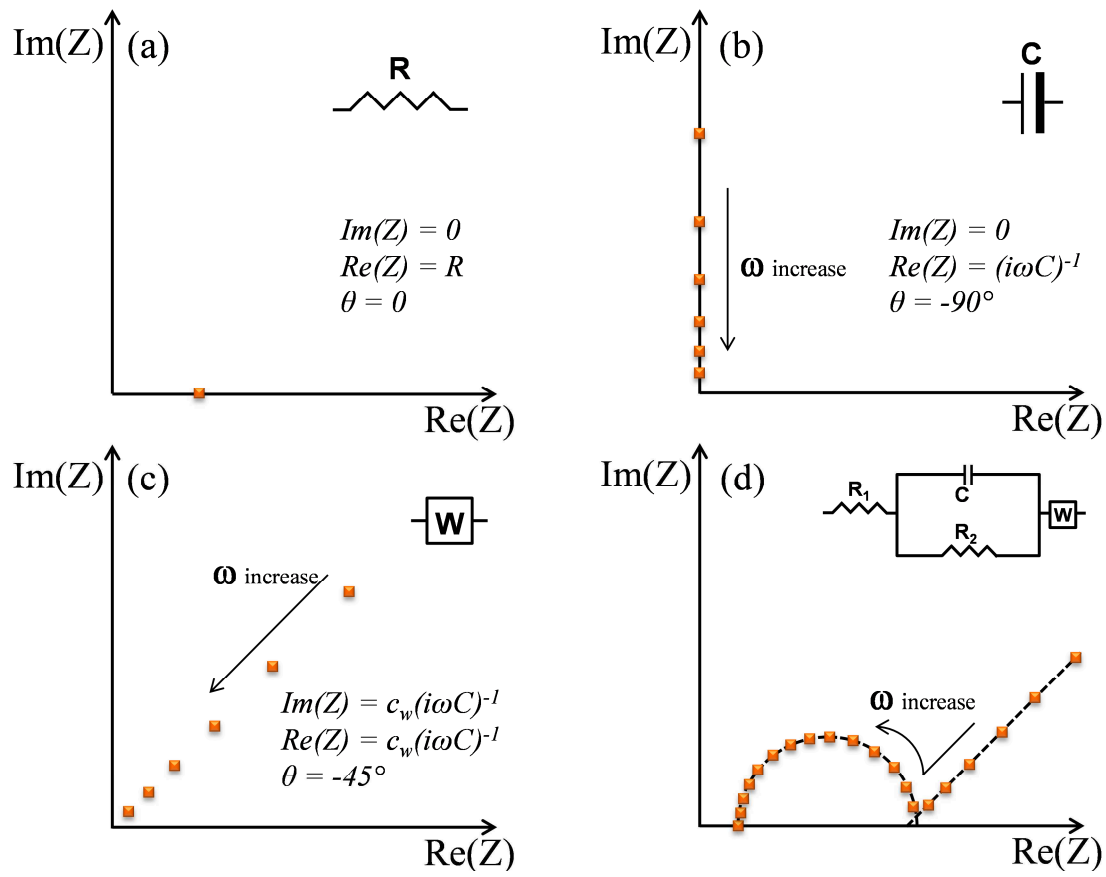


**Figure 20:** Nyquist's plots for (a) a resistor, (b) a capacitor, (c) a Warburg semi-infinite diffusion element and (d) a Randles circuit for electrode-electrolyte interfaces.

## 4. RESULTS AND DISCUSSION – Part I

### 4.1 Characterisation of the Pristine $\text{LiNi}_{0.5}\text{Mn}_{1.5}\text{O}_4$

#### 4.1.1 Morphology and composition of LMNO-0

The first material investigated in this work (LMNO-0) was obtained via the continuous co-precipitation method presented in *Chapter 3.1*. The aim of this synthesis was to realise high-performance  $\text{LiNi}_{0.5}\text{Mn}_{1.5}\text{O}_4$  presenting features in line with commercial cathode materials used in Li-ion batteries. For this purpose, the material was designed with specific particle architecture, consisting in spherical micrometric particles made of a large number of nano-sized crystallites in very close contact with each other (**Figure 21**).

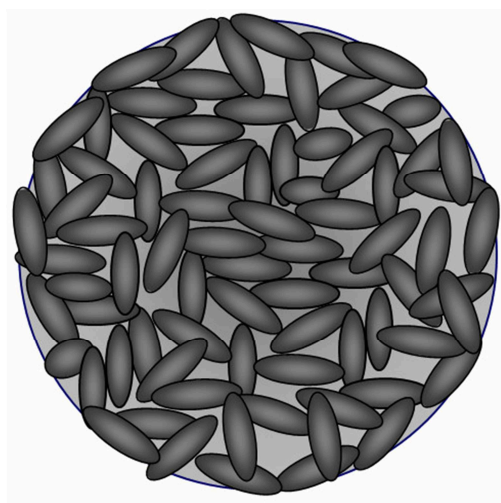


**Figure 21:** Representation of the desired LMNO particle architecture.

This specific architecture aims to minimize the particles' porosity and increase the density of the material. At the same time, the primary crystallites form a network of grain boundaries, which is expected to facilitate Li-ion and electron diffusion between the bulk and the surface of the particles.<sup>100,101</sup> Furthermore,

micrometric particles are easy to handle and present good processability during the electrode preparation process.

**Figure 22** displays the SEM pictures of the synthesized LMNO-0.<sup>102</sup>

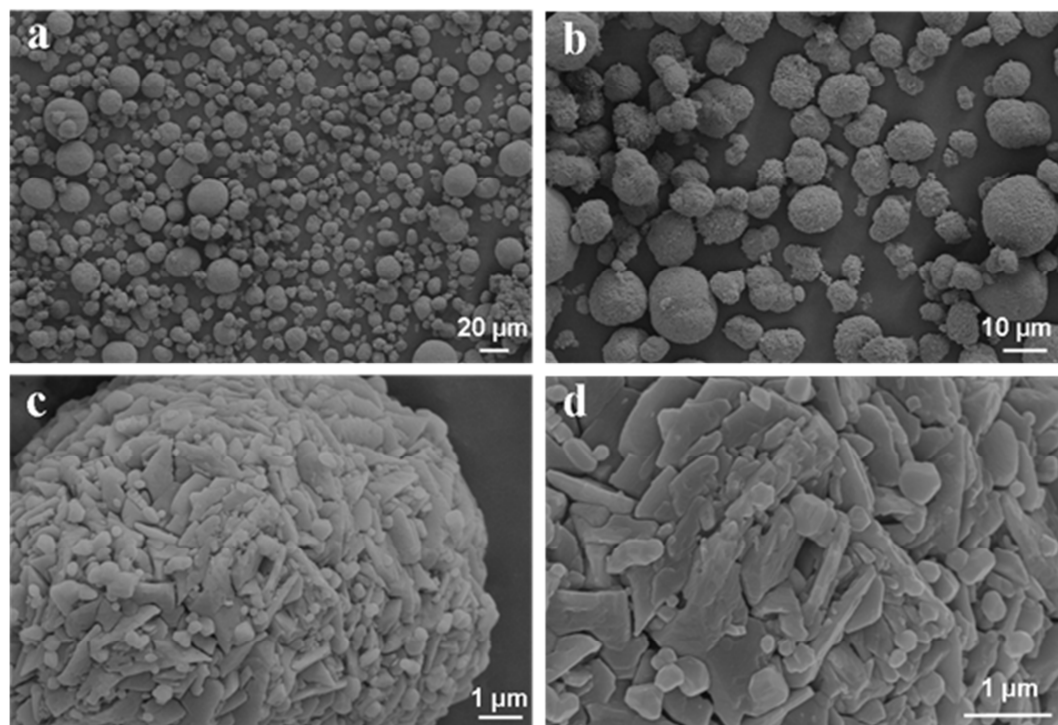


**Figure 22:** SEM images of the synthesized LMNO-0 at different magnifications. Reprinted from *J. Power Sources*, 301, (2016), 151-159. Copyright 2015, with permission from Elsevier.<sup>102</sup> Licence number 3875240261510.

The reported images show spherical particles with dimensions between few micrometres and few tens of micrometres. As discussed above, this specific particle architecture should guarantee dense materials with very low surface area. The density of LMNO-0 powders was determined by tap-density measurements and resulted  $2.26 \text{ g cm}^{-3}$ , which is a value suitable for Li-ion batteries application.<sup>93,94,95,96,97</sup> This high tap-density value is also due to the particle size distribution of LMNO-0. As shown in **Figure 23**, LMNO-0 presents particle dimensions between 3 and 50 μm, with  $d_{90} = 26 \text{ μm}$ ,  $d_{50} = 14.4 \text{ μm}$  and  $d_{10} = 7.6 \text{ μm}$ .

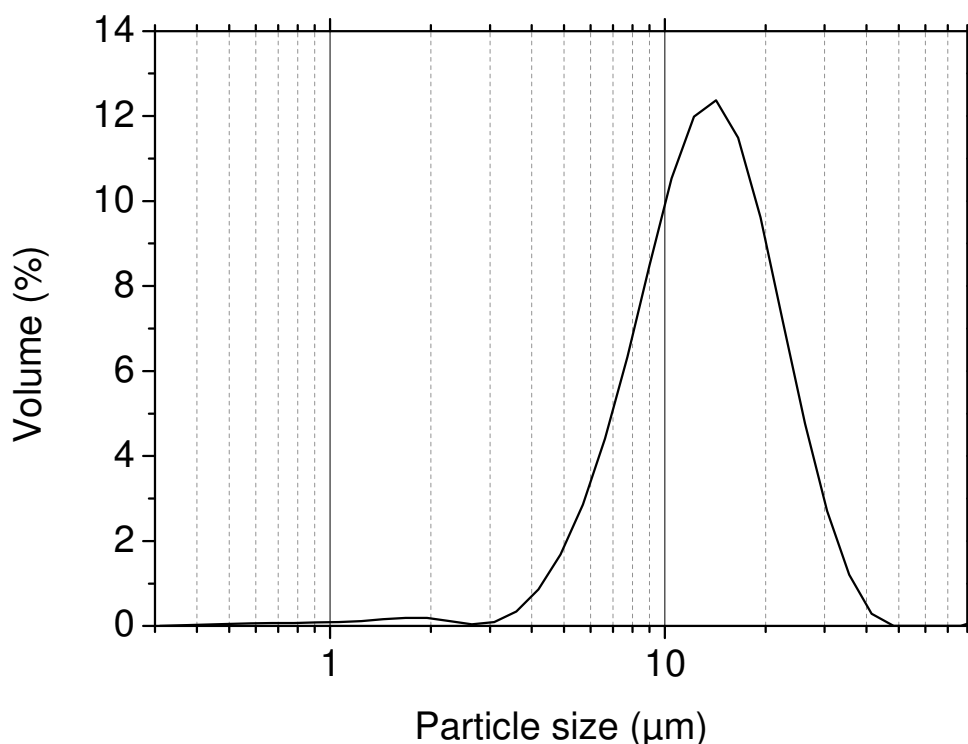


**Figure 23:** Particle size distribution of LMNO-0. Reproduced in part with permission from *J. Electrochem. Soc.*, 163, A470 (2016). Copyright 2016, The Electrochemical Society.<sup>103</sup>

This particle distribution allows smaller particles to fill the empty spaces between bigger particles obtaining a better packing of the powders. Furthermore, the micrometric size of the particles guarantees low surface area, which results below  $1 \text{ m}^2 \text{ g}^{-1}$  from BET analyses. The low surface area reduces the surface-reactivity of the active materials and guarantees higher stability for Li-ion battery applications.

An additional key aspect of this LMNO is the metal stoichiometry and the eventual presence of oxygen deficiencies. The fully substituted  $\text{LiNi}_{0.5}\text{Mn}_{1.5}\text{O}_4$  only presents high-voltage electrochemical activity (ca. 4.7 V vs.  $\text{Li/Li}^+$ ) and leads to higher specific energy in Li-ion cells. ICP analyses on LMNO-0 report a metal composition of 4.03 wt.% Li, 47.31 wt.% Mn and 16.86 wt.% Ni, which correspond to the Li : Mn : Ni ratio of 1.0 : 1.5 : 0.5.

Further XRD analyses on LMNO-0 powders confirmed its exact stoichiometry. As described in *Chapter 1.5*, stoichiometric  $\text{LiNi}_{0.5}\text{Mn}_{1.5}\text{O}_4$  presents a highly-

ordered structure described by the space group  $P4_332$ . According to this structure, the atoms occupy specific position in the lattice: 8c sites for Li, 4a sites for Ni, 12d sites for Mn, 8c and 24e sites for O. The highly-ordered lattice typical for fully-substituted LMNO gives rise to additional superstructure reflections in the XRD patterns at ca.  $15^\circ$ ,  $24^\circ$ ,  $35^\circ$ ,  $40^\circ$ ,  $46^\circ$ ,  $57^\circ$  and  $75^\circ$   $2\theta$  angles.<sup>53,54,55</sup> **Figure 24** displays an XRD pattern obtained for LMNO-0 powders and its fitting.

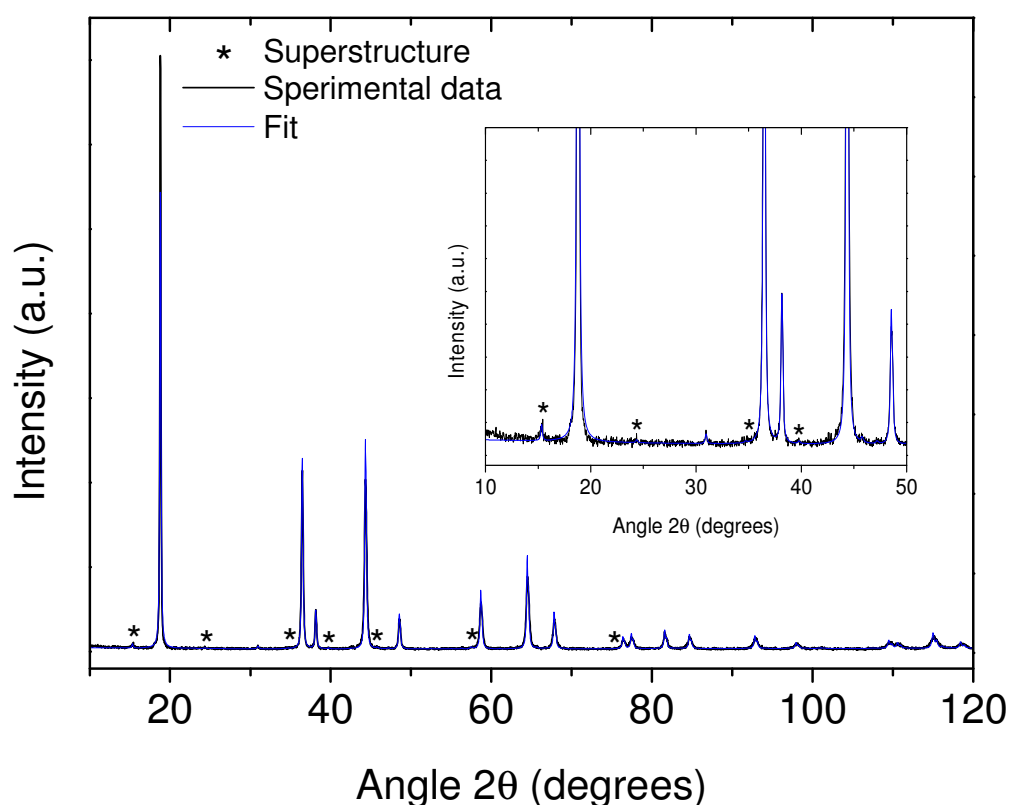


**Figure 24:** XRD pattern and fitting for LMNO-0 powders.

The pattern presents a phase-pure spinel structure with a clear superstructure reflection at  $15^\circ$ . The other superstructure reflections result more difficult to individuate because of their typical low intensities very close to the instrumental noise. Nevertheless, the XRD analyses confirm the structure typical for stoichiometric LMNO and the obtained data can be fit according to the  $P4_332$  space group. The fitting results report a lattice parameter  $a = 8.1694(6)$  Å (in



agreement with the data reported in literature) and mean crystallite size of 44(1) nm, which proves the presence of nano-sized primary crystallites in the particles.<sup>53,54,104,105</sup>

The analyses performed on LMNO-0 confirmed all the features desired for the pristine material. The sample presents tailored particle architecture, consisting in spherical particles made of a network of nano-sized crystallites in densely connected with each other. The particle architecture and the particle size distribution of LMNO-0 guarantee high tap-density beneficial for the processability and the loading of the electrodes. Furthermore, the sample is a fully substituted LMNO, beneficial for reducing the aging effects related to  $\text{Mn}^{3+}$ .<sup>56,59,60,61</sup>

### 4.1.2 Electrochemical Performance of LMNO-0

The next step for the characterisation of LMNO-0 consists in studying its electrochemical performance in standard organic electrolyte. The LMNO electrodes described in the entire chapter contained 90 wt.% of active material, 6 wt.% carbon black and 4 wt.% polyvinylidene fluoride. The active material loading was ca. 10 mg cm<sup>-2</sup>.

**Figure 25** shows the electrochemical performance of the LMNO-0 electrodes cycled between 3.5 – 4.9 V vs. Li/Li<sup>+</sup>.<sup>102</sup>

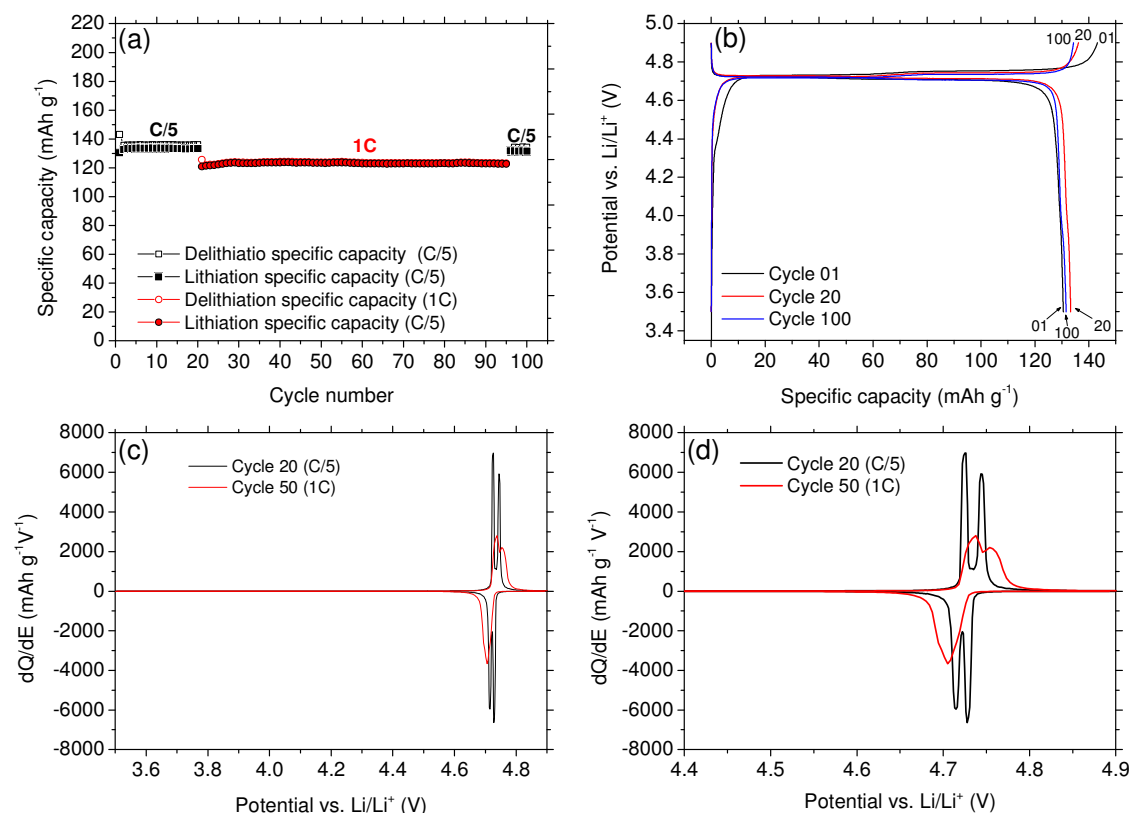


**Figure 25:** (a) Charge/Discharge cycles, (b) Potential vs. Specific capacity and (c), (d) corresponding differential curves for LMNO-0 electrodes. Adapted and reprinted from *J. Power Sources*, 301, (2016), 151-159. Copyright 2015, with permission from Elsevier.<sup>102</sup> Licence number 3875240261510.

These electrodes show stable discharge capacity of 133 and 123 mAh g<sup>-1</sup> at C/5 and 1C, respectively. This stable discharge capacity confirms the beneficial effects of the selected particle architecture on the cycling stability of LMNO-0

electrodes in standard organic electrolyte. The irreversible capacity (difference between charge capacity and discharge capacity) obtained at the first cycle is ca.  $13 \text{ mAh g}^{-1}$  (8 %). In the next cycles, it stabilizes at ca.  $3 \text{ mAh g}^{-1}$  (2 %) and  $0.4 \text{ mAh g}^{-1}$  (0.3 %) at C/5 and 1C, respectively. The irreversible capacity corresponds to the charge consumed by irreversible processes such as film formation and electrolyte decomposition. The irreversible capacity calculated at the first cycle suggests the formation of a passivation film on the surface of the electrode.<sup>66,67,69,70</sup> The significantly lower irreversible capacities determined in the next cycles are ascribable to ongoing electrolyte decomposition reactions, which are significantly reduced by the initial passivation of the electrode.

**Figure 25a** clearly shows the effects of the cycling rate on the electrochemical performance of LMNO-0 electrodes. Cycling at 1C leads to lower discharge capacity and lower irreversible capacity than cycling at C/5. The lithiation/delithiation kinetics of LMNO-0 will be discussed in *Chapter 4.2.2* and *Chapter 5*. However, the decrease of the irreversible capacity at 1C is probably due to shorter exposition of the electrolyte at the high operating potential of LMNO electrodes during each cycle.

**Figure 25b** displays the potential/specific capacity curves obtained from LMNO-0 electrodes. These curves present two very close high-voltage plateaus at ca. 4.7 V vs. Li/Li<sup>+</sup>, related to redox couple Ni<sup>2+</sup>/Ni<sup>4+</sup>. These two plateaus are easier to identify in the differential curves reported in **Figure 25c** and **Figure 25d**. In particular, the differential curve at C/5 (black line) shows two distinct peaks related to high-voltage plateaus at 4.72 and 4.74 V vs Li/Li<sup>+</sup> during charge and at 4.73 V and 4.71 V vs Li/Li<sup>+</sup> during discharge. Wang et al. associated these two high-voltage plateaus to the transition between three different cubic phases through the lithiation or delithiation process of LMNO.<sup>106</sup> **Figure 25b** do not show further electrochemical activity at 4 V vs. Li/Li<sup>+</sup>, confirming the absence of significant Mn<sup>3+</sup> traces in the sample.

According to the obtained results, LMNO-0 electrodes present high and stable discharge capacities, low irreversible capacities and no Mn<sup>3+</sup> activity at 4 V vs. Li/Li<sup>+</sup>. These results confirm the beneficial effects of the particle

architecture on the electrochemical performance of LMNO-0 in standard organic electrolyte. Additionally, the stoichiometric composition of LMNO-0 leads to only high-voltage electrochemical activity, which is beneficial for the specific energy achievable in full Li-ion cells.

## 4.2 Modification of the Pristine Material

### 4.2.1 Crystallite Size Effects

LMNO-0 electrodes showed remarkable electrochemical performances and confirm the importance of tailoring the particle architecture of active materials. Nevertheless, it is possible to adjust different basic features of the pristine material in order to further modify its electrochemical behaviour. Accordingly, basic features of LMNO-0 like crystallite size, oxygen stoichiometry and particle dimension were singularly modified and investigated keeping unchanged all the other characteristics. The aim of this study was to find out the most suitable material Li-ion cells application.

The crystallite size of LMNO-0 was modified by the secondary thermal treatment described in *Chapter 3.1.1*. This treatment aimed to increase the crystallites dimension of LMNO-0, without modifying the final oxygen stoichiometry.

**Figure 26** shows the SEM images of the material after the thermal treatment (LMNO-T1).

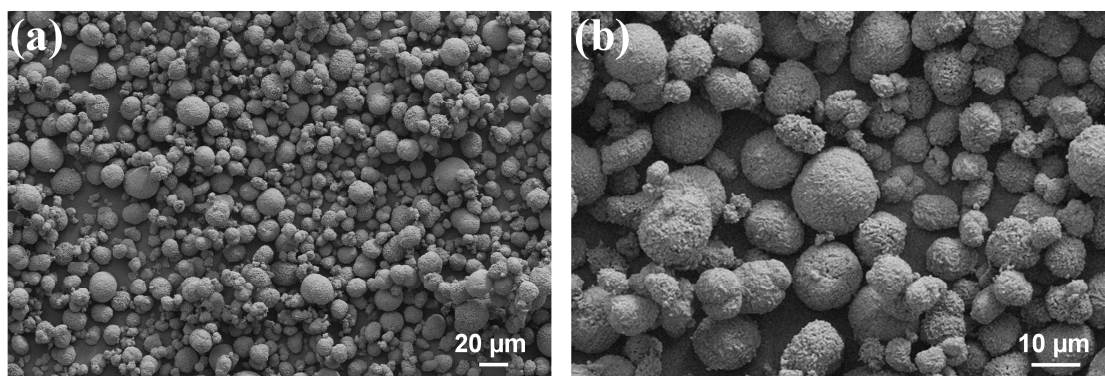


**Figure 26:** SEM images of the sample LMNO-T1. Reprinted in part from *J. Power Sources*, 301, (2016), 151-159. Copyright 2015, with permission from Elsevier.<sup>102</sup> Licence number 3875240261510.

The images confirm that no changes occurred to the particle architecture and morphological features of the pristine material. Also the metal composition

determined by ICP analyses did not change after the secondary thermal treatment and the sample still presented the Li : Ni : Mn ratio of 1.0 : 0.5 : 1.5.

The structure of LMNO-T1 was investigated by XRD analyses in order to confirm the absence of oxygen deficiencies and determine eventual impurities formed during the thermal treatment. **Figure 27** reports a diffractogram and the relative fitting obtained from LMNO-T1 powders.

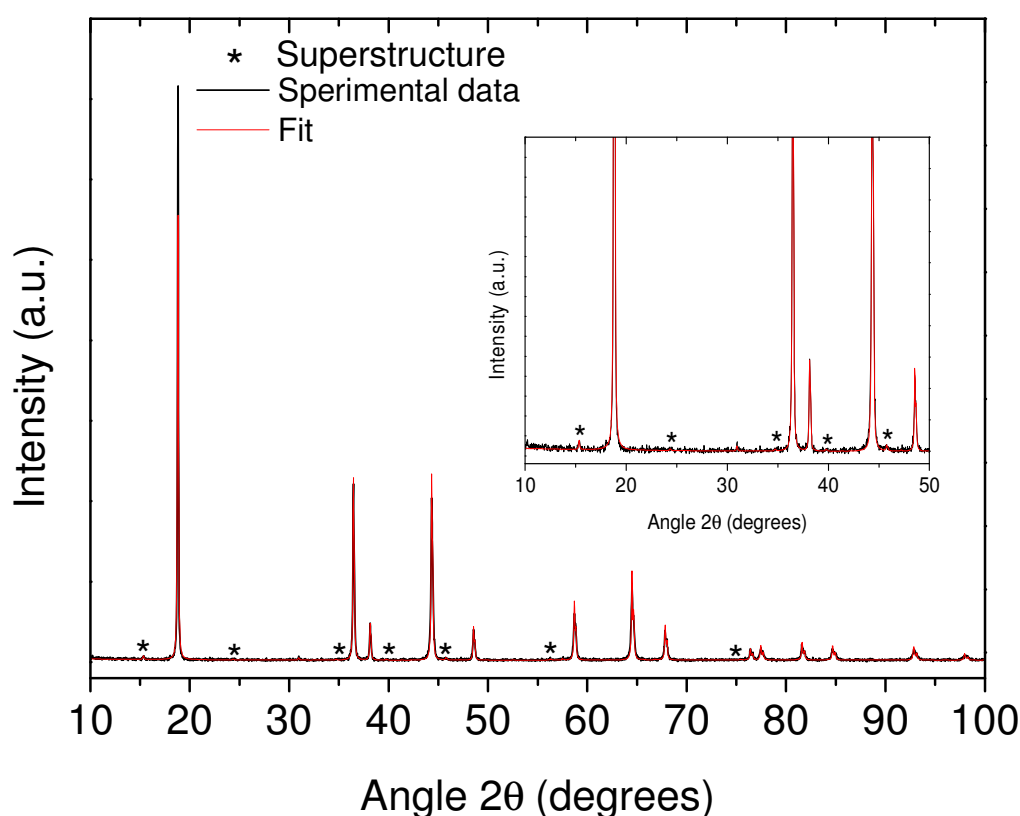


**Figure 27:** XRD pattern and fit for the sample LMNO-T1.

LMNO-T1 shows again the superstructure peak at ca. 15°. Accordingly, the fitting of the experimental data was performed according to the space group  $P4_332$ . The obtained cell parameter ( $a$ ) results 8.1680(5) Å, which is once again in agreement with what expected for highly ordered LMNO.<sup>53,54,104,105</sup> As expected, the crystallite size of LMNO-T1 increased to 83(2) nm. According to the collected data, this material results suitable to evaluate the role of the

crystallite size on the electrochemical performance of LMNO keeping unchanged all the other pristine features.

Both LMNO-0 and LMNO-T1 electrodes were tested between 3.5 – 4.9 V vs Li/Li<sup>+</sup> at different C-rates. **Figure 28** displays the potential/specific capacity profiles obtained from these cells.

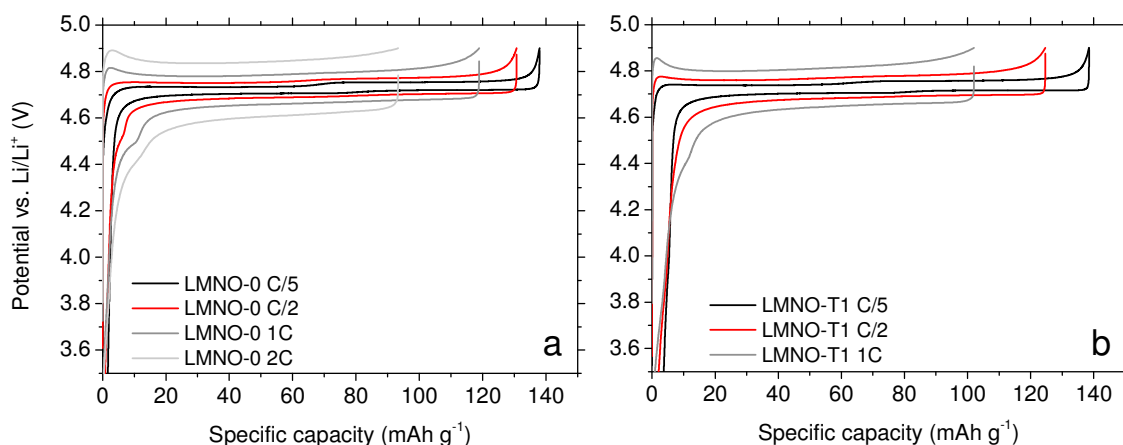


**Figure 28:** Potential vs. Specific capacity profiles obtained for (a) LMNO-0 and (b) LMNO-T1. Reprinted in part from *J. Power Sources*, 301, (2016), 151-159. Copyright 2015, with permission from Elsevier.<sup>102</sup> Licence number 3875240261510.

The electrodes exhibit the potential plateaus related to the redox couple Ni(II)/Ni(IV) and typical for stoichiometric LMNO. The potential profiles of these electrodes also show hysteresis between the charge and the discharge plateaus, related to the IR drop and to the lithiation/delithiation kinetics. The IR drop depends on the applied current and thus, higher C-rates leads to the enlarging of the hysteresis and to the approaching of the charging plateaus to the upper cut-off potential (4.9 V vs. Li/Li<sup>+</sup>). This behaviour leads to a premature interruption of the charge and explains the lower discharge capacities obtained for LMNO-0 and LMNO-T1 electrodes at higher C-rates.

As shown in **Figure 29**, cycling LMNO-0 and LMNO-T1 electrodes at C/5 leads to comparable discharge capacity (ca. 135 mAh g<sup>-1</sup>) and potential hysteresis (ca. 50 mV). This is not anymore valid at higher C-rates, where LMNO-T1 electrodes present larger hysteresis and lower discharge capacities than LMNO-0 electrodes (samples LMNO-T2 and LMNO-T3 will be discussed in the next

paragraph). This different electrochemical behaviour at higher C-rates suggests slower delithiation/lithiation kinetics in the case of bigger crystallites, which lead to longer diffusion paths for the Li-ions inside the material.

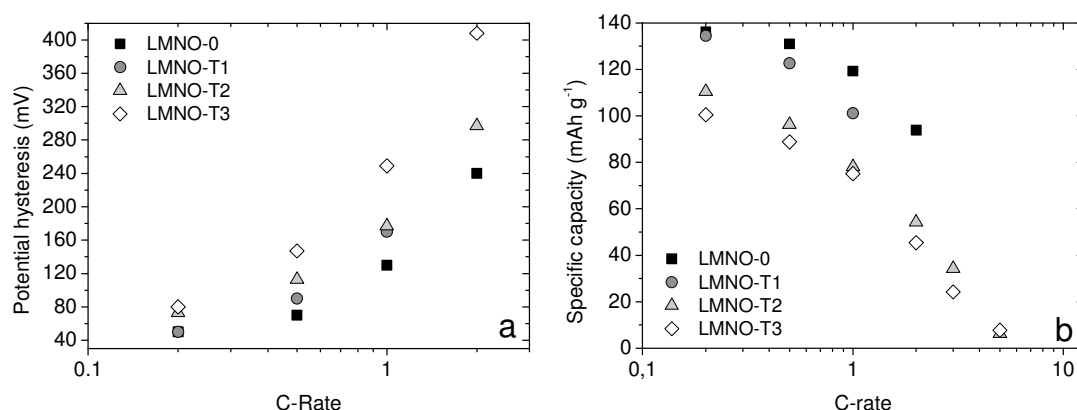


**Figure 29:** (a) Trend of the hysteresis and (b) of the discharge specific capacity in function of the applied C-rate for LMNO-0 and LMNO-T1, LMNO-T2 and LMNO-T3 electrodes. Reprinted in part from *J. Power Sources*, 301, (2016), 151-159. Copyright 2015, with permission from Elsevier.<sup>102</sup> Licence number 3875240261510.

LMNO-0 and LMNO-T1 electrodes show sudden capacity drop down at 3C and 2C, respectively. This phenomenon is probably due to the potential peak appearing at the beginning of the charging process at higher C-rates (**Figure 28**). When this potential peak reaches the upper cut-off potential, the charging process suddenly stops without any significant delithiation of the electrodes. This potential peak is characteristic for stoichiometric LMNO and will be further discussed in *Chapter 4.2.2* along with the electrochemical behaviour of not stoichiometric LMNO.

The investigation of the crystallite size pointed out slower kinetics for bigger crystallites and no improvements on the electrochemical performances. Thus, smaller primary crystallites are the best choice to obtain better rate capabilities.



### 4.2.2 Changes in the Oxygen Stoichiometry of LMNO

Performing secondary thermal treatment, allows introducing different amounts of oxygen deficiencies in the LMNO structure. The oxygen deficiencies modify the stoichiometry of the material and the oxidation state of the manganese according to the formula  $\text{Li}[\text{Ni(II)}_{0.5}\text{Mn(III)}_{2\delta}\text{Mn(IV)}_{1.5-2\delta}]\text{O}_{4-\delta}$ .

In order to investigate the role of these oxygen deficiencies on the electrochemical behaviour of LMNO-0, two secondary thermal treatments were performed on the pristine material as described in *Chapter 3.1.1*. The obtained materials are expected to contain low amounts (LMNO-T2) and high amounts (LMNO-T3) of oxygen deficiencies, keeping unchanged the other fundamental features of the pristine LMNO-0.

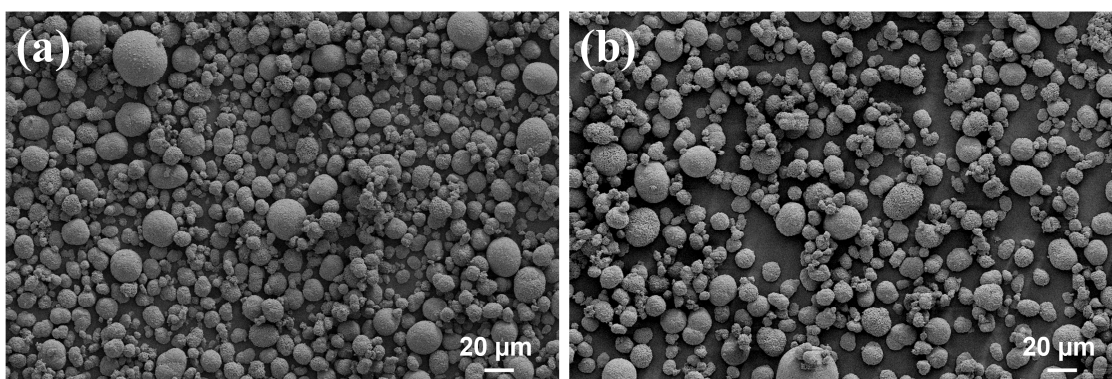


**Figure 30:** SEM images of (a) LMNO-T2 and (b) LMNO-T3. Reprinted in part from *J. Power Sources*, 301, (2016), 151-159. Copyright 2015, with permission from Elsevier.  
<sup>102</sup> Licence number 3875240261510.

The SEM images of LMNO-T2 and LMNO-T3 powders show the same particle architecture observed in the pristine LMNO-0. Also ICP analyses did not report any variation of the pristine Li : Ni : Mn (1.0 : 0.5 : 1.5).

**Figure 31** compares the XRD patterns and relative fittings of LMNO-0, LMNO-T1, LMNO-T2 and LMNO-T3.

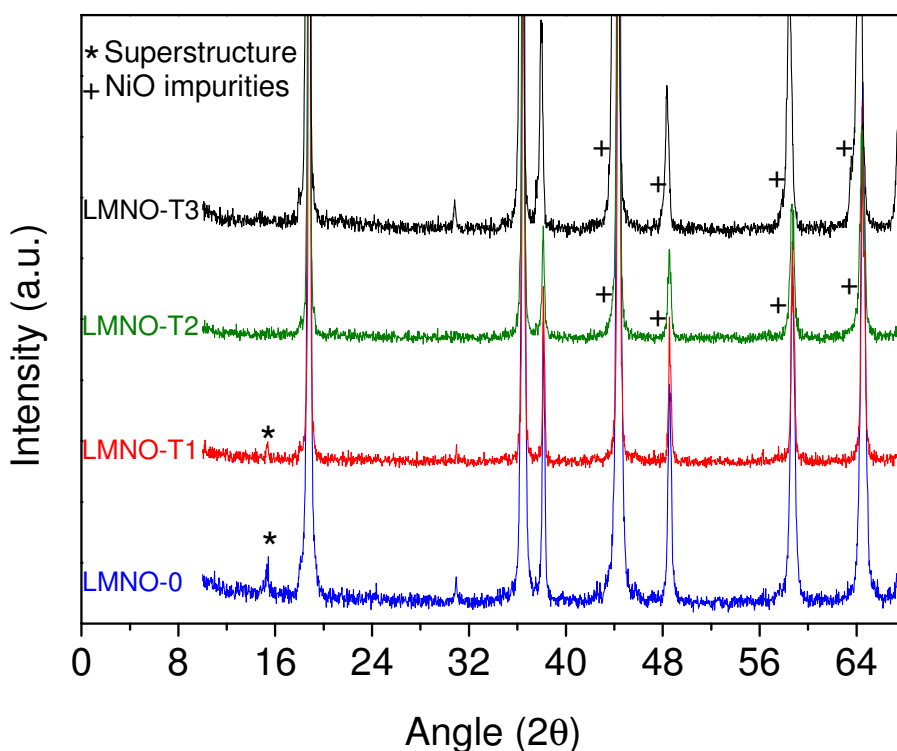


**Figure 31:** XRD patterns and fits for LMNO-0, LMNO-T1, LMNO-T2 and LMNO-T3. Reprinted from *J. Power Sources*, 301, (2016), 151-159. Copyright 2015, with permission from Elsevier.<sup>102</sup> Licence number 3875240261510.

The oxygen-deficient materials do not present any superstructure reflections typical for highly ordered spinel structure. Thus, the diffraction patterns of LMNO-T2 and LMNO-T3 were fitted according to the  $Fd\bar{3}m$  space group, where Li atoms occupy the 8a positions, Mn and Ni atoms occupy the 16d positions, and O atoms occupy the 32e positions.<sup>53,54,55</sup> Furthermore, the oxygen-deficient materials show asymmetric broadening of some peaks at lower angles (marked with “+” in **Figure 31**). The broadening of these peaks indicates that LMNO-T2 and LMNO-T3 contain electrochemically inactive Rock-salt impurities, which are typical for not-stoichiometric materials prepared by thermal treatments.<sup>45,64,107</sup> LMNO-T3 presents larger peak broadening than LMNO-T2, suggesting a correlation between the quantity of impurities and the amount of oxygen deficiencies. **Table 1** resumes the results of the XRD fittings performed on LMNO-0, LMNO-T2 and LMNO-T3 diffraction patterns.

**Table 1:** XRD fits results for LMNO-0, LMNO-T2 and LMNO-T3.

	Space Group	Crystallite Size (nm)	Latt. Parameter (Å)	Phases
<b>LMNO-0</b>	$P4_332$	44(1)	8.1694(4)	Ordered spinel
<b>LMNO-T2</b>	$Fd3-m$	55(1)	8.1732(8)	Disordered spinel Rock-salt imp.
<b>LMNO-T3</b>	$Fd3-m$	63(1)	8.2022(7)	Disordered spinel Rock-salt imp.

The fittings of the XRD patterns report increases of lattice parameter proportional to the amount of oxygen deficiencies. This result is in agreement with the literature and confirms that part of  $Mn^{4+}$  converted in  $Mn^{3+}$ .<sup>53,64,106,108</sup> Unfortunately, applying secondary thermal treatments is not possible to completely exclude the crystallite growth.

In order to evaluate the electrochemical behaviour of oxygen-deficient materials, electrodes made of LMNO-T2 and LMNO-T3 were cycled at different C-rates and compared with LMNO-0 electrodes. **Figure 32** compares the potential profiles and the discharge capacities obtained from these electrodes. The potential profiles of LMNO-T2 and LMNO-T3 electrodes appear immediately different from those of LMNO-0 electrodes. The most evident difference is the electrochemical activity of  $Mn^{3+}$  at ca. 4 V vs. Li/Li<sup>+</sup>. LMNO-T3 electrodes show the longest low-potential plateau and the shortest high-potential plateaus among all the tested materials. This behaviour depends on the high amounts of  $Mn^{4+}$  converted in  $Mn^{3+}$  during the secondary thermal treatment and leads to a conversion of the high-voltage capacity in low voltage capacity. The higher is the amount of oxygen deficiencies in the material, the stronger is the low-voltage contribution.

Also increasing the C-rate reduces the length of the high-voltage plateaus but it does not influence the length of the low-voltage plateau. The reason of this high-voltage capacity loss was already discussed in *Chapter 4.2.1* and regards the earlier reaching of the upper potential cut-off during delithiation.

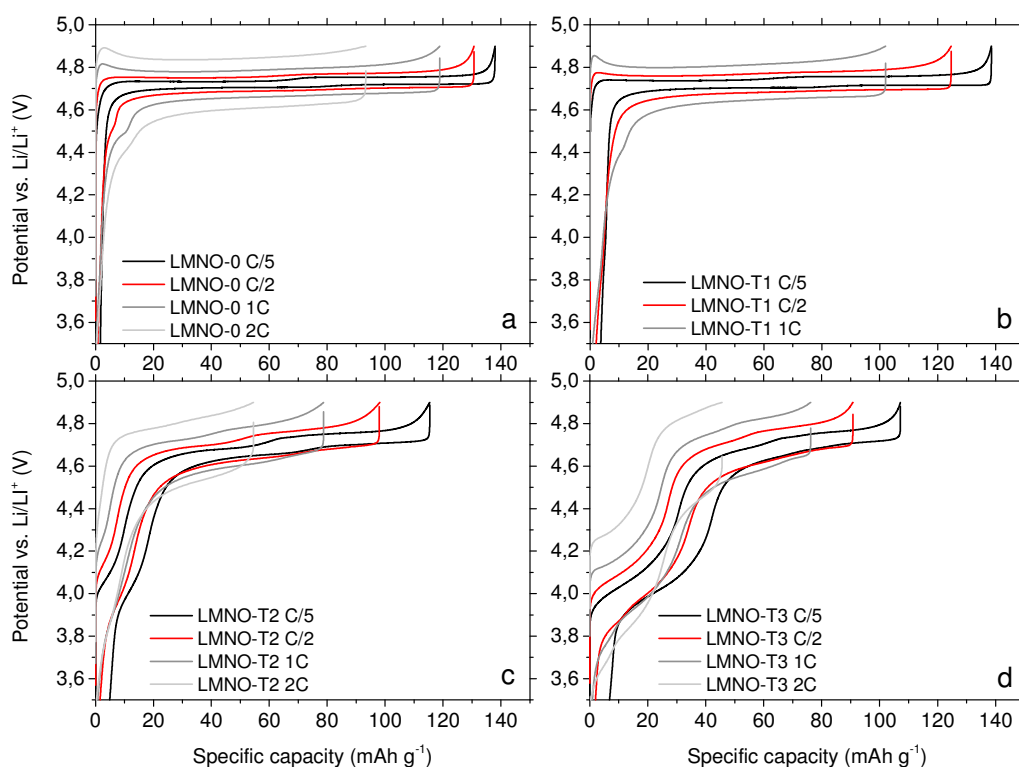


**Figure 32:** Potential vs. specific capacity profiles for (a) LMNO-0, (b) LMNO-T1, (c) LMNO-T2 and (d) LMNO-T3 electrodes. Reprinted in part from *J. Power Sources*, 301, (2016), 151-159. Copyright 2015, with permission from Elsevier.<sup>102</sup> Licence number 3875240261510.

Oxygen-deficient materials always show lower discharge capacities than LMNO-0, probably because of the electrochemically inactive phases formed during the secondary thermal treatments. The rate capabilities of LMNO-0, LMNO-T2 and LMNO-T3 electrodes are similar up to 2C but then, LMNO-0 electrodes show the sudden capacity drop-down described in the previous chapter (**Figure 29b**). According to the literature, not stoichiometric LMNO phases show better ionic and electronic conductivity with respect to the stoichiometric one.<sup>62,63</sup> However, the rate capability of stoichiometric and not stoichiometric materials are comparable up to 2C. Furthermore, the capacity drop-down observed for LMNO-0 electrodes is more likely ascribable to the steep potential increase at the beginning of the delithiation process of stoichiometric materials (**Figure 28 Chapter 4.2.1** and **Figure 32**). **Figure 33a** clearly shows that the potential maximum value ( $U_{\max}$ ) for LMNO-0 electrodes is very close the upper cut-off of 4.9 V vs. Li/Li<sup>+</sup> already at 2C. Extrapolating  $U_{\max}$  and  $U_{\text{plat}}$  at 3C (**Figure 33b**),

the calculated  $U_{\max}$  value is higher than the cell cut-off potential and it is probably the reason of the sudden charge interruption. On the contrary, the calculated plateau potential ( $U_{\text{plat}}$ ) at 3C is still lower than the cut-off potential suggesting that it would be still possible to charge LMNO-0 electrodes at this C-rate.

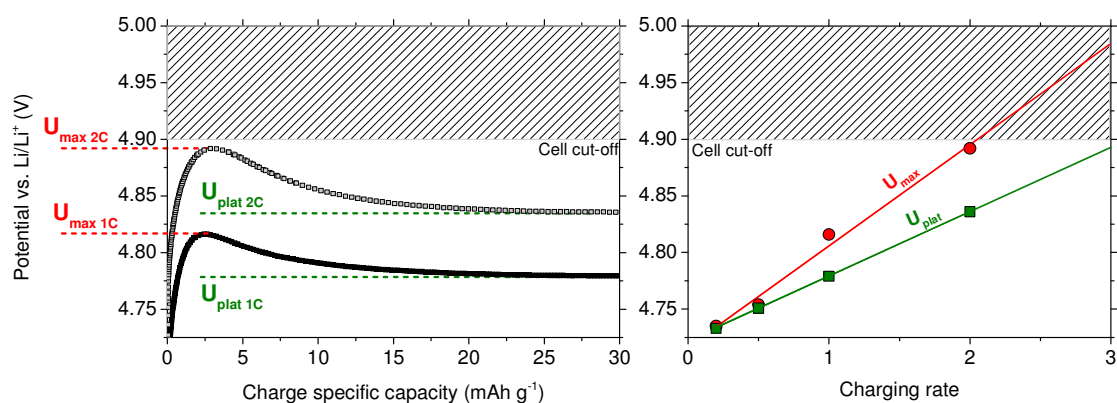


**Figure 33:** (a)  $U_{\text{plat}}$  and  $U_{\max}$  at 1C and 2C for LMNO-0 electrodes. (b) Increase of  $U_{\text{plat}}$  and  $U_{\max}$  with the C-rate and extrapolation at 3C for LMNO-0 electrodes.

In order to better understand the origin of this initial potential maximum in stoichiometric materials, impedance measurements were performed at 3.5 V vs. Li/Li<sup>+</sup> (lithiated status) and at 4.9 V vs. Li/Li<sup>+</sup> (delithiated status) on both LMNO-0 and LMNO-T3 electrodes. **Figure 34** reports and compares the results of these impedance measurements. The semicircles observed at high to medium frequencies for LMNO-0 are larger in the lithiated status (discharged) than in the delithiated status (charged). The larger semicircles related to the discharged electrode suggest higher resistances for the lithiated phase than for the delithiated phase. This difference in the resistance between lithiated and delithiated phase can explain the rapid increase of potential at the beginning of the charging process ( $U_{\max}$ ) and the consecutive reduction to the plateau value ( $U_{\text{plat}}$ ) as the material undergoes the delithiation process. Oxygen-deficient materials present similar semicircle size both in the lithiated and in the delithiated phase. Thus, they neither present  $U_{\max}$  values nor incur into the sudden capacity fade observed for stoichiometric materials. However, the semicircles obtained from charged

electrodes are smaller for LMNO-0 than for LMNO-T3, suggesting lower resistances and better kinetics for the delithiated phase of the stoichiometric material. This hypothesis is supported also by the hysteresis observed for oxygen-deficient materials (**Figure 32**), which are larger than those observed for the stoichiometric material.

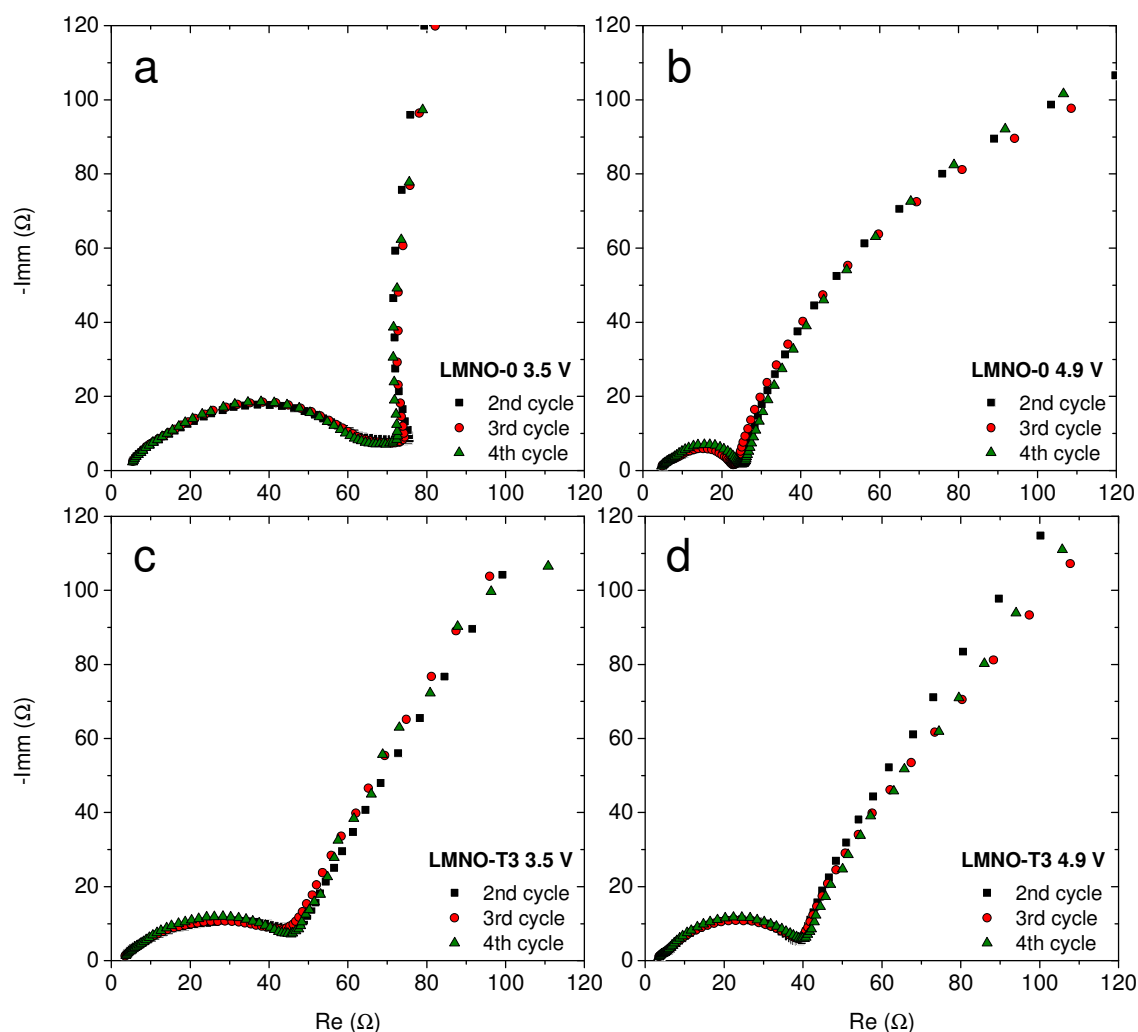


**Figure 34:** Impedance spectra for LMNO-0 and LMNO-T3 electrodes in (a), (b) lithiated status and (c), (d) delithiated status. Reprinted from *J. Power Sources*, 301, (2016), 151-159. Copyright 2015, with permission from Elsevier.<sup>102</sup> Licence number 3875240261510.

According to the obtained results, the stoichiometric LMNO-0 presents different positive features with respect to the two oxygen-deficient materials. LMNO-0 is a single phase material, without any impurities formed during the primary

thermal treatment. This guarantees higher discharge capacity for LMNO-0 electrodes than for LMNO-T2 and LMNO-T3 electrodes. Furthermore, the stoichiometric material presents only high-voltage activity, which is beneficial for increasing the specific energy of Li-ion cells. Finally, LMNO-0 electrodes show rate capabilities comparable with LMNO-T2 and LMNO-T3 electrodes up to 2C and faster kinetics in the charged status. The only problem of LMNO-0 electrodes is the initial potential peak, which requires the study of suitable charging procedures (see *Chapter 5.2*).

### 4.2.3 Role of the particle dimension in LMNO-0 electrodes

The synthesis process described in *Chapter 3.1.1* allows obtaining different LMNO batches with tuned particle size. Nevertheless, it is better to use the same LMNO-0 batch for the complete investigation of the pristine material. For this reason, the effect of the particle dimension on the electrochemical performance of LMNO was evaluated by sieving the pristine material in different batches. The sieving process allowed dividing LMNO-0 in four different batches according to the particle size:  $< 20\ \mu\text{m}$  (LMNO-XS),  $20 - 25\ \mu\text{m}$  (LMNO-S),  $25 - 32\ \mu\text{m}$  (LMNO-M) and  $32 - 40\ \mu\text{m}$  (LMNO-L).

**Figure 35** shows SEM images of the different sieved samples.

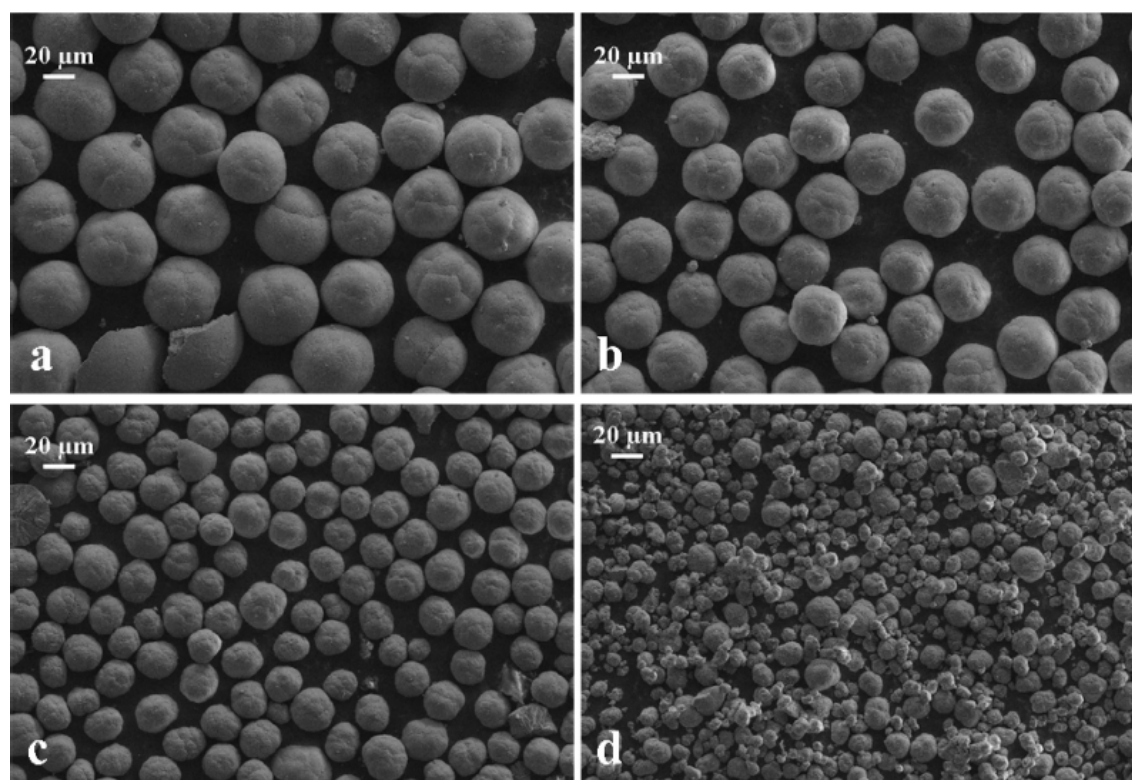


**Figure 35:** SEM images for (a) LMNO-L, (b) LMNO-M, (c) LMNO-S and (d) LMNO-XS. Reprinted from *J. Power Sources*, 301, (2016), 151-159. Copyright 2015, with permission from Elsevier.<sup>102</sup> Licence number 3875240261510.

The SEM images clearly show comparable particle dimensions for all the sieved samples, with the exception of few very small particles visible in all the fractions.



These smaller particles did not pass through the meshes during the sieving process. However, their amount is considerably small and not enough to significantly influence the electrochemistry of the main fraction.

**Figure 36** summarises the electrochemical results obtained with the four different sieved materials. Because of the charge interruption observed for LMNO-0 at high C-rates, the electrodes were always charged at C/2 and then discharged at different C-rates.

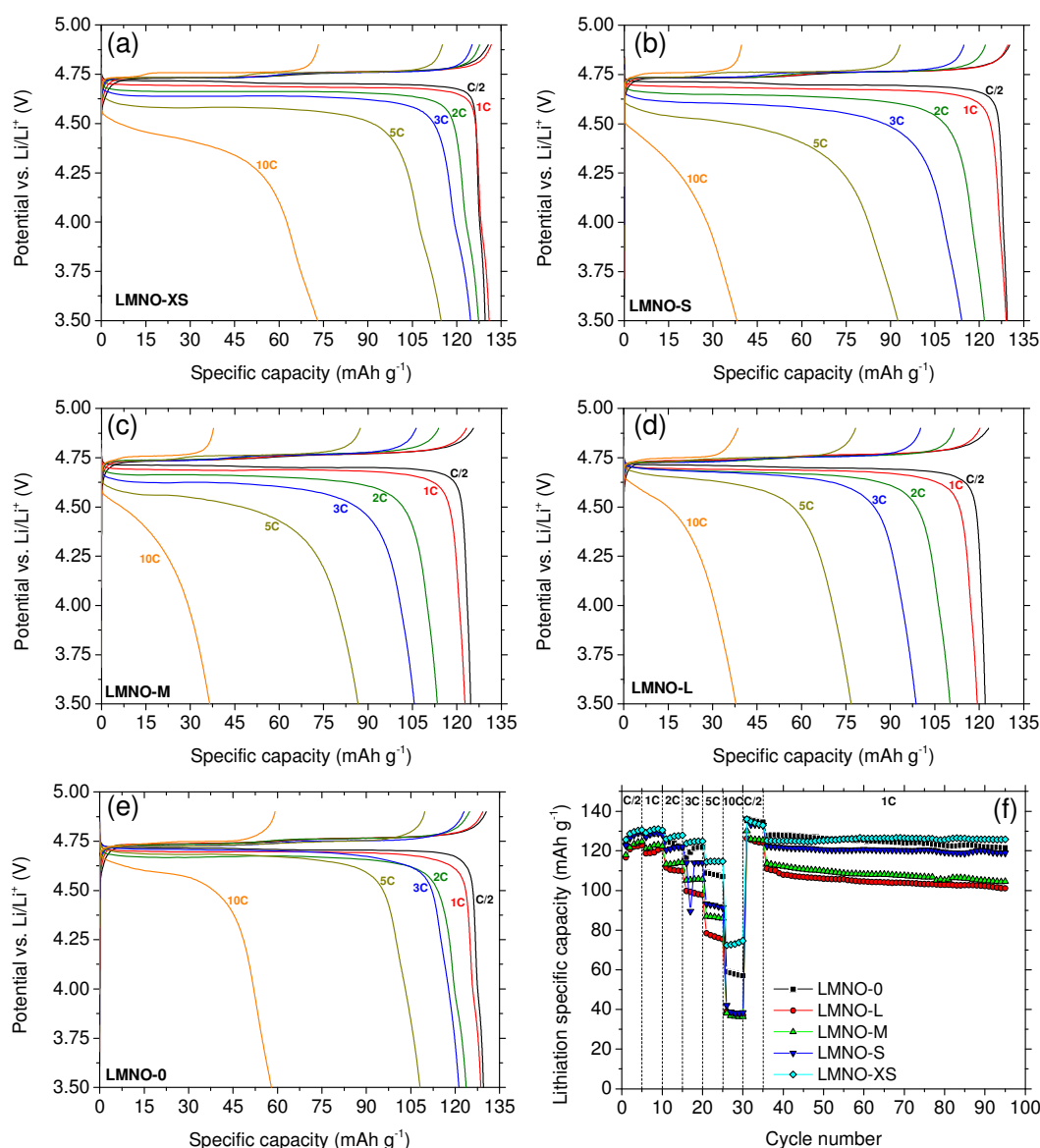


**Figure 36:** Potential vs. Specific capacity profiles for (a) LMNO-XS, (b) LMNO-S, (c) LMNO-M (d) LMNO-L and (f) reversible specific capacity for the same electrodes. Reprinted in part from *J. Power Sources*, 301, (2016), 151-159. Copyright 2015, with permission from Elsevier.<sup>102</sup> Licence number 3875240261510.

The reported potential profiles and specific discharge capacities show the significant effect of the particle dimension on the electrochemical performances of the different electrodes. By increasing the particle dimension, the electrodes present lower rate capability related to slower intercalation kinetics. The reason for this behaviour is probably the longer Li-ion diffusion path between the surface and the bulk of bigger particles. It is also worth to notice that LMNO-0 electrodes show the best rate capability after LMNO-XS electrodes. Additionally, the difference between the charge and the discharge potentials for LMNO-0 electrodes is smaller than for LMNO-XS electrodes. This result is more likely ascribable to inter-particle effects than to particle size effects. As discussed in *Chapter 4.1*, the wide particle size distribution of LMNO-0 allows smaller particle to fill the empty spaces between bigger particles. Thus, it is probable that the close packing obtained with a wider particle size distribution increases the amount of inter-particle contacts available for the migrating electrons.

According to the obtained results, adopting LMNO-XS as cathode material leads to the best rate capability among all the tested batches. This improved rate capability is probably due to the shorter Li-ion diffusion path between the surface and the bulk of the particle. However, also LMNO-0 electrodes show remarkable rate capability and lower potential hystereses between charge and discharge potentials. Furthermore, bigger particle size leads to reduction of the surface area, which is beneficial for reducing the surface-reactivity of the material.

Summarising all the results presented in *Chapter 4*, the pristine LMNO-0 seems to be the best candidate in terms of electrochemical performance. Thus, it is the material of choice for electrolyte stability studies.

## 5. RESULTS AND DISCUSSION – Part II

### 5.1 STUDY OF THE ELECTROLYTE STABILITY ON LMNO-0 ELECTRODES.

As described in *Chapter 1.5*, cycling high-voltage cathode materials leads to a large variety of electrolyte decomposition reactions. The electrolyte decomposition by-products are the main reason for the deterioration of all the cell components. Thus, realising stable high-voltage cells requires materials with low electrolyte degradation rates.

The rate of the electrolyte decomposition processes and the performances of the electrodes are firstly affected by the morphology of the cathode material. Many works in literature support the adoption of tailored nanometric sized materials in order to obtain better kinetics and improve the electrochemical performance.<sup>48,49,50,109,110,111</sup> Unfortunately, these nanometric sized materials have lower processability than micrometric sized materials. Furthermore, their high surface area leads to lower cycling stability in standard electrolytes.<sup>112,113,114</sup> The particle architecture of LMNO-0 was designed to reach a good compromise between high electrochemical performance and low electrolyte decomposition. According to this architecture, the micrometric particles guarantee low surface area available for electrolyte decomposition. At the same time, the network of nanometric crystallites provides good kinetics and electrochemical performance. In order to verify the effects of the particle architecture, the electrolyte decomposition rates for LMNO-0 and LMNO-R electrodes were studied and compared.

**Figure 37** compares SEM images of LMNO-0 and LMNO-R powders.

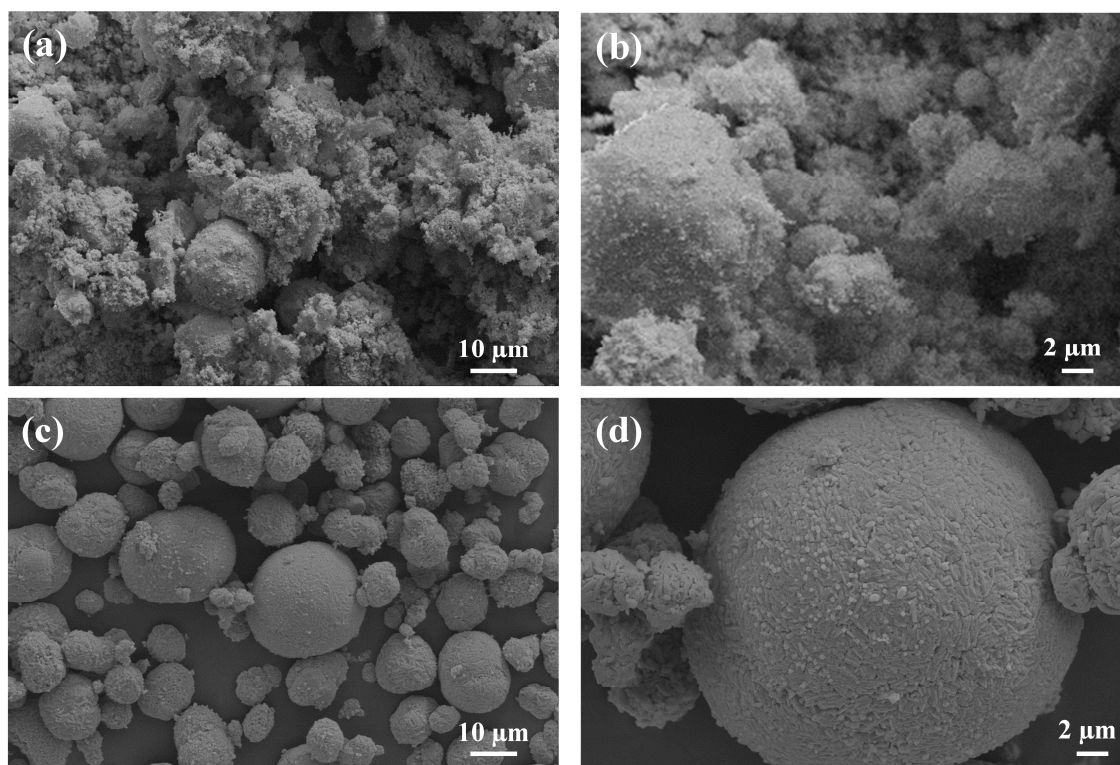


**Figure 37:** SEM images for (a), (b) LMNO-R and (c), (d) LMNO-0 samples.

The reference material LMNO-R does not have any specific particle architecture and consists in a dispersion of micrometric particles together with sub-micrometric particles and aggregates. According to these images, LMNO-R seems to present smaller particles and broader particle size distribution than LMNO-0. The light scatter analyses reported in **Figure 38** confirms what observed in the SEM images and reports a size distribution of  $d_{90} = 34.1 \mu\text{m}$ ,  $d_{50} = 8.8 \mu\text{m}$ ,  $d_{10} = 0.5 \mu\text{m}$ . The smaller particles and the absence of a dense morphology in LMNO-R lead to higher surface area ( $18 \text{ m}^2 \text{ g}^{-1}$ ) and lower tap-density ( $0.67 \text{ g cm}^{-3}$ ) in comparison to LMNO-0.

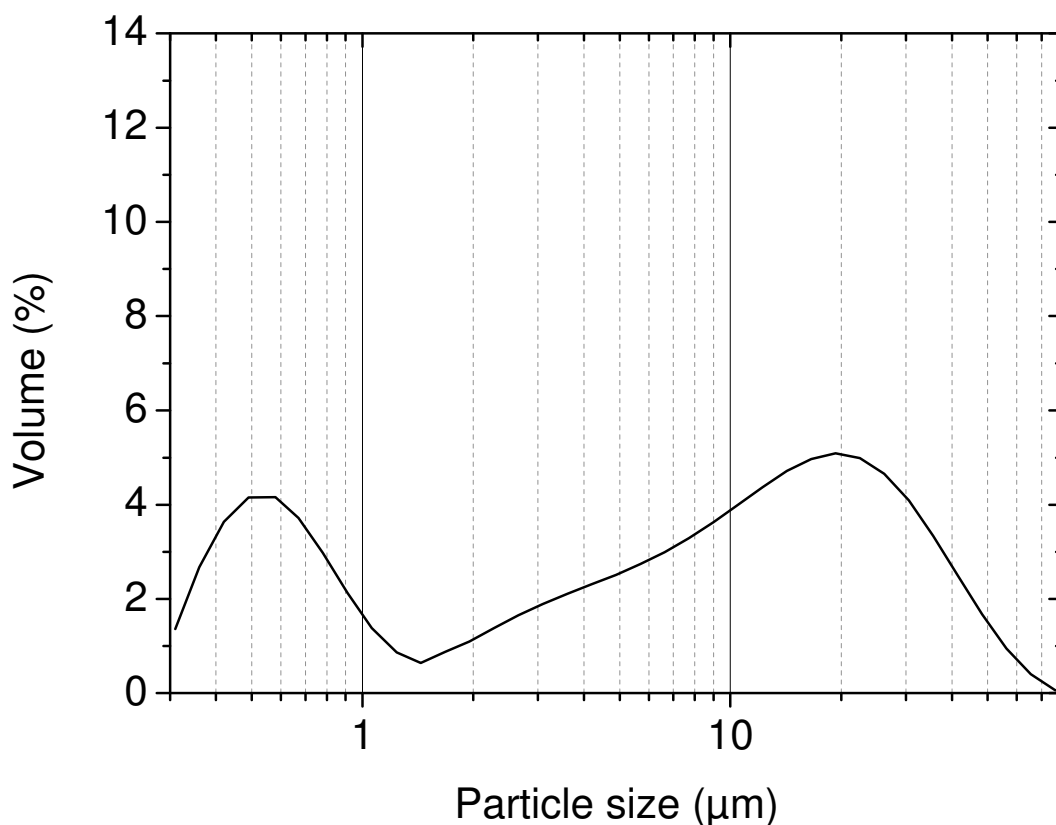


**Figure 38:** Particle size distribution for LMNO-R powders. Reproduced in part with permission from *J. Electrochem. Soc.*, 163, A470 (2016). Copyright 2016, The Electrochemical Society.<sup>103</sup>

**Figure 39** shows an XRD pattern and the relative fitting obtained from LMNO-R powders. This material exhibits no superstructure reflections suggesting the presence of  $\text{Mn}^{3+}$  in the structure. Accordingly, the fitting of the diffractogram was performed adopting the  $Fd3m$  space group. Furthermore, the diffractogram shows peaks in agreement with traces of rock-salt impurities. The obtained cell parameter ( $a$ ) results  $8.168(1) \text{ \AA}$  and suggests that LMNO-R does not contain significant amounts of  $\text{Mn}^{3+}$ , which would lead to larger ( $a$ ) values. The calculated crystallite size for LMNO-R is  $43 (\pm 1) \text{ nm}$  and results comparable with the crystallite size of LMNO-0. In summary, LMNO-R is a spinel material without tailored particle architecture, which presents smaller particle size, lower tap-density and higher surface area than LMNO-0. On the other hand, LMNO-R contains very low amounts of  $\text{Mn}^{3+}$  in the structure and presents a crystallite size comparable with LMNO-0. These characteristics allow comparing the

electrochemical results of LMNO-R and LMNO-0 electrodes in order to better understand the role of the morphology on the high-voltage electrolyte degradation.

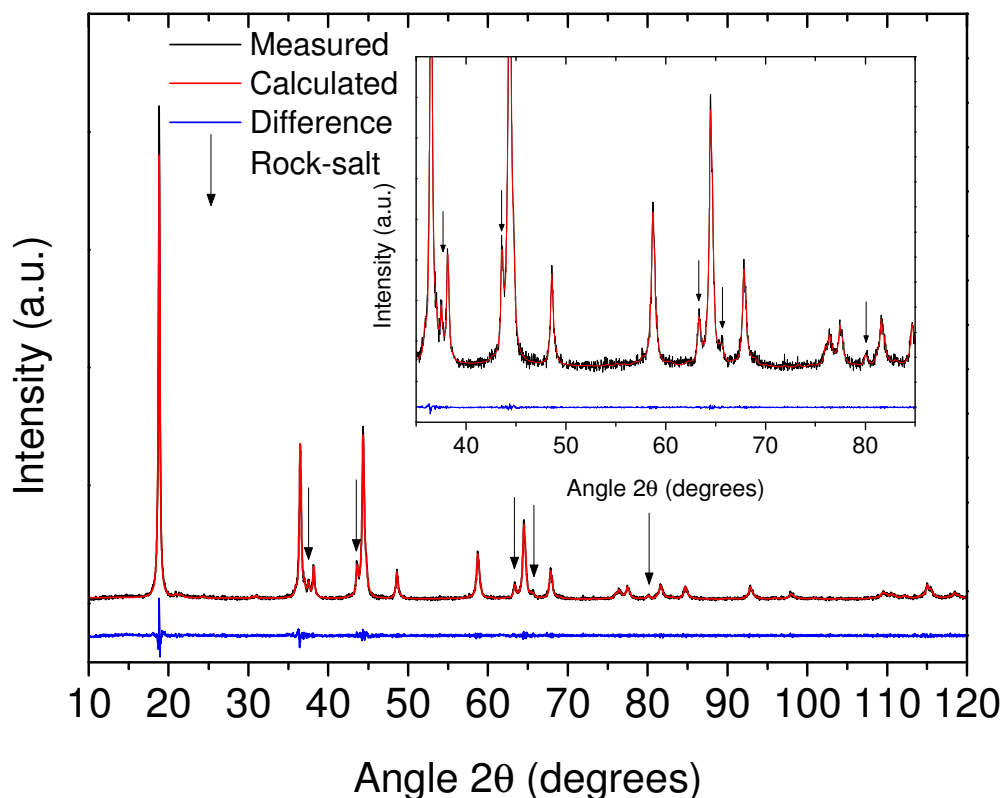


**Figure 39:** XRD pattern and fit for the sample LMNO-R. Reproduced in part with permission from *J. Electrochem. Soc.*, 163, A470 (2016). Copyright 2016, The Electrochemical Society.<sup>103</sup>

The electrochemical tests were performed on electrodes containing 87 wt.% active material (either LMNO-0 or LMNO-R), 7 wt.% conductive carbon and 6 wt.% polyvinylidene fluoride. The loading of the electrodes was ca. 10 mg cm<sup>-2</sup> based on the active material weight.

The first tests performed on both LMNO-0 and LMNO-R electrodes aimed to estimate the amount of electrolyte degradation occurring before and after the operating potential of LMNO. For this purpose, pristine LMNO-0 and LMNO-R electrodes underwent a linear sweep voltammetry from OCV up to 6 V vs. Li/Li<sup>+</sup>. During the potential scan, the current values before and after the working

potential of LMNO depend mainly on eventual secondary reactions occurring at the electrodes surface. **Figure 40** displays the results of these potential sweeps for LMNO-0 and LMNO-R electrodes obtained at a scan rate of  $0.1 \text{ mV s}^{-1}$ .

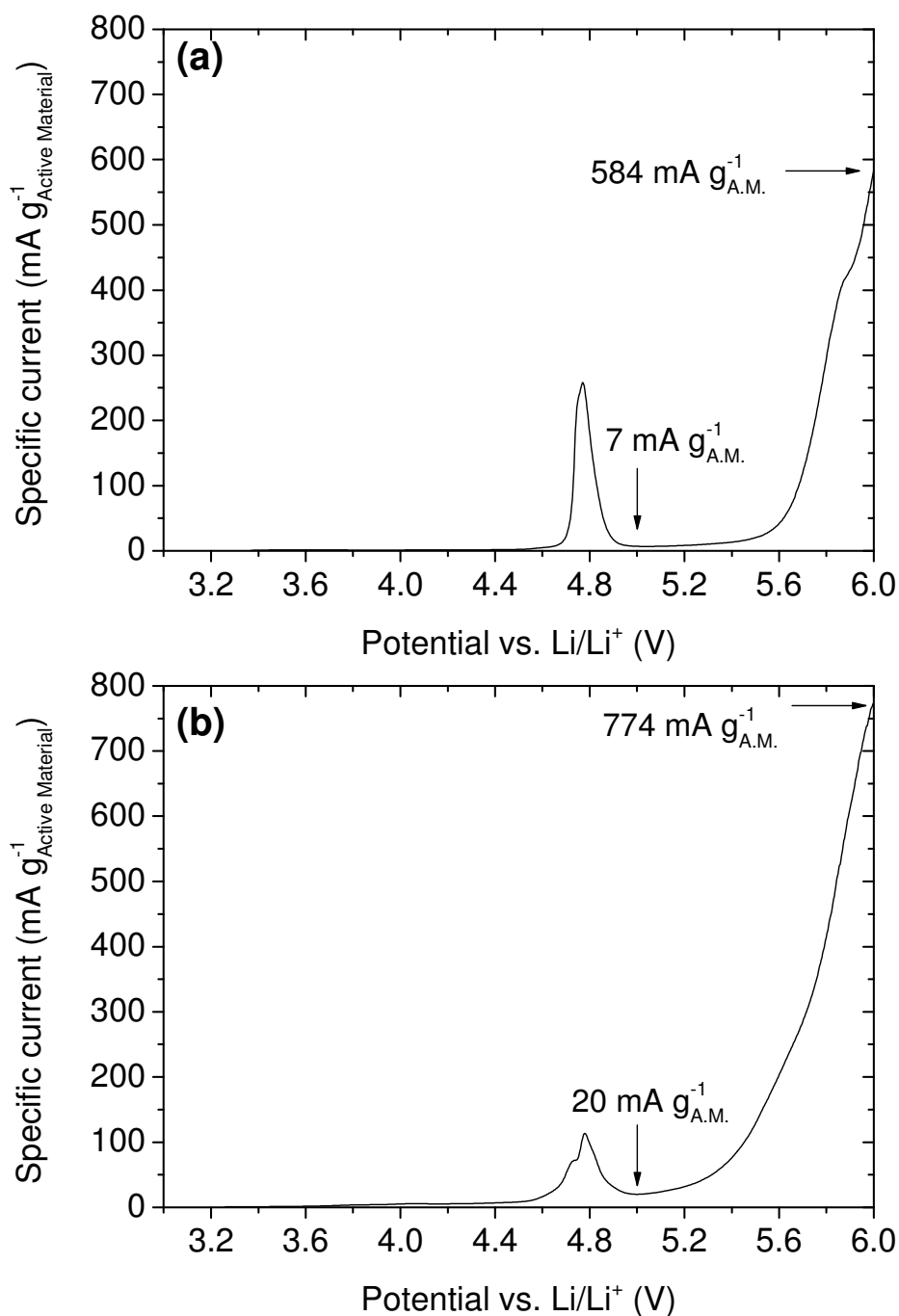


**Figure 40:** Linear potential sweep for LMNO-0 and LMNO-R electrodes. Reproduced with permission from *J. Electrochem. Soc.*, 163, A470 (2016). Copyright 2016, The Electrochemical Society.<sup>103</sup>

The first significant current appears at the potentials related to the Ni(II)/Ni(IV) redox couple and suggests that no significant electrolyte degradation occurs before the beginning of the delithiation process. Actually, LMNO-R electrodes show very low current values starting from ca. 4 V vs. Li/Li<sup>+</sup>. However, these current values regard the electrochemical activity of some Mn<sup>3+</sup> present in the structure of the active material and are not ascribable to electrolyte decomposition reactions. At 5 V vs. Li/Li<sup>+</sup>, the current related to the nickel oxidation process decreases and reaches a stable value, which suggests a complete delithiation of the electrodes. Starting from this potential, the current measured at the electrodes mainly depends on the collateral oxidation reactions. Above 5 V vs. Li/Li<sup>+</sup>, both LMNO-0 and LMNO-R electrodes present the same current trend, which suggests the same nature of secondary reactions occurring at the electrodes surface. However, LMNO-R electrodes show significantly higher current values than LMNO-0 electrodes and thus, higher electrolyte degradation rates. These results clearly show a relation between the degradation rates and the particle morphologies of the samples but unfortunately, they do not allow determining the onset potential of the degradation processes. For these reason, new LMNO-R and LMNO-0 electrodes underwent further specific electrochemical tests.

**Figure 41** shows the potential and current profiles of LMNO-0 and LMNO-R electrodes obtained by applying potentiostatic steps of 8 hours at 4.72, 4.76, 4.90 and 5.00 V vs. Li/Li<sup>+</sup> during charging. The aim of these potentiostatic steps is to reach the maximum electrodes delithiation at the applied potential and then measure the equilibrium current without the contribution of Ni (end of the potentiostatic step). Since no delithiation process occurs at the end of the potentiostatic step, the value of the equilibrium current mainly depends on the electrolyte degradation rate at the applied potential: higher electrolyte degradation rates lead to higher equilibrium currents. Before starting the test, the electrodes were galvanostatically cycled two times between 3.5 – 4.9 V vs. Li/Li<sup>+</sup> at C/5. Thereafter, they were charge according to the described procedure and discharged at C/5 for 10 times.



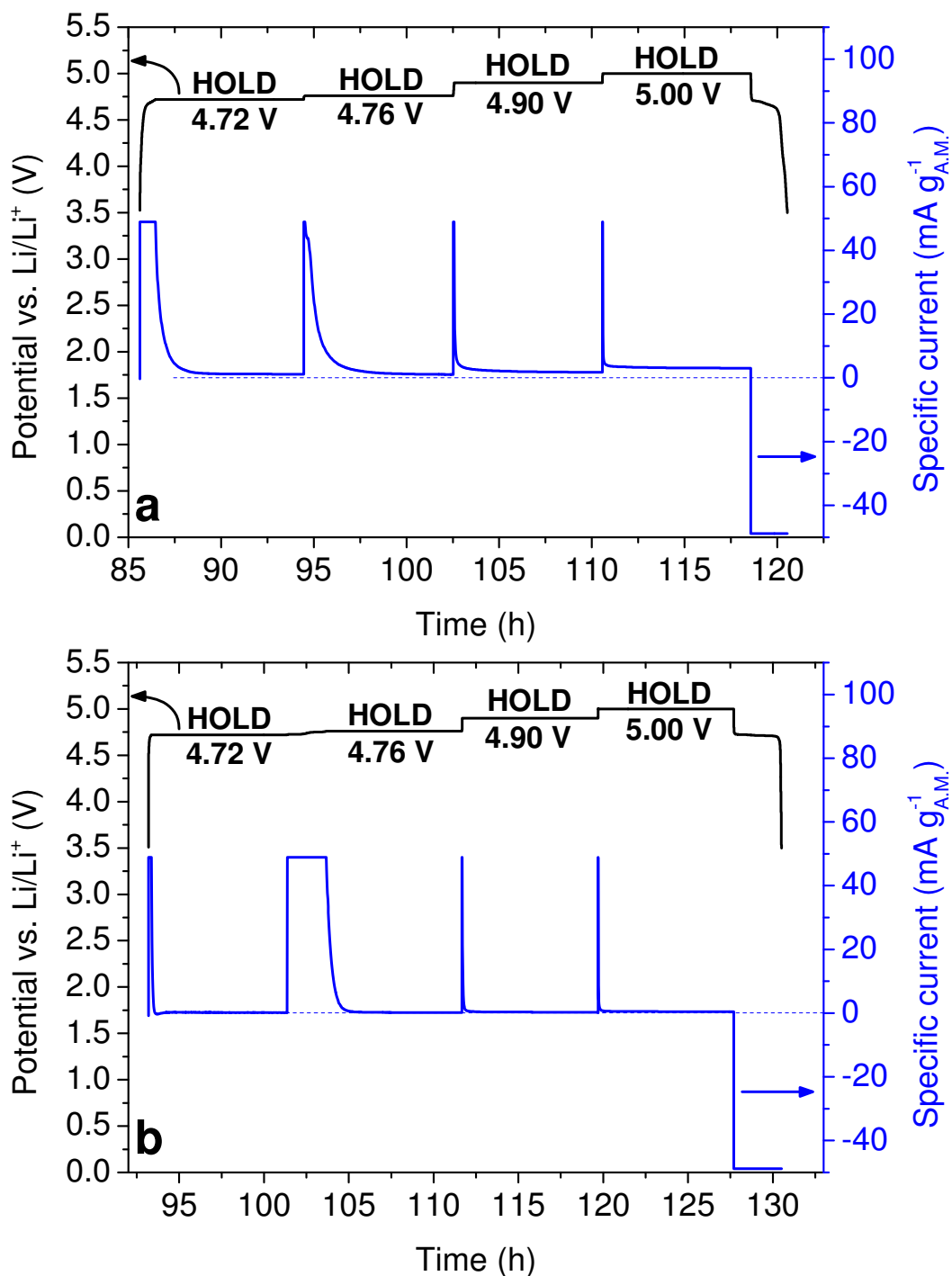


**Figure 41:** Potential profiles and current trends for (a) LMNO-0 and (b) LMNO-R electrodes obtained by holding the potential at 4.72, 4.76, 4.90 and 5.00 V vs. Li/Li<sup>+</sup>. Reproduced in part with permission from *J. Electrochem. Soc.*, 163, A470 (2016). Copyright 2016, The Electrochemical Society.<sup>103</sup>

**Table 2** reports the values of the equilibrium currents measured at the end of the potentiostatic steps. The reported values are the mean values obtained from 10 testing cycles.

**Table 2:** *Equilibrium current values measured at the end of the potentiostatic steps.*

	<b>4.72 V Current (mA g<sup>-1</sup>)</b>	<b>4.76 V Current (mA g<sup>-1</sup>)</b>	<b>4.90 V Current (mA g<sup>-1</sup>)</b>	<b>5.00 V Current (mA g<sup>-1</sup>)</b>
<b>LMNO-0</b>	0.19	0.20	0.35	0.52
<b>LMNO-R</b>	1.10	1.11	1.76	2.84

LMNO-0 and LMNO-R electrodes show no significant increase of the equilibrium current between 4.72 and 4.76 V vs. Li/Li<sup>+</sup>. This suggests that the electrolyte degradation rate does not increase along the charging plateaus of the electrodes. The situation looks different at 4.90 and at 5.00 V vs. Li/Li<sup>+</sup>, where the equilibrium currents are 1.7 and 2.6 times higher than at the 4.76 V vs. Li/Li<sup>+</sup>. This increase in the equilibrium current points out the onset of significant electrolyte decomposition reactions and underlines the importance of keeping the upper potential cut-off as close as possible to the last high-voltage plateau. The onset potential is the same for both LMNO-0 and LMNO-R electrodes. This data suggests once again that the nature of the decomposition reactions does not depend on the particles morphology. On the other hand, LMNO-R electrodes show values of equilibrium current ca. 5 times higher than LMNO-0 electrodes, confirming the key role of the morphology in limiting the electrolyte degradation rate at high potential. Also the coulombic efficiencies obtained during these tests (**Figure 42**) report similar results. The trend of the coulombic efficiency during cycling is again the same for LMNO-0 and LMNO-R electrodes but the values obtained at each cycle are significantly higher for LMNO-0 electrodes.

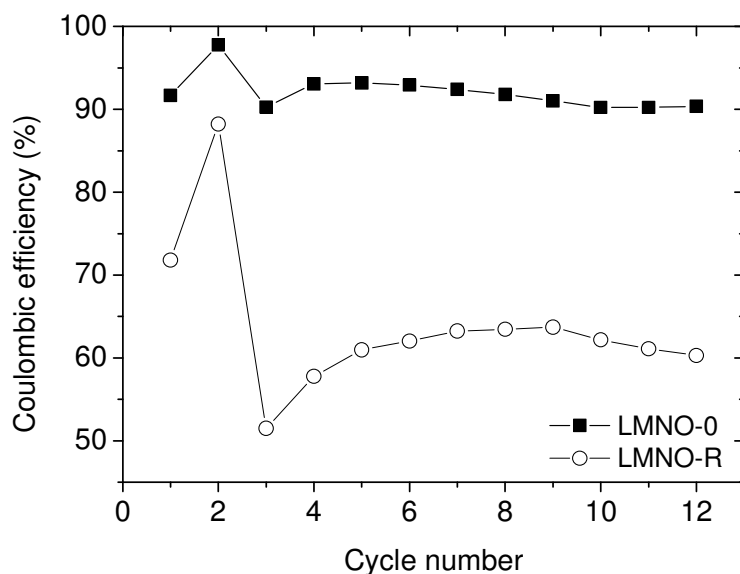


**Figure 42:** Trend of the coulombic efficiency for LMNO-0 and LMNO-R electrodes cycled two times between 3.5 and 4.9 V vs.  $\text{Li}/\text{Li}^+$  and then 10 times holding the potential at 4.72, 4.76, 4.90 and 5.00 V vs.  $\text{Li}/\text{Li}^+$  during charging.

As mentioned in *Chapter 1.5*, the electrolyte decomposition processes form different by-products, which can deposit on the surface of LMNO electrodes and form a passivation film. As previously described, also graphite anodes form a passivation film (SEI), which is stable during cycling and prevents further electrolyte degradation without compromising the  $\text{Li}^+$  diffusion. In the case of LMNO electrodes, the formed film partially limits further electrolyte decomposition and thus, it keeps growing during cycling. This thickening process consumes charge and electrolyte at each cycle leading to capacity fade and aging of the cells. Additionally, the formation of thick films increases the electrodes resistance and causes an early reaching of the upper potential cut-off similar to that described in *Chapter 4*. It is possible to investigate and compare the film formation process on LMNO-0 and LMNO-R electrodes by impedance spectroscopy measurements during cycling. Generally, the impedance spectra of LMNO electrodes consist in the combination of: a semicircle at high frequencies related to the surface film, a second semicircle at high to medium frequencies related to the charge-transfer process and a slopping line at low frequencies associated to a Warburg-type diffusion.<sup>67,70</sup> **Figure 43** reports the impedance

spectra and the related fittings for LMNO-0 and LMNO-R electrodes recorded at 4.9 V vs. Li/Li<sup>+</sup>. The impedance spectra were fitted according to the equivalent circuit shown in **Figure 43a**, where  $R_U$  is the uncompensated resistance,  $C_F$  is the capacitance of the film,  $R_F$  is the resistance of the film,  $C_{CT}$  is the capacitance of the charge-transfer,  $R_{CT}$  is the resistance of the charge transfer and  $W$  is the Warburg diffusion element. According to this circuit, the small semicircle at high frequencies allows determining and comparing the resistances of the surface films ( $R_F$ ) formed on LMNO-0 and LMNO-R electrodes during cycling.

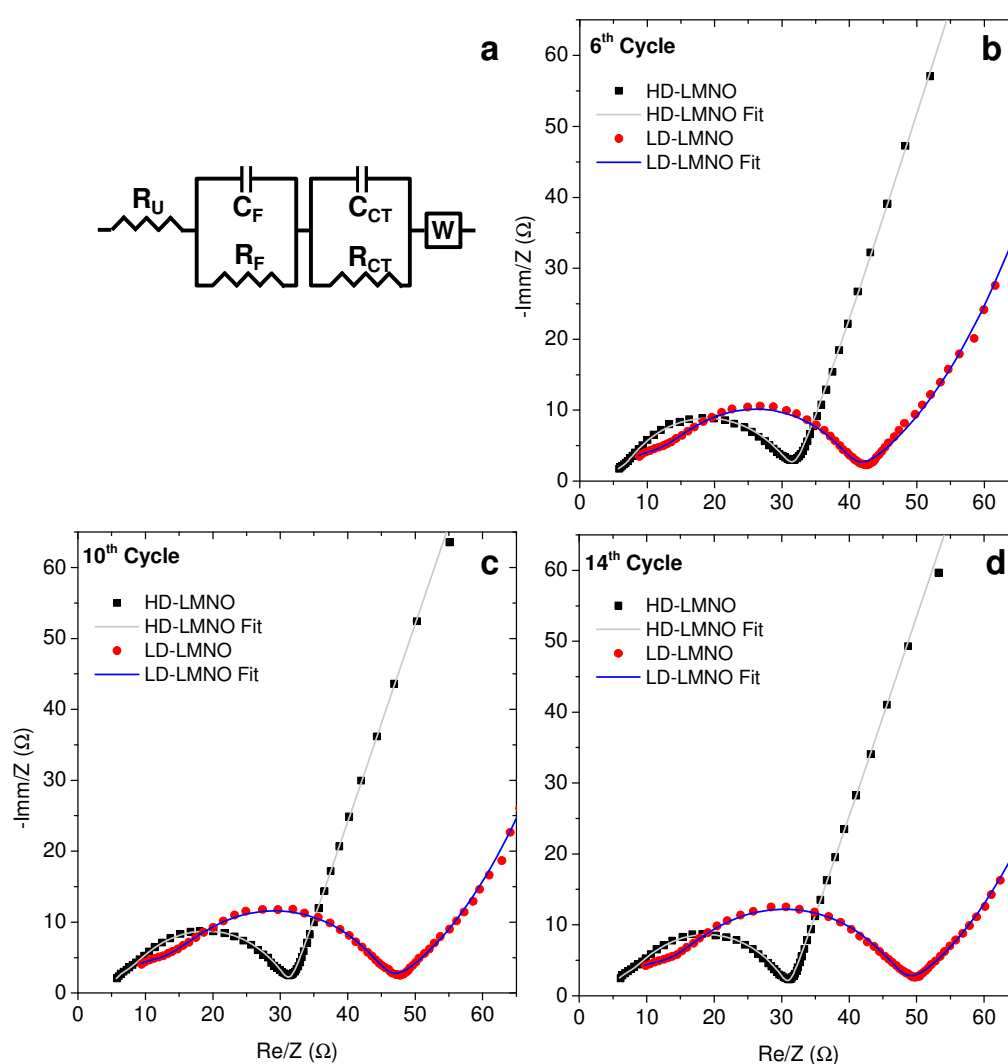


**Figure 43:** (a) Equivalent circuit, impedance spectra and relative fittings obtained at the (b) 6<sup>th</sup>, (c) 10<sup>th</sup> and (d) 14<sup>th</sup> cycle of LMNO-0 and LMNO-R electrodes. Adapted and reproduced with permission from *J. Electrochem. Soc.*, 163, A470 (2016). Copyright 2016, The Electrochemical Society.<sup>103</sup>

**Figure 44** displays and compares the  $R_F$  values determined for LMNO-0 and LMNO-R electrodes. Both these electrodes show the same  $R_F$  trend during cycling, which suggests similar film formation processes. The larger increase of  $R_F$  between the 6<sup>th</sup> and the 10<sup>th</sup> cycle is ascribable to initial significant thickening of the films. The formed films partially passivate the surface of the electrodes and lead to lower resistance increase between the 10<sup>th</sup> and the 14<sup>th</sup> cycle. LMNO-R electrodes show  $R_F$  values ca. 5 times higher than LMNO-0 electrodes. This difference suggests the formation of more extend films on the LMNO-R electrodes surface and points out a relation between the electrolyte degradation rate and the film thickening during cycling. According to these results, the particle morphology of LMNO-0 does not influence how the passivation films form on the electrodes but it significantly reduces thickening process during cycling and guarantees lower electrodes resistances.

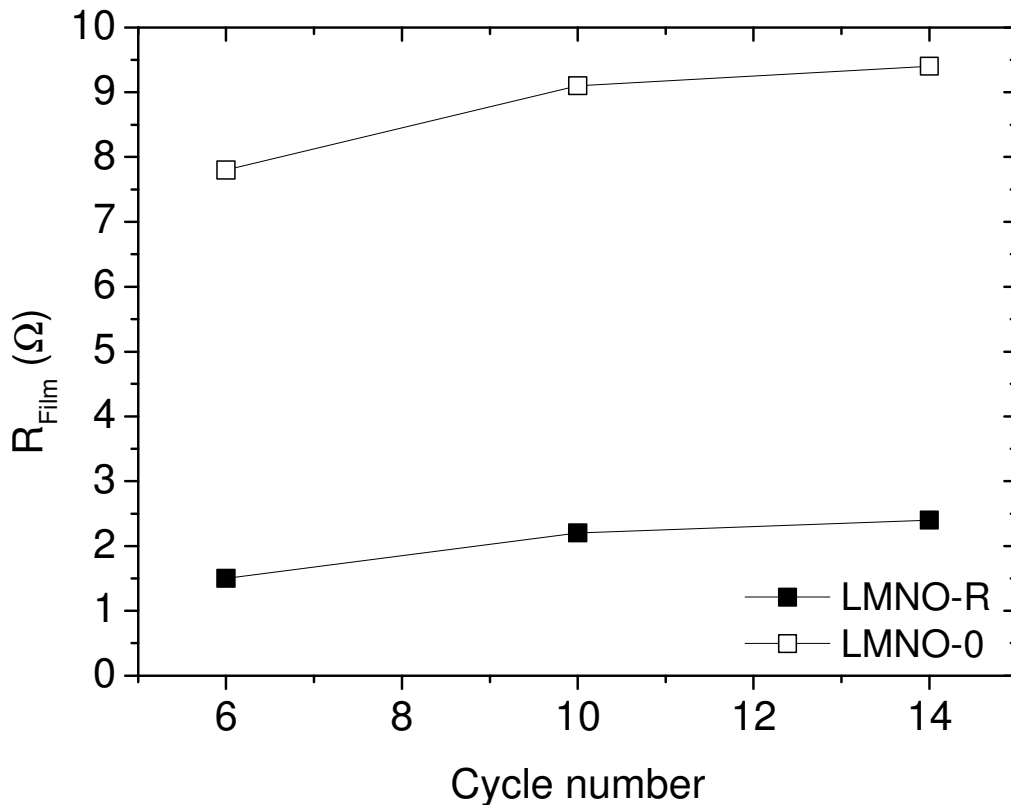


**Figure 44:** Trend of the  $R_F$  during cycling for LMNO-0 and LMNO-R electrodes.

The results presented in this chapter clearly point out the role of particle morphology on electrolyte degradation processes. According to these results, the optimized particle morphology of LMNO-0 drastically reduces the rate of the electrolyte degradation processes and the aging of the electrodes during cycling. On the other hand, the nature of the degradation processes does not depend on the particle architectures. This suggests that the decomposition reactions and the formed by-products only depend on the surface chemistry of LMNO.

## 5.2 CHARGE OPTIMIZATION OF LMNO-0 ELECTRODES.

As shown in the previous chapter, the onset of significant electrolyte decomposition reactions for LMNO electrodes is just above its operating potential. Thus, it is possible to limit the electrolyte decomposition also by defining suitable charging protocols, which guarantee complete electrodes delithiation with upper cut-offs close to the operating potential.

Applying a potentiostatic step at the end of the galvanostatic charge guarantee full electrodes delithiation and lower cut-off potential. However, during the potentiostatic steps, the electrolyte can incur significant degradation processes. It is not easy to determine whether a potentiostatic step is beneficial or not for LMNO electrodes and it is necessary to evaluate different factors, such as the selected cut-off potential, the length of the potentiostatic step and the desired charging rate.

The first parameter to define is the upper potential cut-off suitable for the potentiostatic step. This parameter was evaluated by charging LMNO-0 electrodes up to different potentials (C/5), exposing them to a potentiostatic step and finally discharging them (C/5) to 3.5 V vs. Li/Li<sup>+</sup> (**Figure 45a**). The different investigated potentials correspond to the beginning of the first delithiation plateau (4.73 V vs. Li/Li<sup>+</sup>), the beginning of the second delithiation plateau (4.75 V vs. Li/Li<sup>+</sup>), the conclusion of the second delithiation plateau (4.8 V vs. Li/Li<sup>+</sup>) and the standard LMNO upper cut-off (4.9 V vs. Li/Li<sup>+</sup>). In these tests, the applied potentiostatic steps lasted until the measured current decreased below C/20. In order allow the formation of a passivation layer, the test included two initial galvanostatic cycles between 4.9 - 3.5 V vs. Li/Li<sup>+</sup>.

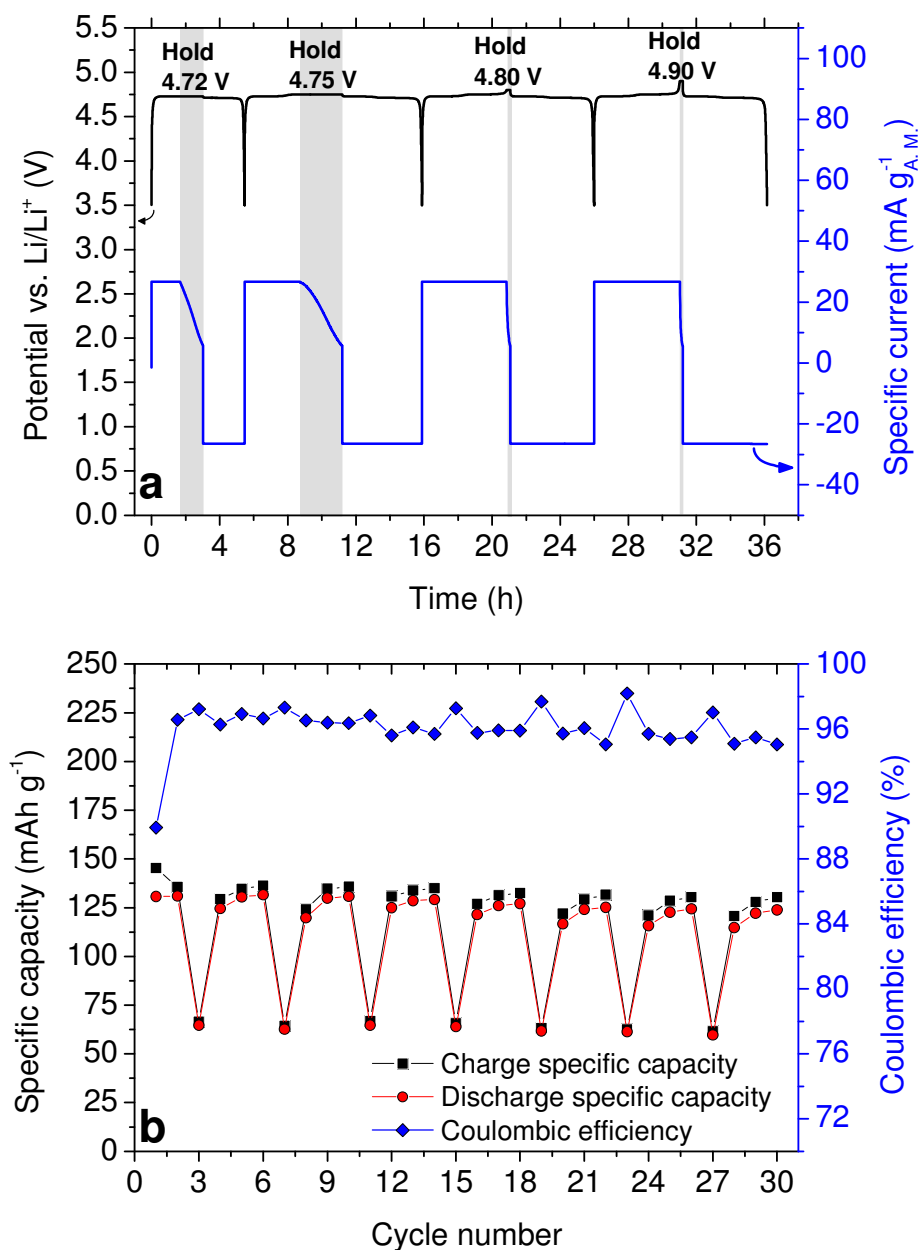


**Figure 45:** (a) Potential and specific current profiles, (b) discharge specific capacity and coulombic efficiency for LMNO-0 electrodes charged with a potentiostatic step at different cut-offs. Reproduced with permission from *J. Electrochem. Soc.*, 163, A470 (2016). Copyright 2016, The Electrochemical Society.<sup>103</sup>

According to this procedure, the discharge capacities point out the maximum electrodes delithiation achievable with the selected potential cut-off. At the same time, the coulombic efficiencies allow estimating the contribution of the potentiostatic step to the electrolyte decomposition (**Figure 45b**). The lowest cut-off (4.73 V vs.  $\text{Li/Li}^+$ ) provides discharge capacities related only to the first



intercalation plateau of LMNO ( $63 \text{ mAh g}^{-1}$ ). The second cut-off ( $4.75 \text{ V vs. Li/Li}^+$ ) allows using also the second high-voltage plateau and leads to a discharge capacity of  $120 \text{ mAh g}^{-1}$ . The maximum discharge capacity (ca.  $126 \text{ mAh g}^{-1}$ ) is achievable at both  $4.80$  and  $4.9 \text{ V vs. Li/Li}^+$ . However, the coulombic efficiency at  $4.9 \text{ V vs. Li/Li}^+$  is worse than at  $4.8 \text{ V vs. Li/Li}^+$ .

According to the obtained results, the cut-off potential suitable for potentiostatic steps is  $4.8 \text{ V vs. Li/Li}^+$ .

Once determined the suitable cut-off potential, it is possible to determine the optimal duration of the potentiostatic step and the benefits achievable at different charging rates. This second investigation consisted in cycling LMNO-0 electrodes at different C-rates according to three different charging methods:

*Method 1:* galvanostatic charge and discharge between  $4.9 - 3.5 \text{ V vs. Li/Li}^+$ .

*Method 2:* galvanostatic charge and short potentiostatic step (current limit =  $C/10$ ) at  $4.8 \text{ V vs. Li/Li}^+$  followed by galvanostatic discharge to  $3.5 \text{ V vs. Li/Li}^+$ .

*Method 3:* galvanostatic charge and long potentiostatic step (current limit =  $C/20$ ) at  $4.8 \text{ V vs. Li/Li}^+$  followed by galvanostatic discharge to  $3.5 \text{ V vs. Li/Li}^+$ .

**Figure 46** summarises the discharge capacities and the coulombic efficiencies obtained for LMNO-0 electrodes cycled according these methods.

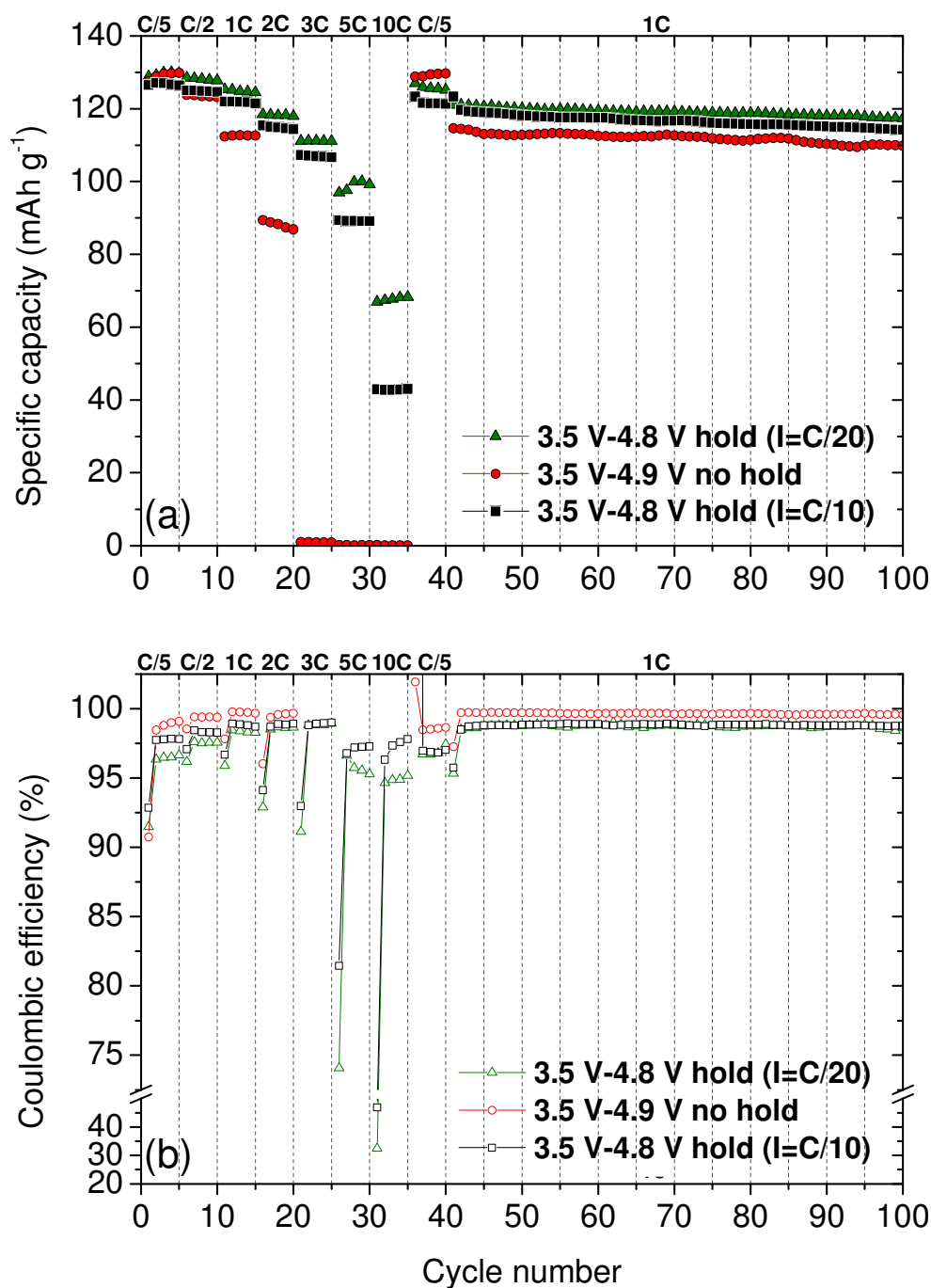


**Figure 46:** (a) Discharge capacity and (b) coulombic efficiency of LMNO-0 cycled according to different charging procedures. Adapted and reproduced with permission from *J. Electrochem. Soc.*, 163, A470 (2016). Copyright 2016, The Electrochemical Society.<sup>103</sup>

The discharge capacities in **Figure 46a** show no improvements related to the potentiostatic steps by charging the electrodes at rates below 1C. This result indicates that *Method 1* is sufficient to obtain a complete charge of LMNO-0 electrodes using C-rates < 1C. The obtained coulombic efficiencies (**Figure 46b**)

result very high and always above 98% (except at the 1<sup>st</sup> cycle). Increasing the C-rate to 1C and 2C, the potentiostatic steps significantly affects the obtained discharge capacities and thus, it is possible to completely delithiate LMNO-0 electrodes only using *Method 2* and *Method 3*. The presence of potentiostatic steps influences also the coulombic efficiencies of the electrodes. However, the lower cut-off of *Method 2* and *Method 3* limits the electrolyte decomposition and the difference in the coulombic efficiency between the tested methods is acceptable. Starting from 3C, LMNO-0 electrodes charged with *Method 1* show the typical capacity drop down already discussed in *Chapter 4.2.2*. Applying the potentiostatic steps allows avoiding this phenomenon and leads to good delithiation of LMNO-0 electrodes also at higher C-rates. Above 3C, *Method 3* guarantees better discharge capacities than *Method 2*. However, cycling LMNO-0 electrodes above 3C does not lead to any capacity uptake during the galvanostatic step and the entire charging process takes place along the potentiostatic step. Thus, using C-rates  $\geq 3C$  does not lead to significant improvements in the overall charging time of LMNO-0 electrodes. Furthermore, also below 3C, longer potentiostatic steps always require longer charging times without leading to significant improvements of the discharge capacity.

According to the obtained results, *Method 1* is the best charging procedure for LMNO-0 electrodes cycled at C-rates  $< 1C$ , while *Method 2* allows faster and efficient charge at 1C and 2C. Further increases of the C-rate do not lead to any improvements on the charging time and therefore, they are not useful for LMNO-0 electrodes.

## 6. RESULTS AND DISCUSSION – Part III

### 6.1 LiNbO<sub>3</sub> SURFACE TREATMENT OF LMNO

The electrochemical performance of LMNO and the rate of the electrolyte degradation considerably depend on the particles morphology. The optimised LMNO particle architecture described in the previous chapters was identified as the best compromise between electrochemical performance and reduced electrolyte degradation rate. As discussed in *Chapter 1.5* and *Chapter 3.1.3*, it is possible to further improve the stability of the active material/electrolyte interface by coating the particles surface with a suitable material. Among the possible coating materials, lithium niobate (LiNbO<sub>3</sub>) presents different attractive features, which make this material a potential candidate for the treatment of LMNO particles. Thus, LMNO powders presenting optimised particle architecture were treated with LiNbO<sub>3</sub>, obtaining the coated sample LMNO-T.

The metal composition of LMNO-T was investigated by ICP analyses obtaining a Li : Ni : Mn ratio of 1.0 : 0.5 : 1.5. Additionally, LMNO-T presents a Niobium content of 0.5 wt.%, corresponding to 0.8 wt.% in terms of LiNbO<sub>3</sub>.

**Figure 47** reports the SEM images obtained from LMNO-Nb. This sample shows exactly the same particle architecture observed for LMNO-0 and no morphological alteration due to the LiNbO<sub>3</sub> treatment. Indeed, the LiNbO<sub>3</sub> treatment is expected to involve just the surface of the primary crystallites without modifying the tailored particle architecture and its properties.

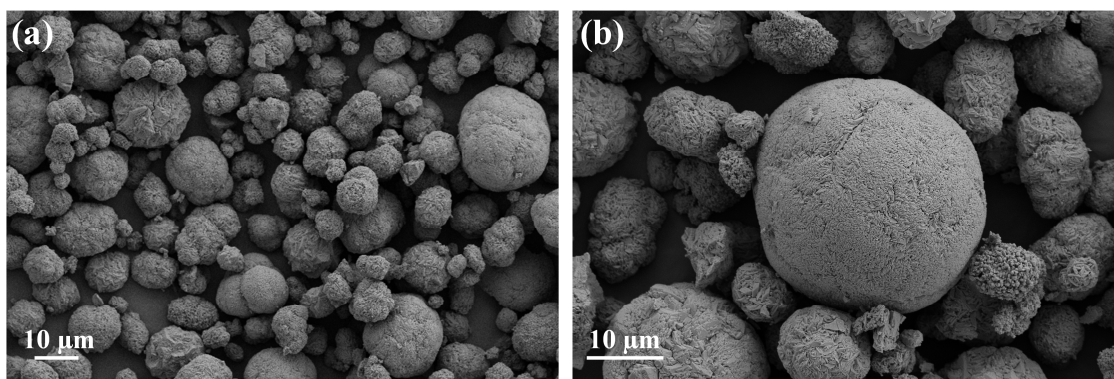


**Figure 47:** SEM images of LMNO-T at different magnifications.

The surface of the LMNO-T sample was investigated via TEM-EDX and TEM-EELS analyses at the Natural and Medical Sciences Institute (NMI) at the University of Tübingen. **Figure 48** reports the obtained TEM images together with the corresponding EDX and the EELS analyses. From these analyses, it is possible to verify the bulk elemental composition of the sample, confirm the presence of the Nb on the particles surface and evaluate the quality of the coating. The EDX analyses reported in **Figure 48** clearly show intense Ni, Mn and O signals mainly related to the LMNO bulk composition. LMNO-T also presents Nb signals homogeneously distributed on the crystallites surface. High-resolution TEM-EELS analyses (**Figure 48d, f, h, j**), confirm once again the bulk composition of the particle and clearly show a thin Nb film homogeneously distributed and localised on the surface of primary crystallites. These analyses confirm the validity of the coating method and the very good quality of the film deposited on LMNO particles.

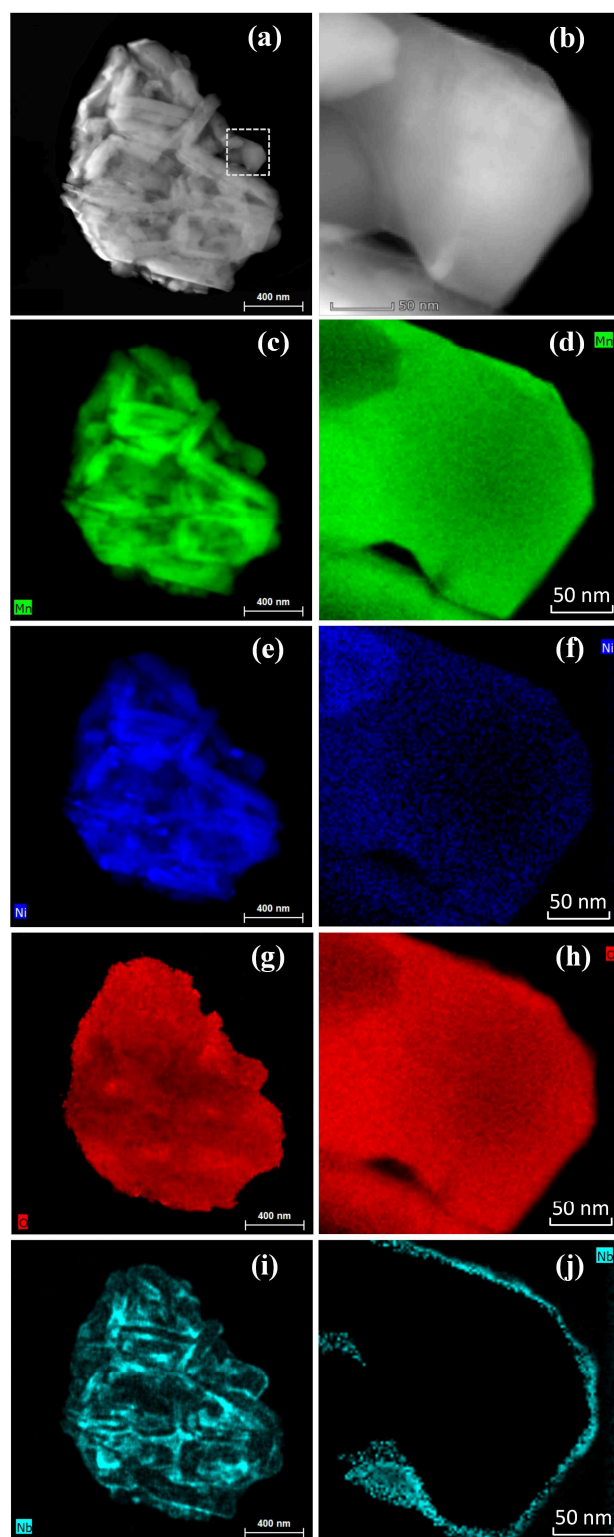


**Figure 48:** (a); (b) TEM images, (c); (e); (g); (i); EDX analyses and (d); (f); (h); (j) EELS analyses of LMNO-T particles. The green, blue, red and light blue colours correspond to the detected Mn, Ni, O and Nb, respectively. Adapted and reproduced with the permission from ChemSusChem. 2016, DOI: 10.1002/cssc.201600278. Copyright 2016 WILEY-VCH Verlag GmbH & Co. KGaA.<sup>88</sup> License Number: 3883560968998

The uncoated LMNO samples and the coated LMNO-Nb were also investigated by X-Ray Photoelectron Spectroscopy (XPS) at the Institute of Surface Chemistry and Catalysis at the University of Ulm. The first fundamental difference between the coated and the uncoated samples was detected in the Nb(3d) region of the XPS spectra (**Figure 49a**), where only LMNO-T shows the peak component related to Nb(V) at 207.0 eV. This peak confirms the presence of Nb on the surface of LMNO-T and results in very good agreement with the value obtained in literature for  $\text{LiNbO}_3$  (207.1 eV).<sup>115,116</sup> A second key difference between the coated and the uncoated LMNOs appears in the Mn(3p)/Li(1s) region of the spectra (**Figure 49b**). In this region, LMNO-T presents two Li(1s) peaks (53.9 eV and 55.0 eV), while the uncoated sample shows only one peak at 53.9 eV. The Li(1s) peak visible in both samples (53.9 eV) corresponds to the lithium inside the LMNO structure, while the additional peak observed for LMNO-T (55.0 eV) is again in good agreement with the data reported in literature for  $\text{LiNbO}_3$ .<sup>115,116,117</sup>

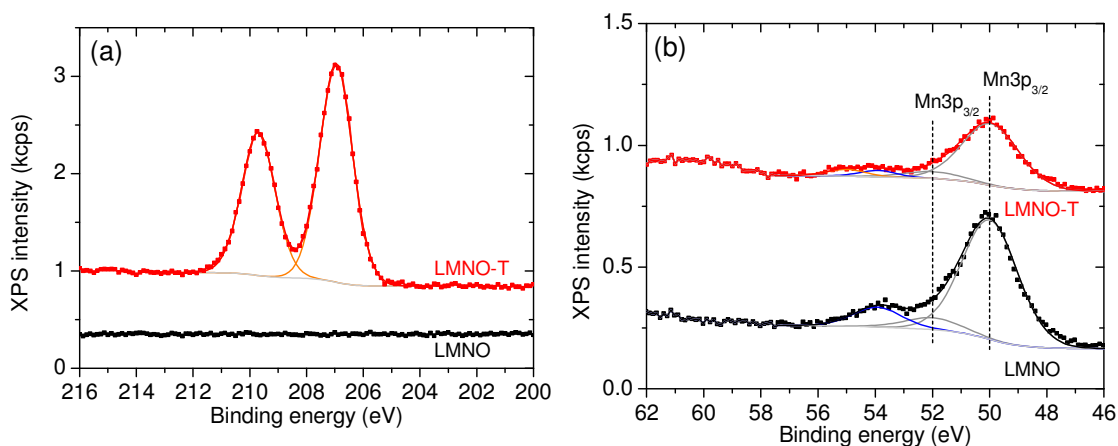


**Figure 49:** XPS spectra for LMNO-T and LMNO (a) in the Nb(3d) and (b) in the Mn(3p)/Li(1s) regions. Adapted and reproduced with the permission from ChemSusChem. 2016, DOI: 10.1002/cssc.201600278. Copyright 2016 WILEY-VCH Verlag GmbH & Co. KGaA.<sup>88</sup> License Number: 3883560968998

The results of the XPS analyses and their good agreement with the literature suggest a successful coating of the LMNO surface with  $\text{LiNbO}_3$ . However, this

technique cannot provide a univocal identification of the  $\text{LiNbO}_3$  phase and the coated material could also present additional similar phases on the surface.

**Figure 50** displays the XRD patterns obtained from LMNO-T powders. The pattern presents peaks related to the LMNO spinel phase but it does not show peaks ascribable to  $\text{LiNbO}_3$  crystalline phase. The absence of these peaks is not unexpected and it is probably related to the very low amounts of  $\text{LiNbO}_3$  present in the sample. Additionally, the low-temperature coating procedure should form mainly amorphous  $\text{LiNbO}_3$ , which is barely detectable via XRD analyses.

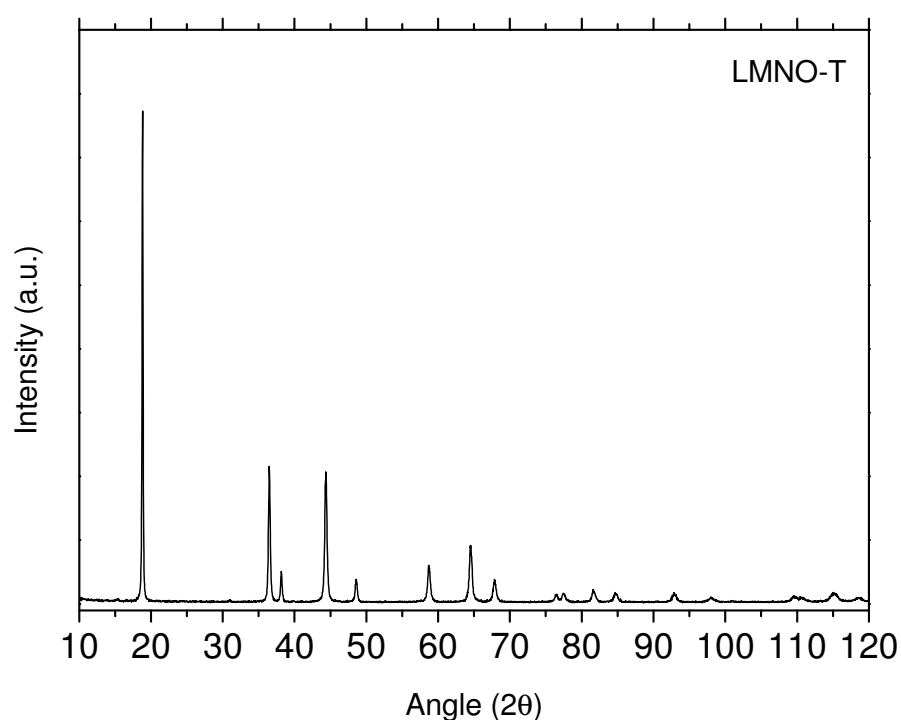


**Figure 50:** XRD patterns of LMNO-T.

Electrodes made with LMNO-T were tested in half-cells configuration in order to compare the electrochemical performances of this material with the results obtained for LMNO-0 electrodes. All the cathodes presented in this chapter had a composition of 88 wt.% active material, 8 wt.% conductive carbon and 4 wt.% polyvinylidene fluoride. The active material loading was in line with commercial cathodes for Li-ion batteries (ca.  $15 \text{ g cm}^{-2}$ ).



**Figure 51** reports the discharge specific capacity and the coulombic efficiency of LMNO-T electrodes. These electrodes were always charged at C/3 and then discharged at different C-rates.

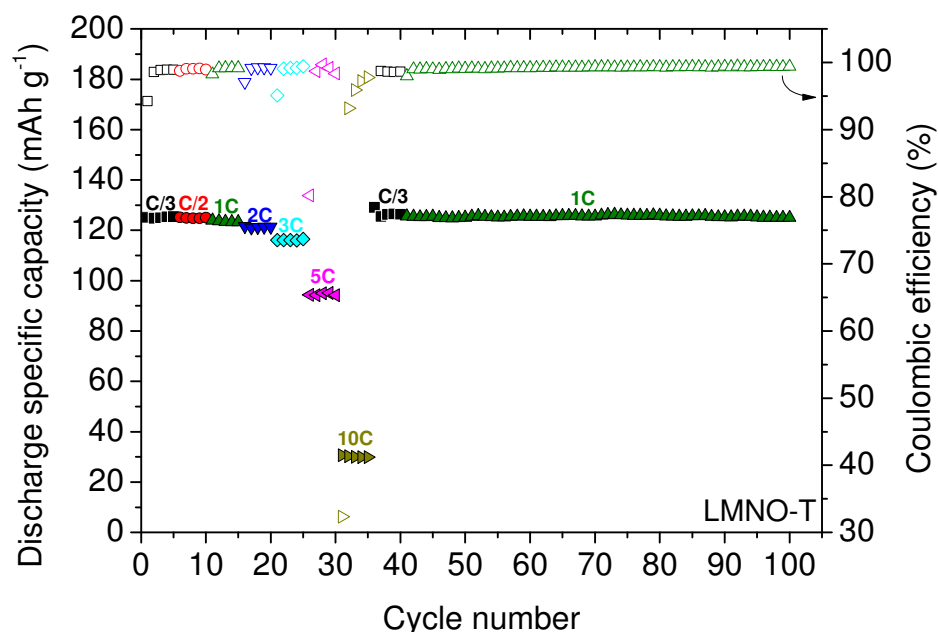


**Figure 51:** Discharge specific capacity and coulombic efficiency of LMNO-T electrodes. Reproduced in part with the permission from ChemSusChem. 2016, DOI: 10.1002/cssc.201600278. Copyright 2016 WILEY-VCH Verlag GmbH & Co. KGaA.<sup>88</sup> License Number: 3883560968998

The obtained results show high discharge capacities, stable coulombic efficiency above 98 % and very good capacity retention during cycling. The electrochemical performance obtained from LMNO-T electrodes in half cells are in very good agreement with those obtained with LMNO-0 electrodes. This suggests that the  $\text{LiNbO}_3$  coating does not compromise the electrochemical performances guaranteed by the tailored particle morphology. The electrochemical results obtained from LMNO-T electrodes in half-cells do not show any further improvement or difference related to the coating. In facts, the metallic lithium adopted as counter electrode guarantees a continuous  $\text{Li}^+$  source and avoids all the aging phenomena related to full Li-ion cells. Thus, LMNO-T

electrodes are suitable for full cell tests, where the aging effects strongly depend on the interactions between cathode, anode and electrolyte.

## 6.2 REALIZATION OF GRAPHITE/LMNO FULL CELLS

The optimised particle architecture described for LMNO-0 guaranteed remarkable electrochemical performance and high coulombic efficiency when tested in half-cells versus Li. The  $\text{LiNbO}_3$  coating described in the previous chapter does not compromise these electrochemical performances but on the other hand, it does not show any visible improvement to the already remarkable results obtained with LMNO-0 electrodes in half-cells. In order to better characterise these materials, the effects of both particle architecture and  $\text{LiNbO}_3$  coating were evaluated versus graphite anodes in full Li-ion cells.

Graphite anodes operate at potentials close to 0 V vs.  $\text{Li/Li}^+$  guaranteeing high cell voltage and high specific energy. On the other hand, these low potentials can lead to Li plating and dendrites formation at the anode surface drastically increasing the risk of short-cuts and thermal runaway of the cell. For safety reasons, it is extremely important to balance the active material loadings of the electrodes in order to guarantee charge excess at the anode. This way, the Li extracted from the cathode during charging is not enough to fully lithiate the graphite and the anode potential remains far enough from the critical value of 0 V vs.  $\text{Li/Li}^+$ . Because of the low operating potentials, graphite anodes also consume part of the available Li for the SEI formation process during the first charge. Thus, it is important to not exceed the amount of extra anode charge required for avoiding the Li plating.

Full Li-ion cells assembled with LMNO as cathode material lead to electrolyte degradation phenomena at high potential and thus, it is extremely important to reach the right upper cut-off potential during cycling. Also in this case, the cell balancing plays a key role in order to achieve at the same time a safe potential at the anode and the right cut-off potential at the cathode during charging.

In the case of Graphite/LMNO cells, the balancing was carried out considering the practical capacity of LMNO cathodes and graphite anodes. Cycling at C/3, LMNO cathodes showed discharge capacities of ca.  $130 \text{ mAh g}^{-1}$ , while graphite

electrodes presented discharge capacities of  $310 \text{ mAh g}^{-1}$  after few cycles in half-cell (**Figure 52**).

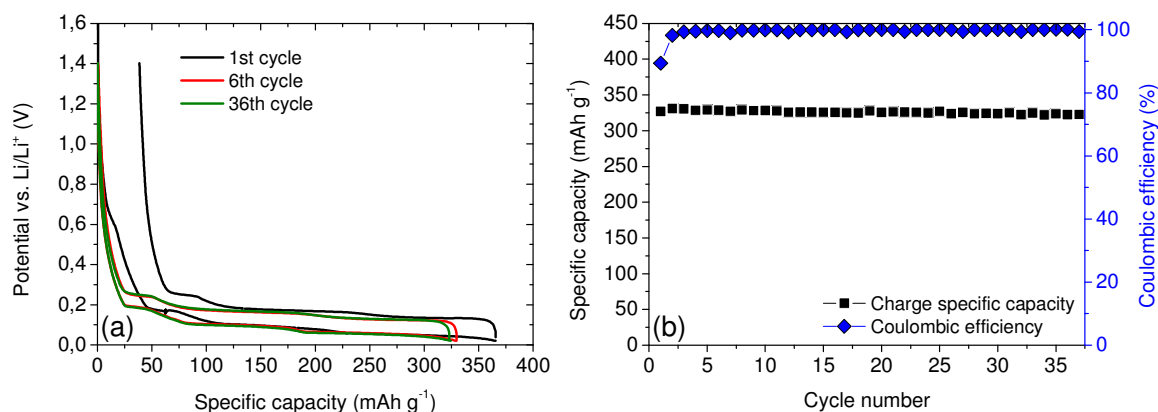


**Figure 52:** Voltage profiles and specific capacity of Graphite anodes cycled in half-cells at  $C/4$ . Reproduced with the permission from ChemSusChem. 2016, DOI: 10.1002/cssc.201600278. Copyright 2016 WILEY-VCH Verlag GmbH & Co. KGaA.<sup>88</sup> License Number: 3883560968998

The assembled full cells had a Graphite : LMNO weight ratio of ca. 1.7, which correspond to 40 % anode charge excess according to the practical capacities of the electrodes. In order to determine the most suitable operating voltage window, Graphite/LMNO cells were tested in three-electrode configuration using Li as reference electrode and controlling separately anode and cathode potentials. **Figure 53** displays the cell voltage and electrodes potential (vs.  $\text{Li/Li}^+$ ) reached in a balanced Graphite/LMNO cell at the 3<sup>rd</sup> cycle.

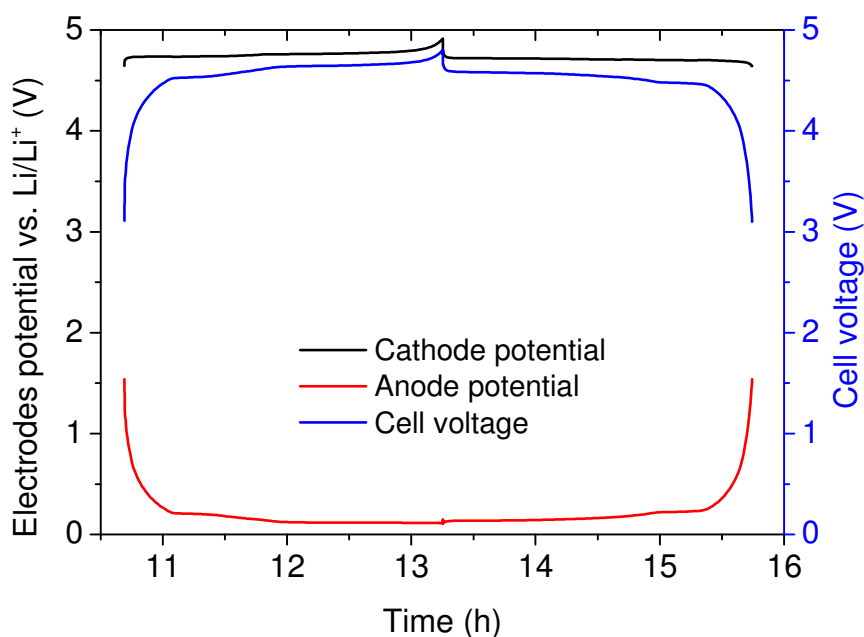


**Figure 53:** Electrodes potential profiles and cell voltage of a Graphite/LMNO full cell.

According to the measured electrodes potentials, it is possible to reach 4.9 V vs.  $\text{Li/Li}^+$  at the cathode and 0.1 V vs.  $\text{Li/Li}^+$  at the anode by setting the upper and the lower cell cut-off voltage at 4.8 and 3.1 V, respectively.

The first generation of full cells were assembled using the morphologically optimised LMNO as cathode material and aimed to point out the effect of the particle architecture on the electrochemical performance. **Figure 54** shows the potential profile and the cycling stability of a Graphite/LMNO coin cell cycled at C/3 between 4.8 – 3.1 V.

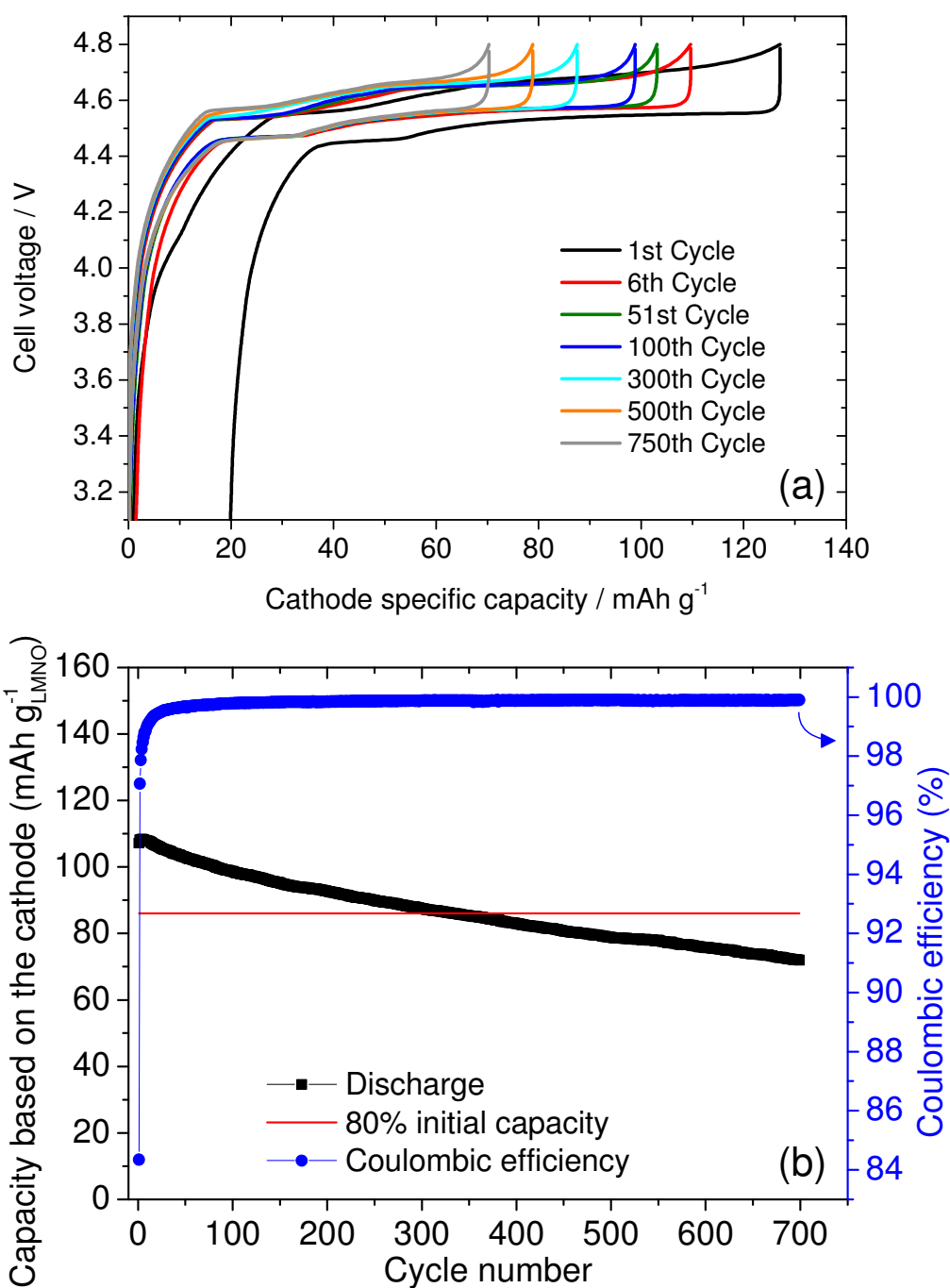


**Figure 54:** (a) Potential profiles and (b) cycling stability of a Graphite/LMNO full cell. Reproduced in part with the permission from ChemSusChem. 2016, DOI: 10.1002/cssc.201600278. Copyright 2016 WILEY-VCH Verlag GmbH & Co. KGaA.<sup>88</sup> License Number: 3883560968998

These cells present high-voltage electrochemical activity, with a charge plateau at ca. 4.6 V and a discharge plateau at ca. 4.5 V. During the first charge/discharge cycles, the electrodes undergo SEI and film formation

processes. Therefore, these cells show ca.  $108 \text{ mAh g}_{\text{LMNO}}^{-1}$  discharge capacity, which correspond to 83 % of the initial capacity available in cathode. The capacity fade of these cells during cycling follows a linear trend, which is in agreement with what already reported for similar systems.<sup>74,75,76</sup> However, Graphite/LMNO cells show still 92% of the initial capacity after 100 cycles, which is a very good result in comparison with recent literature.<sup>75,76</sup> Graphite/LMNO cells reach the end of their cycling life (80 % of the initial capacity) after more than 300 cycles. This high cycling stability is in agreement with their high coulombic efficiencies. Namely, Graphite/LMNO cells reach 99 % coulombic efficiency after 10 cycles and the maximum value of 99.8 % after 50 cycles. This coulombic efficiency trend indicates an initial stabilization of the system and results in agreement with the film formation occurring on LMNO electrodes within the first 10 cycles (**Figure 44**). Additionally, the high coulombic efficiency values suggest reduced electrolyte decomposition rates and confirm the results shown in the *Chapter 4*.

The aging of these full cells was further investigated by impedance spectroscopy measurements. **Figure 55** reports the impedance spectra Graphite/LMNO cells (in the discharge state) recorded within the first 96 cycles. The obtained impedance spectra were fitted according to the equivalent circuit inserted in **Figure 55** and consisting in: an uncompensated resistance ( $R_0$ ), a semicircle capacitance ( $C_{SC}$ ), a semicircle resistance ( $R_{SC}$ ) and a Warburg-diffusion element ( $W$ ).

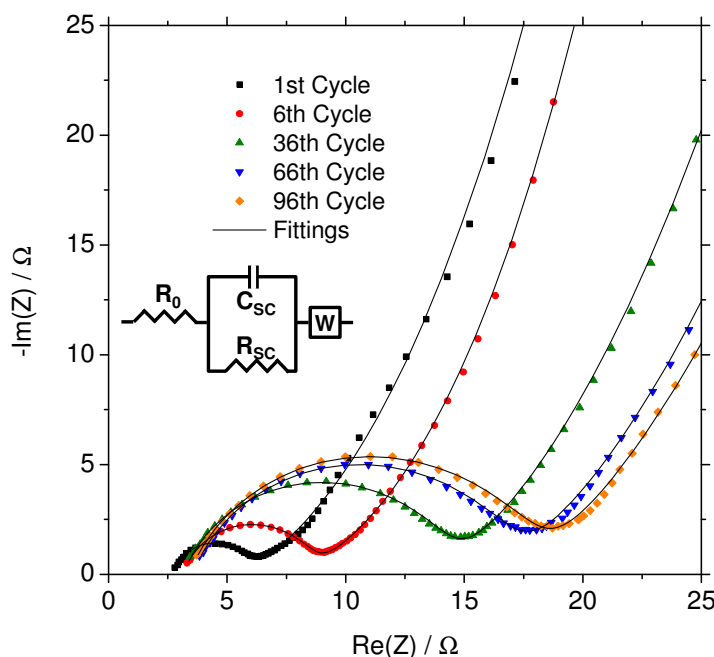


**Figure 55:** Impedance values and fittings for Graphite/LMNO cells in the discharged state. Reproduced in part with the permission from ChemSusChem. 2016, DOI: 10.1002/cssc.201600278. Copyright 2016 WILEY-VCH Verlag GmbH & Co. KGaA.<sup>88</sup> License Number: 3883560968998

All the impedance spectra of **Figure 55** present a single semicircle at high to medium frequencies is the result of both films and charge-transfer contribution. The significant enlargement of this semicircle during the first 36 cycles depends on a rapid increase of the  $R_{sc}$ , which indicates film thickening processes at the electrodes and increase of the charge-transfer resistances. Keeping cycling, the  $R_{sc}$  becomes gradually stable and reaches a value of ca. 14  $\Omega$  between the 66<sup>th</sup> and the 96<sup>th</sup> cycle. Unfortunately, it is not possible to estimate the exact contribution of the film resistances on the overall resistance. However, the trend of the  $R_{sc}$  along with the coulombic efficiency increase during the first cycles suggest stronger initial passivation of the electrodes, which guarantees reduced electrolyte decomposition rates and cell aging in the next cycles. Graphite/LMNO cells clearly point out the importance of the LMNO particle morphology in reducing the aging processes of full cells. However, the particle architecture alone is not sufficient to completely suppress the high voltage



effects, which still lead to charge consumption, films thickening and increase of charge transfer resistances.

As reported in *Chapter 6.1*, coating LMNO particles with  $\text{LiNbO}_3$  allows improving the stability of the active material/electrolyte interface and thus, further suppress the high-voltage cell aging of full cells. In order to evaluate the effects of the  $\text{LiNbO}_3$  coating, a second generation of full cells was assembled replacing the morphologically optimised LMNO with the coated LMNO-T. No other cell component or parameter were modified with respect to the first generation Graphite/LMNO cells.

**Figure 56** shows the potential profiles and the cycling stability of Graphite/LMNO-T cells.

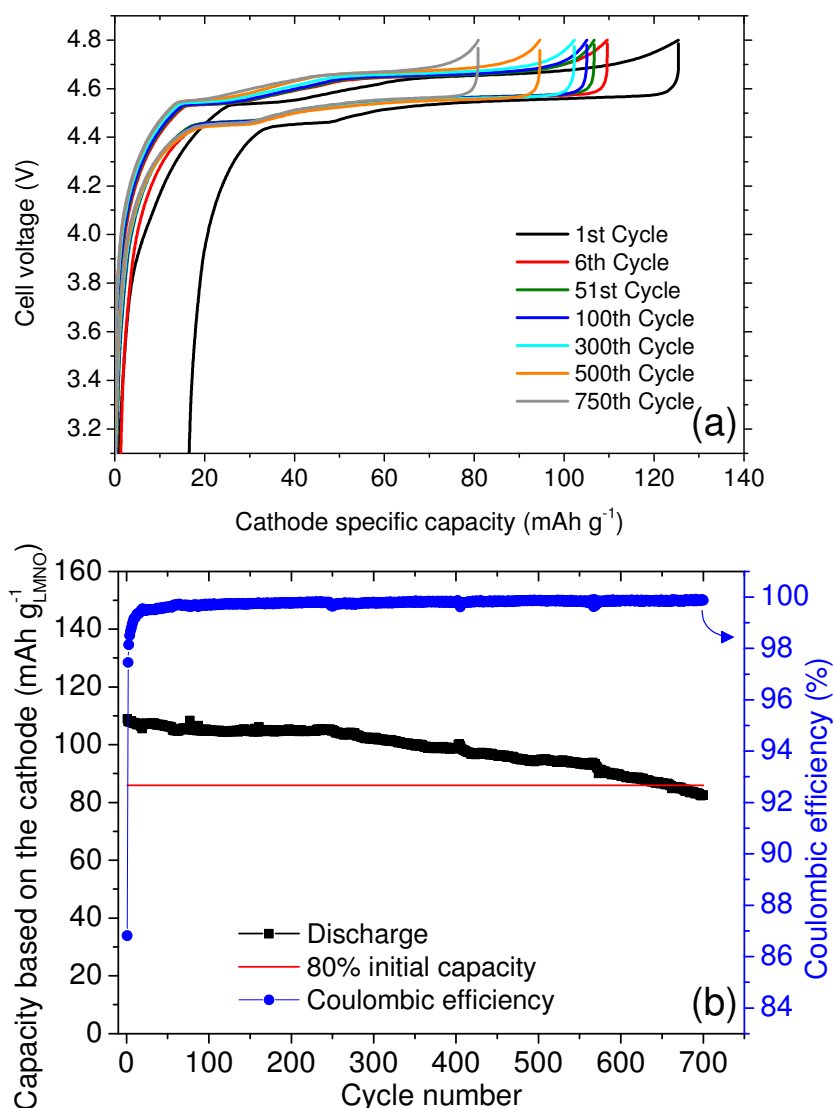


**Figure 56:** (a) Potential profiles and (b) cycling stability of a Graphite/LMNO-T full cell. Reproduced in part with the permission from ChemSusChem. 2016, DOI: 10.1002/cssc.201600278. Copyright 2016 WILEY-VCH Verlag GmbH & Co. KGaA.<sup>88</sup> License Number: 3883560968998

The potential profiles of Graphite/LMNO-T full cells present the same shape observed for Graphite/LMNO cells, with a charge and discharge voltage of 4.6 V and 4.5 V, respectively. The initial discharge capacity for Graphite/LMNO-T cells is again ca. 108 mAh g<sub>LMNO</sub><sup>-1</sup> but their cycling stability (**Figure 56b**) is twofold the cycling stability obtained with the uncoated LMNO as cathode material (**Figure 54b**). After 100 cycles, Graphite/LMNO-T cells still show 97 % of the initial capacity and they reach the end of the cycling life (80% of the initial

capacity) after more than 650 cycles. Also for these cells, the coulombic efficiency rapidly increases during the first 10 cycles and reaches a maximum value of 99.8% after ca. 50 cycles.

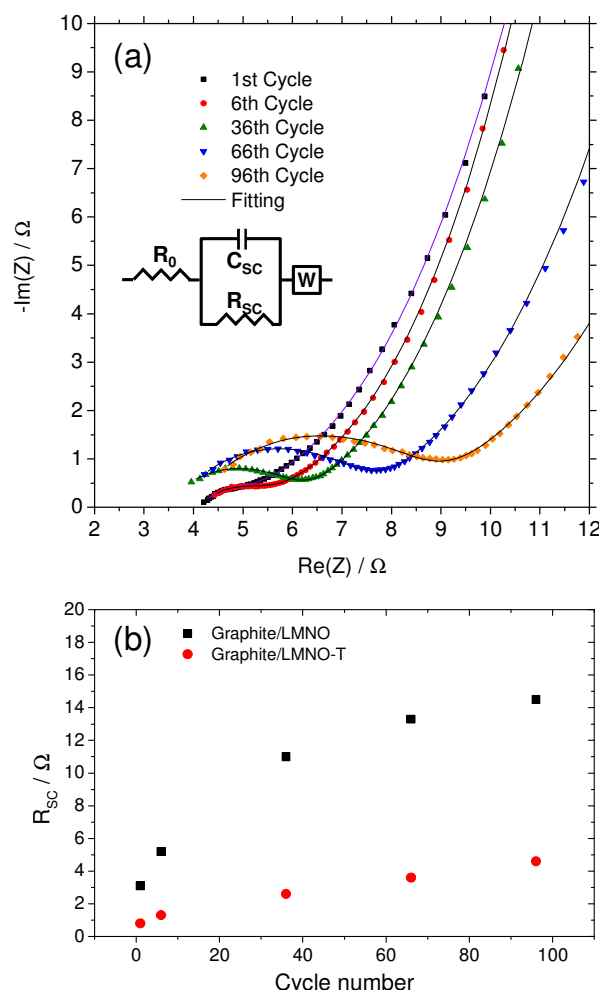


**Figure 57:** (a) impedance measurements and fittings for Graphite/LMNO-T cells; (b) comparison between the  $R_{sc}$  of Graphite/LMNO and Graphite/LMNO-T cells. Adapted and reproduced with the permission from ChemSusChem. 2016, DOI: 10.1002/cssc.201600278. Copyright 2016 WILEY-VCH Verlag GmbH & Co. KGaA.<sup>88</sup> License Number: 3883560968998

However, the different aging of Graphite-LMNO-T cells with respect to Graphite/LMNO cells clearly appears in the impedance measurements of **Figure 57**. In this case, the  $R_{sc}$  values for Graphite/LMNO-T cells are significantly lower than for Graphite/LMNO cells (**Figure 57b**) and suggest reduced aging related to charge transfer resistances increase, film formation and film

thickening. Since the only difference between Graphite/LMNO and Graphite/LMNO-T cells is the surface coating of LMNO-T, the reduced resistances and the superior cycling stability are only ascribable to  $\text{LiNbO}_3$ . The exact role of the  $\text{LiNbO}_3$  coating in full cells is not yet clear and its investigation requires a complete mechanistic study, which goes beyond the purpose of this work. Anyway, it is possible that the surface coating of LMNO-T leads to slightly different high voltage by-products and reduced transition metal dissolution with respect to the uncoated LMNO. The reported results confirm the key role of the selected particle architecture in the electrochemical performance and coulombic efficiency of full cells. Moreover, adopting LMNO-T as cathode material guarantees twofold cycling life and reduced aging with respect to the uncoated LMNO.

Different Li-ion batteries applications, such as portable electronics and mobile transport, require good performance and cycling stability in a wide range of temperature. Especially by operating at high temperature, Li-ion batteries undergo faster capacity fade due to faster deterioration kinetics of all the cell components. This deterioration is even more significant for high-voltage cells. In this case, the temperature significantly increases the electrolyte degradation rate and the transition metal dissolution process, which lead to fast cell death.<sup>71,72,73</sup> In order to have a complete overview on the investigated materials, the effects of the temperature on Graphite/LMNO and Graphite/LMNO-T cells were evaluated also at 45 °C.

**Figure 58** shows the potential profiles and the cycling stability of both Graphite/LMNO and Graphite/LMNO-T cells cycled at 45 °C (C/3 between 3.5 – 4.8 V).

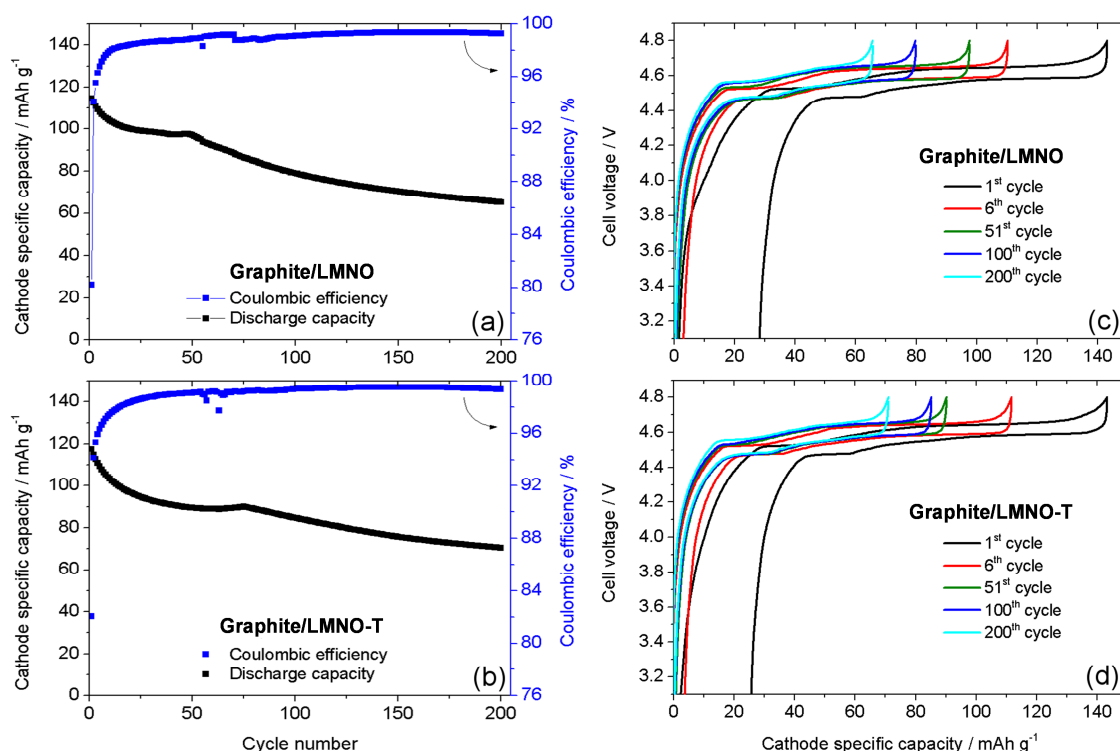


**Figure 58:** Potential profiles and cycling stability for (a), (b) Graphite/LMNO and (c), (d) Graphite/LMNO-T cells tested at 45 °C. Adapted and reproduced with the permission from ChemSusChem. 2016, DOI: 10.1002/cssc.201600278. Copyright 2016 WILEY-VCH Verlag GmbH & Co. KGaA.<sup>88</sup> License Number: 3883560968998

The reported results clearly show the effects of the higher temperature on cells performance. In comparison with the results obtained at RT (**Figure 54b** and **Figure 56b**), both Graphite/LMNO and Graphite/LMNO-T cells present significantly reduced cycling stability and ca. 60 % capacity retention after 200 cycles. Also the coulombic efficiency is affected by the higher temperature, suggesting higher electrolyte decomposition rate and a reduced stabilisation of the system during cycling.

In contrast to what observed at RT, adopting the coated LMNO-T as cathode material does not guarantee better cycling stability at 45 °C. The initial discharge capacity and the coulombic efficiency of Graphite/LMNO-T cells are slightly higher than for Graphite/LMNO-0 cells, but the capacity retention after 200 cycles is comparable. This similar behaviour for Graphite/LMNO-T and Graphite/LMNO cells is probably due to stronger effects of the degradation by-products, which frustrate the effects of the  $\text{LiNbO}_3$  coating.

## 7. SUMMARY

LMNO is a promising and cheap cathode material for Li-ion batteries operating at high potential vs.  $\text{Li/Li}^+$ . Increasing the cell voltage of Li-ion batteries guarantees higher energy density, which is the key for extending the driving of new electric vehicles. Unfortunately, LMNO operates above the stability window of standard organic electrolytes, giving rise to electrolyte decomposition issues and poor cell cycling life. Realising commercial LMNO-based batteries requires sensible reduction of the electrolyte decomposition and increase of the cell cycling stability.

In the first part of this work, a tailored LMNO was systematically studied with the purpose of obtaining the best electrochemical performance for full cell application. The morphology and the features of the active material strongly influence the electrochemical behaviour of LMNO-based cathodes operating in standard organic electrolyte. Thus, different fundamental aspects such as oxygen stoichiometry, particle morphology and crystallite size were separately modified and investigated in order to realise an optimised material. The second part of this work studied the role of particle morphology on the electrolyte degradation rates occurring at the surface of LMNO cathodes. Additionally, different charging methods were evaluated for obtaining the best electrodes performance at different C-rates. Finally, the morphologically optimised LMNO was investigated in full cell versus graphite anodes with and without an additional  $\text{LiNbO}_3$  surface coating. The effects of the optimised morphology and surface coating on the cell stability were separately studied and evaluated. All the collected results were of great relevance for optimising the high-voltage Graphite/LMNO Li-ion cells and pointed out key points for achieving higher cycling life in standard organic electrolyte.

The starting material studied in this work (LMNO-0) was a dense  $\text{LiNi}_{0.5}\text{Mn}_{1.5}\text{O}_4$  with spherical micro-particles made of a network of nano-crystallites densely connected with each other. The material showed a Li : Mn : Ni ratio of 1.0 : 1.5 : 0.5, and highly-ordered cubic structure described by the  $P4_332$  space group. Additionally, LMNO-0 presented high tap-density ( $2.26 \text{ g cm}^{-3}$ ), low surface area ( $< 1 \text{ m}^2 \text{ g}^{-1}$ ) and processability in line with commercial active materials for Li-ion batteries. The aim of the particle architecture was to obtain the best compromise between the high cycling stability typical for micrometric sized particles and the superior electrochemical performance of nano-structured materials. In this material, the low surface area was expected to minimise the active material/electrolyte interface and thus limit the electrolyte decomposition rate while, the network of nanometric crystallites was expected to guarantee good  $\text{Li}^+$  diffusion inside the particle. The pristine LMNO-0 presented exclusively the  $\text{Ni}^{2+}/\text{Ni}^{4+}$  electrochemical activity at ca. 4.7 V vs.  $\text{Li}/\text{Li}^+$  along with good discharge capacity ( $133 \text{ mAh g}^{-1}$  at C/5), good rate capability, high cycling stability and coulombic efficiency.

By performing an additional thermal treatment, it was possible to increase the crystallite size of LMNO-0 leaving unaltered all the other features. The material with bigger crystallite size (LMNO-T1) showed discharge capacities similar to the pristine LMNO-0 when cycled at lower C-rates. However, by increasing the C-rate, LMNO-T1 electrodes showed significant reduction of the rate capability and sudden capacity drop at 2C. The worsening of the rate capability is ascribable to slower delithiation/lithiation kinetics related to the longer  $\text{Li}^+$  diffusion paths inside the crystallites.

A second fundamental feature of LMNO is the oxygen stoichiometry. By performing suitable thermal treatments, it was possible to introduce different amounts of oxygen deficiencies in the LMNO-0 structure. The introduction of oxygen deficiencies in the pristine spinel led to changes in the oxidation state of Mn according to the formula  $\text{Li}[\text{Ni(II)}_{0.5}\text{Mn(III)}_{2\delta}\text{Mn(IV)}_{1.5-2\delta}]\text{O}_{4-\delta}$ . Additionally, the oxygen-deficient materials assumed partially disordered structure described by the  $Fd-3m$  space group and characterised by larger cell parameter. These

structural changes strongly affected the electrochemical behaviour of LMNO electrodes and led to significant changes in the voltage profiles, discharge capacities and rate capabilities. The potential profiles of oxygen-deficient materials showed an additional plateau at ca. 4 V vs. Li/Li<sup>+</sup>, which corresponds to the electrochemical activity of Mn<sup>3+</sup>. Because of this additional plateau, oxygen-deficient materials presented part of their electrochemical activity also at lower potential and thus, reduced high-voltage behaviour with respect to stoichiometric LMNO. Furthermore, oxygen deficient materials had lower discharge capacities than LMNO-0, probably because of the inactive rock-salt impurities formed during the secondary thermal treatments. The rate capabilities observed for the oxygen-deficient materials and for the pristine LMNO-0 were comparable up to 3C, and then LMNO-0 electrodes showed a sudden capacity drop down. Further investigations and data analyses pointed out a possible explanation for this phenomenon. At the very beginning of the charging process, LMNO-0 electrodes show a steep potential increase, which reaches a maximum value and then decreases down to a lower stable value (the potential of the first plateau). This initial potential peak is higher for higher charging rates and when it reaches the upper charging cut-off (4.9 V vs. Li/Li<sup>+</sup> for LMNO electrodes), the charge stops without any significant electrodes delithiation. Impedance measurements on both stoichiometric and oxygen-deficient materials helped understanding the origin of this initial potential peak. Electrodes with the stoichiometric material showed higher resistances in the lithiated state than in the delithiated state. This suggests that the lithiated LMNO phase presents slower kinetics with respect to the delithiated one, leading to the potential peak at the beginning of the charge process. The oxygen-deficient materials did not show significant differences between the lithiated and the delithiated status. Thus, they presented neither an initial potential peak nor a sudden capacity drop-down by increasing the charging rate.

Another morphological feature studied for LMNO-0 is the particle dimension. The pristine sample was sieved in four batches with different particle dimensions: < 20  $\mu\text{m}$  (LMNO-XS), 20 – 25  $\mu\text{m}$  (LMNO-S), 25 – 32  $\mu\text{m}$



(LMNO-M) and 32 – 40  $\mu\text{m}$  (LMNO-L). Electrodes from these batches were investigated in half-cells in order to point out the effect of the particle dimension on the electrochemical performance. Adopting smaller particles (LMNO-XS) guaranteed better rate capabilities with respect to bigger particle, probably because of the shorter Li diffusion path between bulk and surface. However, also the wider particle distribution of LMNO-0 led to comparable rate capabilities. This is probably due to better packing of the powders obtained when smaller particles fill the gaps between bigger particles. This way, LMNO-0 presents more inter-particle contacts, which are beneficial for the conductivity. Since smaller particles lead to increased active material/electrolyte interface, using broader particle size distribution is the best compromise between cycling stability and electrochemical performance. According to the obtained results, the material of choice for further investigations was the stoichiometric LMNO-0 with small crystallite size and wide particle size distribution.

The relation between particle morphology and electrolyte degradation was studied by comparing the optimized LMNO-0 with a commercial nano-sized material with no specific particle architecture (LMNO-R). LMNO-0 and LMNO-R presented comparable crystallite size, but the morphology of LMNO-R resulted in lower tap density ( $0.67 \text{ g cm}^{-3}$ ) and higher surface area ( $18 \text{ m}^2 \text{ g}^{-1}$ ). LMNO-0 and LMNO-R electrodes were electrochemically investigated outside and inside the operating potential window of LMNO (3.5 – 4.9 V vs.  $\text{Li/Li}^+$ ) in order to identify the onset potential and the rate of the electrolyte decomposition reactions in a wide potential range. These electrochemical tests suggested that both LMNO-0 and LMNO-R electrodes lead to the same nature of the electrolyte degradation processes, which probably do not depend on the morphology but only on the surface chemistry of the material. On the other hand, the morphology of the active material strongly influences the electrolyte degradation rate, which result ca. 5 times higher for LMNO-R electrodes than for LMNO-0 electrodes. The lower electrolyte decomposition rate on LMNO-0 electrodes reduces also the growth of passivation films on the electrodes surface and their resistances during cycling. These results confirm that the selected particle architecture allows

obtaining a good compromise between high electrochemical performances and low electrolyte degradation.

The electrolyte degradation on LMNO-0 electrodes occurs mainly above the operating potential (ca. 4.7 V vs. Li/Li<sup>+</sup>) and thus, it is very important to charge these cathodes keeping the upper potential cut-off as close as possible to the operating potential. Two different charging procedures allowed obtaining both high coulombic efficiency and complete charge of LMNO-0 electrodes. At slower charging rates (< 1C), LMNO-0 electrodes presented the best performance when galvanostatically charged up to 4.9 V vs. Li/Li<sup>+</sup>, while at faster charging rates (≥ 1C) it was necessary to apply a short potentiostatic step after the galvanostatic charge. This second charging procedure allowed also reducing the upper cut-off down to 4.8 V vs. Li/Li<sup>+</sup>.

Surface treatments of the cathode active material are also a valid method to further improve the stability of the electrode-electrolyte interface and limit the electrolyte degradation. According to literature, LiNbO<sub>3</sub> is a good candidate as coating material for LMNO and should guarantee better electrode-electrolyte interface without compromising the electrochemical performance of the pristine material. The LiNbO<sub>3</sub> surface treatment of morphologically optimised LMNO was performed with an easy and low-temperature method, which allowed obtaining thin and homogeneous coating on the surface of the particles. The LiNbO<sub>3</sub> coating did not alter the remarkable electrochemical performance of the morphologically optimised LMNO.

Both the uncoated and the coated LMNO were tested as cathode materials in full Li-ion cells versus graphite anodes. The balancing of the assembled full cells took in consideration key aspects for Li-ion cells such as electrodes loadings, electrochemical performance and safety. The aim of these tests was to individually evaluate the role of the particle architecture and the beneficial effects of the LiNbO<sub>3</sub> coating on the cycling stability of full cells.

Full cells assembled with the morphologically optimised LMNO (Graphite/LMNO cells) showed high coulombic efficiency up to 99.8 % and initial discharge capacity of ca. 108 mAh g<sup>-1</sup> (based on the weight of LMNO in

the cathode). After more than 300 cycles, these cells still presented 80 % of the initial capacity, which is a good result for high-voltage systems. Impedance measurements on these cells showed an increase of the surface resistances during cycling, especially within the first 10 cycles. This increase suggests the progressive stabilization of the system, which is partly ascribable to surface passivation of the electrodes. Full cells adopting  $\text{LiNbO}_3$ -coated LMNO as cathode material (Graphite/LMNO-T cell) showed initial capacity and coulombic efficiency similar to Graphite/LMNO cells but twofold cycling stability (80% capacity retention after more than 650 cycles). Impedance spectra performed on these cells showed much lower and more stable surface resistance values with respect to Graphite/LMNO cells and thus, reduced aging during cycling. The exact mechanism related to this lower aging requires further investigation. However, it is plausible that the  $\text{LiNbO}_3$  coating leads to slightly different electrolyte by-products and lower Mn dissolution with respect to the uncoated LMNO particle surface.

Graphite/LMNO and Graphite/LMNO-T cells were also tested at 45 °C. Working at high temperature significantly increases the high-voltage aging phenomenon and drastically reduces the cycling life. Nevertheless, the tested cells showed a coulombic efficiency above 99 % and ca. 60 % of the initial capacity after 200 cycles. In the case of high temperature tests, Graphite/LMNO-T cells presented electrochemical behaviour comparable with Graphite/LMNO cells, probably because of significantly stronger effects of the degradation by-products at 45°C.

In conclusion, this work investigated different key issues for realising high-voltage Li-ion cells, such as optimisation of the active material, onset and rate of the electrolyte high-voltage decomposition, effective charging procedures for the LMNO cathodes and improvement of full cells cycling stability. The reported results are useful for improving the performance and the stability of high-voltage Li-ion batteries. However, these systems still require further studies and optimisations in order to become the next generation of Li-Ion batteries.



# Bibliography

---

<sup>1</sup> IEA (2014), "A framework for our energy future", in IEA, World Energy Outlook 2014, IEA. DOI: 10.1787/weo-2014-3-en. <http://dx.doi.org/10.1787/weo-2014-3-en>.

<sup>2</sup> K.E. Aifantis, S.A. Hackney, R.V. Kumar. High Energy Density Lithium Batteries, Materials, Engineering, Applications. Wiley-VCH, Weinheim, Germany, (2010).

<sup>3</sup> J.-M. Tarascon, M. Armand. Issues and challenges facing rechargeable lithium batteries. *Nature*, 414, 359, (2001).

<sup>4</sup> B. Scrosati, J. Hassounab, Y.-K. Sun. Lithium-ion batteries. A look into the future. *Energy Environ. Sci.*, 4, 3287, (2011).

<sup>5</sup> R. A. Huggins. Advanced Batteries, Materials Science Aspects. Springer Science+Business Media, New York, United States, (2009).

<sup>6</sup> D. Linden, T.B.Reddy. Handbook of Batteries, Third Edition. The McGraw-Hill Company, New York, United States, (2001).

<sup>7</sup> M. S. Whittingham. Electrical Energy Storage and Intercalation Chemistry. *Science*, 192, 1126 (1976).

<sup>8</sup> M. S. Whittingham. The Role of Ternary Phases in Cathode Reactions. *J. Electrochem. Soc.*, 123, 315 (1976)

- 
- <sup>9</sup> K.M. Abraham, D.M. Pasquariello, F.J. Martin. Mixed Ether Electrolytes for Secondary Lithium Batteries with Improved Low Temperature Performance. *J. Electrochem. Soc.*, 133, 661 (1986).
- <sup>10</sup> M. Lazzari, B. Scrosati. A Cyclable Lithium Organic Electrolyte Cell Based on Two Intercalation Electrodes. *J. Electrochem. Soc.*, 127, 773, (1980).
- <sup>11</sup> B. Di Pietro, M. Patriarca, B. Scrosati. On the use of rocking chair configurations for cyclable lithium organic electrolyte batteries. *J. Power Sources*, 8, 298, (1982).
- <sup>12</sup> B. Scrosati. Lithium rocking chair batteries: An old concept? History of rocking chair batteries. *J. Electrochem. Soc.*, 139, 2776, (1992).
- <sup>13</sup> C.K. Dyer, P.T. Moseley, Z. Ogumi, D.A.J. Rand, B. Scrosati. Encyclopedia of Electrochemical Power Sources. Elsevier B.V., Amsterdam, The Netherlands (2009)
- <sup>14</sup> V. Muenzel, A.F. Hollenkamp, A.I. Bhatt, J. de Hoog, M. Brazil, D.A. Thomas, I. Mareels. A Comparative Testing Study of Commercial 18650-Format Lithium-Ion Battery Cells. *J. Electrochem. Soc.*, 162, A1592, (2015).
- <sup>15</sup> T. Ohzuku, A. Ueda, N. Yamamota. Zero-Strain Insertion Material of  $\text{Li}[\text{Li}_{1/3}\text{Ti}_{5/3}]\text{O}_4$  for Rechargeable Lithium Cells. *J. Electrochem. Soc.*, 142, 1431, (1995).
- <sup>16</sup> H.-G. Jung, M. W. Jang, J. Hassoun, Y.-K. Sun, B. Scrosati. A high-rate long-life  $\text{Li}_4\text{Ti}_5\text{O}_{12}/\text{Li}[\text{Ni}_{0.45}\text{Co}_{0.1}\text{Mn}_{1.45}]\text{O}_4$  lithium-ion battery. *Nat. Commun.* 2, 516, (2011).

- 
- <sup>17</sup> C. Wang, S. Wang, Y.-B. He, L. Tang, C. Han, C. Yang, M. Wagemaker, B. Li, Q.-H. Yang, J.-K. Kim, F. Kang. Combining Fast Li-Ion Battery Cycling with Large Volumetric Energy Density: Grain Boundary Induced High Electronic and Ionic Conductivity in  $\text{Li}_4\text{Ti}_5\text{O}_{12}$  Spheres of Densely Packed Nanocrystallites. *Chem. Mater.*, 27, 5647, (2015).
- <sup>18</sup> X. Xiao , W. Zhou , Y. Kim , I. Ryu , M. Gu , C. Wang , G. Liu , Z. Liu , H. Gao. Regulated Breathing Effect of Silicon Negative Electrode for Dramatically Enhanced Performance of Li-Ion Battery. *Adv. Funct. Mater.*, 25, 1426, (2015).
- <sup>19</sup> Y. Xu , Y. Zhu , F. Han , C. Luo , C. Wang. 3D Si/C Fiber Paper Electrodes Fabricated using a Combined Electrospray/Electrospinning Technique for Li-Ion Batteries. *Adv. Energy Mater.*, 5, 1400753, (2015).
- <sup>20</sup> X. Huang, S. Cui, J. Chang, P. B. Hallac, C. R. Fell, Y. Luo, B. Metz, J. Jiang, P. T. Hurley, J. Chen. A Hierarchical Tin/Carbon Composite as an Anode for Lithium-Ion Batteries with a Long Cycle Life. *Angew. Chem. Int. Ed.*, 54, 1490, (2015).
- <sup>21</sup> Q.-Y. Li, Q.-C. Pan, G.-H. Yang, X.-L. Lin, Z.-X. Yan, H.-Q. Wang, Y.-G. Huang. Synthesis of Sn/MoS<sub>2</sub>/C composites as high-performance anodes for lithium-ion batteries. *J. Mater. Chem. A*, 3, 20375, (2015).
- <sup>22</sup> L.-X. Yuan, Z.-H. Wang, W.-X. Zhang, X.-L. Hu, J.-T. Chen, Y.-H. Huang, J. B. Goodenough. Development and challenges of  $\text{LiFePO}_4$  cathode material for lithium-ion batteries. *Energy Environ. Sci.*, 4, 269, (2011).
- <sup>23</sup> C. M. Julien, A. Mauger, K. Zaghib, H. Groult. Comparative Issues of Cathode Materials for Li-Ion Batteries. *Inorganics*, 2, 132 (2014).

- 
- <sup>24</sup> S.-T. Myung, K. Amine, Y.-K. Sun. Nanostructured cathode materials for rechargeable lithium batteries. *J. Power Sources*, 283, 219, (2015).
- <sup>25</sup> Y. Tang, Y. Zhang, W. Li, B. Ma, X. Chen. Rational material design for ultrafast rechargeable lithium-ion batteries. *Chem. Soc. Rev.*, 44, 5926, (2015).
- <sup>26</sup> K. Mizushima, P.C. Jones, P.J. Wiseman, J.B. Goodenough.  $\text{Li}_x\text{CoO}_2$  ( $0 < x < 1$ ): A new cathode material for batteries of high energy density. *Mater. Res. Bull.*, 15, 783 (1980).
- <sup>27</sup> J.R. Dahn. Structure and electrochemistry of  $\text{Li}_{1\pm y}\text{NiO}_2$  and a new  $\text{Li}_2\text{NiO}_2$  phase with the  $\text{Ni}(\text{OH})_2$  structure. *Solid State Ionics*, 44, 87, (1990).
- <sup>28</sup> G. G. Amatucci, J. M. Tarascon, L. C. Klein.  $\text{CoO}_2$ , The End Member of the  $\text{LiCoO}_2$  Solid Solution. *J. Electrochem. Soc.*, 143, 1114 (1996).
- <sup>29</sup> R. J. Gummow, D. C. Liles, M. M. Thackeray. Lithium extraction from orthorhombic lithium manganese oxide and the phase transformation to spinel. *Mater. Res. Bull.*, 28, 1249 (1993).
- <sup>30</sup> R. J. Gummow, M. M. Thackeray. An Investigation of Spinel-Related and Orthorhombic  $\text{LiMnO}_2$  Cathodes for Rechargeable Lithium Batteries. *J. Electrochem. Soc.*, 141, 1178 (1994).
- <sup>31</sup> M. M. Thackeray, S.-H. Kang, C. S. Johnson, J. T. Vaughey, R. Benedeka, S. A. Hackney.  $\text{Li}_2\text{MnO}_3$ -stabilized  $\text{LiMO}_2$  ( $\text{M} = \text{Mn, Ni, Co}$ ) electrodes for lithium-ion batteries. *J. Mater. Chem.*, 17, 3112, (2007).



- 
- <sup>32</sup> C. S. Johnson, N. Li, C. Lefief, M. M. Thackeray. Anomalous capacity and cycling stability of  $x\text{Li}_2\text{MnO}_3 \cdot (1 - x)\text{LiMO}_2$  electrodes (M = Mn, Ni, Co) in lithium batteries at 50 °C. *Electrochem. Commun.*, 9, 787, (2007).
- <sup>33</sup> T. Ohzuku, M. Nagayama, K. Tsuji, K. Ariyoshi. High-capacity lithium insertion materials of lithium nickel manganese oxides for advanced lithium-ion batteries: toward rechargeable capacity more than 300 mAh g<sup>-1</sup>. *J. Mater. Chem.*, 21, 10179, (2011).
- <sup>34</sup> S. Rajarathinam, S. Mitra, R. K. Petla.  $\text{Li}_2\text{MnO}_3$  rich- $\text{LiMn}_{0.33}\text{Co}_{0.33}\text{Ni}_{0.33}\text{O}_2$  integrated nano-composites as high energy density lithium-ion battery cathode materials. *Electrochim. Acta*, 108, 135, (2013).
- <sup>35</sup> C. Cao, L. Xi, K. L. Leung, M. Wang, Y. Liu, R. Ma, S. Yang, Z. Lu, C. Y. Chung. Facile synthesis of porous Li-rich layered  $\text{Li}[\text{Li}_{0.2}\text{Mn}_{0.534}\text{Ni}_{0.133}\text{Co}_{0.133}]\text{O}_2$  as high- performance cathode materials for Li-ion batteries. *RSC Adv.*, 5, 30507, (2015).
- <sup>36</sup> A. R. Armstrong, M. Holzapfel, P Novák, C. S. Johnson, S.-H. Kang, M. M. Thackeray, P. G. Bruce. Demonstrating Oxygen Loss and Associated Structural Reorganization in the Lithium Battery Cathode  $\text{Li}[\text{Ni}_{0.2}\text{Li}_{0.2}\text{Mn}_{0.6}]\text{O}_2$ . *J. Am. Chem. Soc.*, 128, 8694, (2006).
- <sup>37</sup> J. R. Croy, K. G. Gallagher, M. Balasubramanian, B. R. Long, M. M. Thackeray. Quantifying Hysteresis and Voltage Fade in  $x\text{Li}_2\text{MnO}_3 \bullet (1-x)\text{LiMn}_{0.5}\text{Ni}_{0.5}\text{O}_2$  Electrodes as a Function of  $\text{Li}_2\text{MnO}_3$  Content. *J. Electrochem. Soc.*, 161, A318, (2014).

- 
- <sup>38</sup> F. Dogan, J. R. Croy, M. Balasubramanian, M. D. Slater, H. Iddir, C. S. Johnson, J. T. Vaughey, B. Key. Solid State NMR Studies of  $\text{Li}_2\text{MnO}_3$  and Li-Rich Cathode Materials: Proton Insertion, Local Structure, and Voltage Fade. *J. Electrochem. Soc.*, 162, A235, (2015).
- <sup>39</sup> E. Lee, J. S. Park, T. Wu, C.-J. Sun, H. Kim, P. C. Stair, J. Lu, D. Zhouad, C. S. Johnson. Role of  $\text{Cr}^{3+}/\text{Cr}^{6+}$  redox in chromium-substituted  $\text{Li}_2\text{MnO}_3\cdot\text{LiNi}_{1/2}\text{Mn}_{1/2}\text{O}_2$  layered composite cathodes: electrochemistry and voltage fade. *J. Mater. Chem. A*, 3, 9915, (2015).
- <sup>40</sup> C. M. Julien, A. Mauger, K. Zaghib, D. Liu. Rechargeable Batteries, Materials, Technologies and New Trends. Springer International Publishing, Switzerland, pp. 477-509, (2015).
- <sup>41</sup> G. Kumar, H. Schlorb, D. Rahner. Synthesis and electrochemical characterization of 4 V  $\text{LiR}_x\text{Mn}_{2-x}\text{O}_4$  spinels for rechargeable lithium batteries. *Mater. Chem. Phys.*, 70, 117 (2001).
- <sup>42</sup> G. T.-K. Fey, C.-Z. Lu, T. P. Kumar. Solid-state synthesis and electrochemical characterization of  $\text{LiM}_y\text{Cr}_{0.5-y}\text{Mn}_{1.5}\text{O}_4$  ( $\text{M} = \text{Fe}$  or  $\text{Al}$ ;  $0.0 < y < 0.4$ ) spinels. *Mater. Chem. Phys.*, 80, 309 (2003).
- <sup>43</sup> I. Taniguchi, Powder properties of partially substituted  $\text{LiM}_x\text{Mn}_{2-x}\text{O}_4$  ( $\text{M} = \text{Al}$ ,  $\text{Cr}$ ,  $\text{Fe}$  and  $\text{Co}$ ) synthesized by ultrasonic spray pyrolysis. *Mater. Chem. Phys.*, 92, 172 (2005).
- <sup>44</sup> A. Kraytsberg, Y. Ein-Eli. Higher, Stronger, Better ... A Review of 5 Volt Cathode Materials for Advanced Lithium-Ion Batteries. *Adv. Energy Mater.*, 2, 922, (2012).

- 
- <sup>45</sup> Q. Zhong, A. Bonakclarpour, M. Zhang, Y. Gao, J.R. Dahn. Synthesis and Electrochemistry of  $\text{LiNi}_x\text{Mn}_{2-x}\text{O}_4$ . *J. Electrochem. Soc.*, 144, 205 (1997).
- <sup>46</sup> H.-S. Fang, Z.-X. Wang, X.-H. Li, H.-J. Guo, W.-J. Peng. Exploration of high capacity  $\text{LiNi}_{0.5}\text{Mn}_{1.5}\text{O}_4$  synthesized by solid-state reaction. *J. Power Sources*, 153, 174 (2006).
- <sup>47</sup> Y. Fan, J. Wang, X. Ye, J. Zhang. Physical properties and electrochemical performance of  $\text{LiNi}_{0.5}\text{Mn}_{1.5}\text{O}_4$  cathode material prepared by a coprecipitation method. *Mater. Chem. Phys.*, 103, 19 (2007).
- <sup>48</sup> X. Zhang, F. Cheng, K. Zhang, Y. Liang, S. Yang, J. Liang, J. Chen. Facile polymer-assisted synthesis of  $\text{LiNi}_{0.5}\text{Mn}_{1.5}\text{O}_4$  with a hierarchical micro–nano structure and high rate capability. *RSC Advances*, 2, 5669, (2012).
- <sup>49</sup> H. B. Lin, Y. M. Zhang, H. B. Rong, S. W. Mai, J. N. Hu, Y. H. Liao, L. D. Xing, M. Q. Xu, X. P. Li, W. S. Li. Crystallographic facet- and size-controllable synthesis of spinel  $\text{LiNi}_{0.5}\text{Mn}_{1.5}\text{O}_4$  with excellent cyclic stability as cathode of high voltage lithium ion battery. *J. Mater. Chem. A*, 2, 11987, (2014).
- <sup>50</sup> G. Ma, Y. Zhang, J. Lin, Z. Chen, R. Zhao, P. Tong, L. Zou, H. Chen. Synthesis of high-voltage spinel  $\text{LiNi}_{0.5}\text{Mn}_{1.5}\text{O}_4$  material for lithium-ion batteries by a metal-cholate supramolecular hydrogel as precursor. *J. Solid State Electrochem.*, DOI 10.1007/s10008-015-2962-0, (2015).
- <sup>51</sup> Y. Idemoto, H. Narai, N. Koura. Crystal structure and cathode performance dependence on oxygen content of  $\text{LiMn}_{1.5}\text{Ni}_{0.5}\text{O}_4$  as a cathode material for secondary lithium batteries. *J. Power Sources*, 119, 125, (2003).

- 
- <sup>52</sup> B.J. Hwang, Y.W. Wu, M. Venkateswarlu, M.Y. Cheng, R. Santhanam. Influence of synthesis conditions on electrochemical properties of high-voltage  $\text{Li}_{1.02}\text{Ni}_{0.5}\text{Mn}_{1.5}\text{O}_4$  spinel cathode material. *J. Power Sources*, 193, 828, (2009).
- <sup>53</sup> J.-H. Kim, S.-T. Myung, C. S. Yoon, S. G. Kang, Y.-K. Sun. Comparative Study of  $\text{LiNi}_{0.5}\text{Mn}_{1.5}\text{O}_{4-\delta}$  and  $\text{LiNi}_{0.5}\text{Mn}_{1.5}\text{O}_4$  Cathodes Having Two Crystallographic Structures:  $Fd-3m$  and  $P4_332$ . *Chem. Mater.*, 16, 906, (2004).
- <sup>54</sup> J.-H. Kim, C. S. Yoon, S.-T. Myung, Jai Prakash, Y.-K. Sun. Phase Transitions in  $\text{Li}_{1-\delta}\text{Ni}_{0.5}\text{Mn}_{1.5}\text{O}_4$  during Cycling at 5 V. *Electrochem. Solid St.*, 7, A216, (2004).
- <sup>55</sup> A. Manthiram, K. Chemelewski, E.-S. Lee. A perspective on the high-voltage  $\text{LiMn}_{1.5}\text{Ni}_{0.5}\text{O}_4$  spinel cathode for lithium-ion batteries. *Energy Environ. Sci.*, 7, 1339 (2014).
- <sup>56</sup> A. Du Pasquier, A. Blyr, P.Courjal, D. Larcher, G. Amatucci, B. Gérard, J.-M. Tarascon. . Mechanism for Limited 55°C Storage Performance of  $\text{Li}_{1.05}\text{Mn}_{1.95}\text{O}_4$  Electrodes. *J. Electrochem. Soc.*, 146, 428, (1999).
- <sup>57</sup> D. H. Jang, S. M. Oh. Electrolyte Effects on Spinel Dissolution and Cathodic Capacity Losses in 4 V  $\text{Li}/\text{Li}_x\text{Mn}_2\text{O}_4$  Rechargeable Cells. *J. Electrochem. Soc.*, 144, 3342, (1997).
- <sup>58</sup> D. Jang, Y. Shin, S. Oh. Dissolution of Spinel Oxides and Capacity Losses in 4 V  $\text{Li}/\text{Li}_x\text{Mn}_2\text{O}_4$  Cells. *J. Electrochem. Soc.*, 143, 2204, (1996).
- <sup>59</sup> Y. Xia, Y.Zhou, M. Yoshio. Capacity Fading on Cycling of 4 V  $\text{Li}/\text{LiMn}_2\text{O}_4$  Cells. *J. Electrochem. Soc.*, 144, 4, (1997).

- 
- <sup>60</sup> T. Aoshima, K. Okahara, C. Kiyohara, K. Shizuka. Mechanisms of manganese spinels dissolution and capacity fade at high temperature. *J. Power Sources*, 97, 377, (2001).
- <sup>61</sup> L. Yang, M. Takahashi, B. Wang. A study on capacity fading of lithium-ion battery with manganese spinel positive electrode during cycling. *Electrochim. Acta*, 51, 3228, (2006).
- <sup>62</sup> M. Kunduraci, G.G. Amatucci. The effect of particle size and morphology on the rate capability of 4.7V  $\text{LiMn}_{1.5+\delta}\text{Ni}_{0.5-\delta}\text{O}_4$  spinel lithium-ion battery cathodes. *Electrochim. Acta*, 53, 4193, (2008).
- <sup>63</sup> M. Kunduraci, J.F. Al-Sharab, G.G. Amatucci. High-Power Nanostructured  $\text{LiMn}_{2-x}\text{Ni}_x\text{O}_4$  High-Voltage Lithium-Ion Battery Electrode Materials: Electrochemical Impact of Electronic Conductivity and Morphology. *Chem. Mater.*, 18, 3585, (2006).
- <sup>64</sup> J. Xiao, X. Chen, P. V. Sushko, M. L. Sushko, L. Kovarik, J. Feng, Z. Deng, J. Zheng, G. L. Graff, Z. Nie, D. Choi, J. Liu, J.-G. Zhang, M. S. Whittingham. High-performance  $\text{LiNi}_{0.5}\text{Mn}_{1.5}\text{O}_4$  spinel controlled by  $\text{Mn}^{3+}$  concentration and site disorder. *Adv. Mater.*, 24, 2109, (2012).
- <sup>65</sup> W. Xu, X. Chen, F. Ding, J. Xiao, D. Wang, A. Pan, J. Zheng, X.S. Li, A.B. Padmaperuma, J.-G. Zhang. Reinvestigation on the state-of-the-art nonaqueous carbonate electrolytes for 5 V Li-ion battery applications. *J. Power Sources*, 213, 304 (2012).
- <sup>66</sup> L. Yang, B. Ravdel, B.L. Lucht. Electrolyte Reactions with the Surface of High Voltage  $\text{LiNi}_{0.5}\text{Mn}_{1.5}\text{O}_4$  Cathodes for Lithium-Ion Batteries. *Electrochem. Solid St.*, 13, A95 (2010).

- 
- <sup>67</sup> H. Duncan, Y. Abu-Lebdeh, I. J. Davidson. Study of the Cathode–Electrolyte Interface of  $\text{LiMn}_{1.5}\text{Ni}_{0.5}\text{O}_4$  Synthesized by a Sol–Gel Method for Li-Ion Batteries. *J. Electrochem. Soc.*, 157, A528 (2010).
- <sup>68</sup> S.-Y. Ha, J.-G. Han, Y.-M. Song, M.-J. Chun, S.-I. Han, W.-C. Shin, N.-S. Choi. Using a lithium bis(oxalato) borate additive to improve electrochemical performance of high-voltage spinel  $\text{LiNi}_{0.5}\text{Mn}_{1.5}\text{O}_4$  cathodes at 60°C. *Electrochim. Acta*, 104, 170 (2013).
- <sup>69</sup> A. Jarry, S. Gottis, Y.-S. Y, J. Roque-Rosell, C. Kim, J. Cabana, J. Kerr, R. Kostecki. The Formation Mechanism of Fluorescent Metal Complexes at the  $\text{Li}_x\text{Ni}_{0.5}\text{Mn}_{1.5}\text{O}_{4-\delta}$ /Carbonate Ester Electrolyte Interface. *J. Am. Chem. Soc.*, 137, 3533 (2015).
- <sup>70</sup> D. Aurbach, B. Markovsky, Y. Talyossef, G. Salitra, H.-J. Kim, S. Choi. Studies of cycling behavior, ageing, and interfacial reactions of  $\text{LiNi}_{0.5}\text{Mn}_{1.5}\text{O}_4$  and carbon electrodes for lithium-ion 5-V cells. *J. Power Sources*, 162, 780, (2006).
- <sup>71</sup> S. Patoux, L. Sannier, H. Lignier, Y. Reynier, C. Bourbon, S. Jouanneau, F. Le Cras, S. Martinet. High voltage nickel manganese spinel oxides for Li-ion batteries. *Electrochim. Acta*, 53, 4137, (2008).
- <sup>72</sup> N. P. W. Pieczonka, Z. Liu, P. Lu, K. L. Olson, J. Moote, B. R. Powell, J.-H. Kim. Understanding Transition-Metal Dissolution Behavior in  $\text{LiNi}_{0.5}\text{Mn}_{1.5}\text{O}_4$  High-Voltage Spinel for Lithium Ion Batteries. *J. Phys. Chem. C*, 117, 15947, (2013).

- 
- <sup>73</sup> D. Lu, M. Xu, L. Zhou, A. Garsuch, B. L. Lucht. Failure Mechanism of Graphite/LiNi<sub>0.5</sub>Mn<sub>1.5</sub>O<sub>4</sub> Cells at High Voltage and Elevated Temperature. *J. Electrochem. Soc.*, 160, A3138, (2013).
- <sup>74</sup> J.-H. Kim, N. P.W. Pieczonka, Z. Li, Y. Wu, S. Harris, B. R. Powell. Understanding the capacity fading mechanism in LiNi<sub>0.5</sub>Mn<sub>1.5</sub>O<sub>4</sub>/graphite Li-ion batteries. *Electrochim. Acta*, 90, 556, (2013).
- <sup>75</sup> J.-H. Kim, N. P. W. Pieczonka, P. Lu, Z. Liu, R. Qiao, W. Yang, M. M. Tessema, Y.-K. Sun, B. R. Powell. In Situ Formation of a Cathode–Electrolyte Interface with Enhanced Stability by Titanium Substitution for High Voltage Spinel Lithium-Ion Batteries. *Adv. Mater. Interfaces*, 2, 1500109, (2015).
- <sup>76</sup> J.-C. Fang, Y.-F. Xu, G.-L. Xu, S.-Y. Shen, J.-T. Li, L. Huang, S.-G. Sun. Fabrication of densely packed LiNi<sub>0.5</sub>Mn<sub>1.5</sub>O<sub>4</sub> cathode material with excellent long-term cycleability for high-voltage lithium ion batteries. *J. Power Sources*, 304, 15, (2016).
- <sup>77</sup> Y. Kobayashi, H. Miyashiro, K. Takei, H. Shigemura, M. Tabuchi, H. Kageyama, T. Iwahori. 5 V Class All-Solid-State Composite Lithium Battery with Li<sub>3</sub>PO<sub>4</sub> Coated LiNi<sub>0.5</sub>Mn<sub>1.5</sub>O<sub>4</sub>. *J. Electrochem. Soc.*, 150, A1577, (2003).
- <sup>78</sup> J. Liu, A. Manthiram. Understanding the Improvement in the Electrochemical Properties of Surface Modified 5 V LiMn<sub>1.42</sub>Ni<sub>0.42</sub>Co<sub>0.16</sub>O<sub>4</sub> Spinel Cathodes in Lithium-ion Cells. *Chem. Mater.*, 21, 1695, (2009).
- <sup>79</sup> A. Manthiram, K. Chemelewski, E.-S. Lee. A perspective on the high-voltage LiMn<sub>1.5</sub>Ni<sub>0.5</sub>O<sub>4</sub> spinel cathode for lithium-ion batteries. *Energy Environ. Sci.*, 7, 1339, (2014).

- 
- <sup>80</sup> M.M. Thackeray, C.S. Johnson, J.-S. Kim, K.C. Lauzze, J.T. Vaughey, N. Dietz, D. Abraham, S.A. Hackney, W. Zeltner, M.A. Anderson. ZrO<sub>2</sub>- and Li<sub>2</sub>ZrO<sub>3</sub>-stabilized spinel and layered electrodes for lithium batteries. *Electrochem. Commun.*, 5, 752, (2003).
- <sup>81</sup> A. Kraytsberg, H. Drezner, M. Auinat, A. Shapira, N. Solomatin, P. Axmann, M. Wohlfahrt-Mehrens, Y. Ein-Eli. Atomic Layer Deposition of a Protective MgF<sub>2</sub> Film on a Li-ion Battery LiMn<sub>1.5</sub>Ni<sub>0.5</sub>O<sub>4</sub> Cathode Powder Material. *ChemNanoMat*, 1, 577, (2015).
- <sup>82</sup> J. Hassoun, P. Reale, B. Scrosati. Recent advances in liquid and polymer lithium-ion batteries. *J. Mater. Chem.*, 17, 3668, (2007).
- <sup>83</sup> A.M. Glass, K. Nassau, T.J. Negran. Ionic conductivity of quenched alkali niobate and tantalate glasses. *J. Appl. Phys.*, 49, 4808, (1978).
- <sup>84</sup> N. Ohta, K. Takada, I. Sakaguchi, L. Zhang, R. Ma, K. Fukuda, M. Osada, T. Sasaki. LiNbO<sub>3</sub>-coated LiCoO<sub>2</sub> as cathode material for all solid-state lithium secondary batteries. *Electrochem. Commun.*, 9, 1486, (2007).
- <sup>85</sup> P. Heitjans, M. Masoud, A. Feldhoff, M. Wilkening. NMR and impedance studies of nanocrystalline and amorphous ion conductors: lithium niobate as a model system. *Faraday Discuss.*, 134, 67, (2007).
- <sup>86</sup> M. Gellert, K. I. Gries, J. Zakel, S. Kranz, S. Bradler, E. Hornberger, S. Müller, C. Yada, F. Rosciano, K. Volz, B. Roling. Charge Transfer across the Interface between LiNi<sub>0.5</sub>Mn<sub>1.5</sub>O<sub>4</sub> High-Voltage Cathode Films and Solid Electrolyte Films. *J. Electrochem. Soc.*, 162, A754, (2015).



- 
- <sup>87</sup> Z.-J. Zhang, S.-L. Chou, Q.-F. Gu, H.-K. Liu, H.-J. Li, K. Ozawa, J.-Z. Wang. Enhancing the High Rate Capability and Cycling Stability of  $\text{LiMn}_2\text{O}_4$  by Coating of Solid-State Electrolyte  $\text{LiNbO}_3$ . *ACS Appl. Mater. Interfaces*, 6, 22155, (2014).
- <sup>88</sup> G. Gabrielli, P. Axmann, T. Diemant, R. J. Behm, M. Wohlfahrt-Mehrens. Combining optimized  $\text{LiNi}_{0.5}\text{Mn}_{1.5}\text{O}_4$  particle morphology and  $\text{LiNbO}_3$  coating for long cycling-life graphite/ $\text{LiNi}_{0.5}\text{Mn}_{1.5}\text{O}_4$  full cells. *ChemSusChem*, DOI: 10.1002/cssc.201600278, (2016).
- <sup>89</sup> R. C. Mehrotra, M. M. Agrawal, P. N. Kapoor. Alkali-metal Hexa-alkoxides of Niobium and of Tantalum. *J. Chem. Soc. A*, 2673, (1968).
- <sup>90</sup> S. Hirano, K. Kato. Formation of  $\text{LiNbO}_3$  films by hydrolysis of metal alkoxides. *J. Non-Cryst. Solids*, 100, 538, (1988).
- <sup>91</sup> Sakka. Handbook of sol-gel science and technology. 1. Sol-gel processing. Chapter 5. Kluwer Academic Publisher. Norwell, USA, (2005).
- <sup>92</sup> M. D. Levi, D. Aurbach. Simultaneous Measurements and Modeling of the Electrochemical Impedance and the Cyclic Voltammetric Characteristics of Graphite Electrodes Doped with Lithium. *J. Phys. Chem. B*, 101, 4630, (1997).
- <sup>93</sup> J. Ying, C. Wan, C. Jiang, Y. Li. Preparation and characterization of high-density spherical  $\text{LiNi}_{0.8}\text{Co}_{0.2}\text{O}_2$  cathode material for lithium secondary batteries. *J. Power Sources*, 99, 78, (2001).
- <sup>94</sup> J. Ying, C. Jiang, C. Wan. Preparation and characterization of high-density spherical  $\text{LiCoO}_2$  cathode material for lithium ion batteries. *J. Power Sources*, 129, 264, (2004).

- 
- <sup>95</sup> X. Luo, X. Wang, L. Liao, S. Gamboa, P.J. Sebastian. Synthesis and characterization of high tap-density layered  $\text{Li}[\text{Ni}_{1/3}\text{Co}_{1/3}\text{Mn}_{1/3}]\text{O}_2$  cathode material via hydroxide co-precipitation. *J. Power Sources*, 158, 654, (2006).
- <sup>96</sup> X. Lou, Y. Zhang. Synthesis of  $\text{LiFePO}_4/\text{C}$  cathode materials with both high rate capability and high tap density for lithium-ion batteries. *J. Mater. Chem.*, 21, 4156, (2011).
- <sup>97</sup> W. Hua, J. Zhang, Z. Zheng, W. Liu, X. Peng, X.-D. Guo, B. Zhong, Y.-J. Wang, X. Wang. Na-doped Ni-rich  $\text{LiNi}_{0.5}\text{Co}_{0.2}\text{Mn}_{0.3}\text{O}_2$  cathode material with both high rate capability and high tap density for lithium ion batteries. *Dalton Trans.*, 43, 14824, (2014).
- <sup>98</sup> Electrochemical Test Cell ECC-Ref User Manual, Release 2.3. EL-CELL GmbH, Hamburg, Germany, (2014).
- <sup>99</sup> E. Barsoukov, J. R. Macdonald. Impedance Spectroscopy Theory, Experiment, and Applications, Second Edition. John Wiley & Sons, Inc., Hoboken, New Jersey (2005).
- <sup>100</sup> L. Klinger, E. Rabkin. Diffusion along the Grain Boundaries in Crystals with Dislocations. *Interface Sci.*, 6, 197, (1998).
- <sup>101</sup> T. Xu, M. Li. Size and shape of grain boundary network components and their atomic structures in polycrystalline nanoscale materials. *J. Appl. Phys.*, 118, 164302, (2015).

- 
- <sup>102</sup> P. Axmann, G. Gabrielli, M. Wohlfahrt-Mehrens. Tailoring high-voltage and high-performance  $\text{LiNi}_{0.5}\text{Mn}_{1.5}\text{O}_4$  cathode material for high energy lithium-ion batteries. *J. Power Sources.*, 301, 151, (2016).
- <sup>103</sup> G. Gabrielli, P. Axmann, M. Wohlfahrt-Mehrens. Study of  $\text{LiNi}_{0.5}\text{Mn}_{1.5}\text{O}_4$  Morphological Features for Reduced Electrolyte Decomposition at High Potential. *J. Electrochem. Soc.*, 163, A470, (2016).
- <sup>104</sup> K. Ariyoshi, Y. Iwakoshi, N. Nakayama, T. Ohzuku. Topotactic Two-Phase Reactions of  $\text{Li}[\text{Ni}_{1/2}\text{Mn}_{3/2}]\text{O}_4$  ( $P4_332$ ) in Nonaqueous Lithium Cells. *J. Electrochem. Soc.*, 151, A296, (2004).
- <sup>105</sup> S.-K. Hong, S.-I. Mho, I.-H. Yeo, Y. Kang, D.-W. Kim. Structural and electrochemical characteristics of morphology-controlled  $\text{Li}[\text{Ni}_{0.5}\text{Mn}_{1.5}]\text{O}_4$  cathodes. *Electrochim. Acta*, 156, 29, (2015).
- <sup>106</sup> L. Wang, H. Li, X. Huang, E. Baudrin. A comparative study of  $\text{Fd-3m}$  and  $P4_332$  “ $\text{LiNi}_{0.5}\text{Mn}_{1.5}\text{O}_4$ ”. *Solid State Ionics*, 193, 32, (2011).
- <sup>107</sup> J. Cabana, M. Casas-Cabanas, F. O. Omenya, N. A. Chernova, D. Zeng, M. S. Whittingham, C. P. Grey. Composition-Structure Relationships in the Li-Ion Battery Electrode Material  $\text{LiNi}_{0.5}\text{Mn}_{1.5}\text{O}_4$ . *Chem. Mater.*, 24, 2952, (2012).
- <sup>108</sup> S.H. Park, S.-W. Oh, S.H. Kang, I. Belharouak, K. Amine, Y.-K. Sun. Comparative study of different crystallographic structure of  $\text{LiNi}_{0.5}\text{Mn}_{1.5}\text{O}_{4-\delta}$  cathodes with wide operation voltage (2.0–5.0 V). *Electrochim. Acta*, 52, 7226, (2007).
- <sup>109</sup> P. G. Bruce, B. Scrosati, J.-M. Tarascon. Nanomaterials for Rechargeable Lithium Batteries. *Angew. Chem. Int. Ed.*, 47, 2930, (2008).
- <sup>110</sup> R. Xu, X. Zhang, R. Chamoun, J. Shui, J. C. M. Li, J. Lu, Khalil Amine, I. Belharouak. Enhanced rate performance of  $\text{LiNi}_{0.5}\text{Mn}_{1.5}\text{O}_4$  fibers synthesized by electrospinning. *Nano Energy*, 15, 616, (2015).

- 
- <sup>111</sup> M. A. Kiani, M. S. Rahmanifar, M. F. El-Kady, R. B. Kaner, M. F. Mousavi. Fabrication of high power  $\text{LiNi}_{0.5}\text{Mn}_{1.5}\text{O}_4$  battery cathodes by nanostructuring of electrode materials. *RSC Adv.*, 5, 50433, (2015).
- <sup>112</sup> A. S. Aricò, P. Bruce, B. Scrosati, J.-M. Tarascon, W. Van Schalkwijk. Nanostructured materials for advanced energy conversion and storage devices. *Nat. Mater.*, 4, 366, (2005).
- <sup>113</sup> M. Kunduraci, G. G. Amatucci. Synthesis and Characterization of Nanostructured 4.7 V  $\text{Li}_x\text{Mn}_{1.5}\text{Ni}_{0.5}\text{O}_4$  Spinel for High-Power Lithium-Ion Batteries. *J. Electrochem. Soc.*, 153, A1345, (2006).
- <sup>114</sup> Y. Talyosef, B. Markovsky, R. Lavi, G. Salitra, D. Aurbach, D. Kovacheva, M. Gorova, E. Zhecheva, R. Stoyanova. Comparing the Behavior of Nano- and Microsized Particles of  $\text{LiMn}_{1.5}\text{Ni}_{0.5}\text{O}_4$  Spinel as Cathode Materials for Li-Ion Batteries. *J. Electrochem. Soc.*, 154, A682, (2007).
- <sup>115</sup> P. Steiner, H. Höchst. X-Ray Excited Photoelectron Spectra of  $\text{LiNbO}_3$ : A Quantitative Analysis. *Z. Physik B*, 35, 51, (1979).
- <sup>116</sup> N. Kaufherr, D. J. Eichorst, D. A. Payne. X-ray photoelectron spectroscopy studies of alkoxide-derived lithium niobate. *J. Vac. Sci. Technol. A*, 14, 299, (1996).
- <sup>117</sup> L. Baggetto, N. J. Dudney, G. M. Veith. Surface chemistry of metal oxide coated lithium manganese nickel oxide thin film cathodes studied by XPS. *Electrochim. Acta*, 90, 135, (2013).

# Acknowledgments

I would like to start my acknowledgments with a sincere thanks to Prof. Dr. Werner Tillmetz who gave me the possibility to carry out my P.h.D work at the ZSW and to Prof. Dr. Mika Lindén for the prompt availability as second supervisor. All my gratitude also to Dr. Margret Wohlfahrt-Mehrens and Dr. Peter Axmann for their constant support and their valuable advices during my entire research work.

I would like to go on with a special thanks to Dr. Emanuele Gucciardi, Dr. Mario Marinaro, Dr. Marilena Mancini and all the other colleagues that accompanied and advised me in the last years. My thanks are also extended to all the colleagues who helped me out with different experimental procedures and techniques. Among them: Gisela Arnold, Paul Drews, Dr. Meike Fleischhammer and Wolfgang Weirather. In addition, many thanks to Dr. Thomas Diemant and Prof. Dr. Rolf Jürgen Behm for their valuable contribution in the materials investigation.

My work would not have been possible without the financial support of the German Research Foundation (DFG), The European Community and the German Federal Ministry for Education and Research (BMBF) in the framework of the projects: *Funktionsmaterialien und Materialanalytik zu Lithium-Hochleistungsbatterien*, *Advanced High Performance Polymer Lithium Batteries for Electrochemical Storage* (APPLES) and *Li-EcoSafe*.

A special thanks goes to my family and in particular to my parents who made everything possible.



# **Declaration**

I herewith declare that the presented manuscript was not produced with the aids of third parties other than specified, and that the notions here reported were not directly taken over from any external source.

This thesis work has not been submitted in the present or similar forms to any other examination board.

Ulm, June 08, 2016

Giulio Gabrielli





# *Curriculum Vitae*

# Giulio Gabrielli

## **Personal Details**

---

First Name	Giulio
Family Name	Gabrielli
Date of Birth	12 September 1985
Nationality	Italian

## **Studies**

---

09/2012-12/2016	<b>Ph.D.</b> , Zentrum für Sonnenenergie- und Wasserstoff-Forschung Baden-Württemberg (ZSW)
Dissertation Title	Studies of high voltage $\text{LiNi}_{0.5}\text{Mn}_{1.5}\text{O}_4$ as positive electrode material in lithium ion cells
Final Grade	Summa cum Laude
Supervisor	Prof. Werner Tillmetz
10/2007-03/2010	<b>M.Sc. Photochemistry and Chemistry of Materials</b> , University of Bologna (Italy)
Dissertation Title	Silicon based anodes for lithium-ion batteries
Final Grade	110/110 (full marks)
Supervisor	Prof. Marina Mastragostino
09/2004-12/2007	<b>B.Sc. Chemistry of Materials</b> , University of Bologna (Italy)
Dissertation Title	Hydroxylapatite based porous scaffolds
Final Grade	110/110 (full marks) cum Laude
Supervisor	Prof. Adriana Bigi

09/1999-07/2004    **High School Diploma**, Liceo Scientifico “Guglielmo Marconi”  
Pesaro (Italy)  
Final Grade    96/100

## **Work Experience**

09/2011-09/2012    **Research Assistants**  
Employer    University of Milan

05/2010-12/2010    **Scholarship holder**  
Employer    University of Bologna

## **Knowledge of Languages (Self-Assessment)**

Italian    Mother tongue  
English    C1  
German    B2  
Spanish    A2

## **List of Publications**

Papers    *Combining optimized  $\text{LiNi}_{0.5}\text{Mn}_{1.5}\text{O}_4$  particle morphology and  $\text{LiNbO}_3$  coating for long cycling-life graphite/ $\text{LiNi}_{0.5}\text{Mn}_{1.5}\text{O}_4$  full cells*  
G. Gabrielli, P. Axmann, T. Diemant, R.J. Behm, M. Wohlfahrt-Mehrens  
ChemSusChem, 10.1002/cssc.201600278, (2016)

*A high-voltage and high-capacity  $\text{Li}_{1+x}\text{Ni}_{0.5}\text{Mn}_{1.5}\text{O}_4$  cathode material – from synthesis to full lithium-ion cell*  
M. Mancini, P. Axmann, G. Gabrielli, M. Kinyanjui, U. Kaiser, M. Wohlfahrt-Mehrens  
ChemSusChem, 10.1002/cssc.201600365 (2016)

*Study of  $\text{LiNi}_{0.5}\text{Mn}_{1.5}\text{O}_4$  Morphological Features for Reduced Electrolyte Decomposition at High Potential*

G. Gabrielli, P. Axmann, M. Wohlfahrt-Mehrens

Journal of the Electrochemical Society, 163, A470 (2016)

*Tailoring high-voltage and high-performance  $\text{LiNi}_{0.5}\text{Mn}_{1.5}\text{O}_4$  cathode material for high energy lithium-ion batteries*

P. Axmann, G. Gabrielli, M. Wohlfahrt-Mehrens

Journal of Power Sources, 301, 151 (2016)

*Thermal stability and flammability of electrolytes for lithium-ion batteries*

C. Arbizzani, G. Gabrielli, M. Mastragostino

Journal of Power Sources, 196, 4801 (2011)

**Oral Presentations**    *Developing High Cycling Stability Graphite/ $\text{LiNi}_{0.5}\text{Mn}_{1.5}\text{O}_4$  Li-Ion Cells*  
G. Gabrielli, P. Axmann, M. Wohlfahrt-Mehrens  
229th ECS Meeting 2016, May 29 - June 2, San Diego, California  
(United States)

*High Performance Spinel Material Studied as High-Voltage and High-Capacity Cathode for Li-Ion Batteries*

G. Gabrielli, M. Mancini, P. Axmann, M. Wilka, M. Wohlfahrt-Mehrens

Batterieforum Deutschland 2015, 21-23 January 2015, Berlin  
(Germany)

*High performance high voltage spinel materials as cathode for Li-ion batteries and its application in full cells*

G. Gabrielli, P. Axmann, M. Wilka, M. Wohlfahrt-Mehrens

GDCh Wissenschaftsforum Chemie 2013, 1-4 September 2013, Darmstadt (Germany)

**Posters** *Strategies to improve long term stability of graphite/LMNO full cells*

G. Gabrielli, P. Axmann, Thomas Diemant, Rolf Jürgen Behm, M. Wohlfahrt-Mehrens

Battery Conference, 25-27 April 2016, Münster (Germany)

*Effect of the surface area and morphology of high voltage spinel materials on the stability of organic electrolyte working at high potential*

G. Gabrielli, P. Axmann, M. Wilka, M. Wohlfahrt-Mehrens

ILED, May 28-30 May 2014, Rome (Italy)